Chapter 13

Single Emitters in Isolated Quantum Systems

Glenn S. Solomon[*], **Charles Santori**[†], **and Axel Kuhn**[‡]

[*] *Joint Quantum Institute, National Institute of Standards and Technology & University of Maryland, Gaithersburg, MD, USA*
[†] *Hewlett-Packard Laboratories, 1501 Page Mill Rd., Palo Alto, CA, 94304, USA*
[‡] *University of Oxford, Clarendon Laboratory, Parks Road, OX1 3PU, United Kingdom*

Chapter Outline

Single-Photon Generation and Detection, Volume 45. http://dx.doi.org/10.1016/B978-0-12-387695-9.00013-5

13.1 INTRODUCTION

The interfacing of discrete matter states and photons, the storage and retrieval of single photons, and the mapping of quantum states between distant entities constitute essential building blocks of future quantum communication networks and quantum information processors [1]. Ideally, such systems are composed of individual nodes acting as quantum gates or memories, with optical links between them that allow for the entanglement or teleportation of their quantum states, or for optical quantum information processing using light traveling between the nodes [2]. With individual photons acting as messengers in these networks, substantial efforts are being undertaken that focus on the production and characterization of single photons. Applications which rely on the availability of single photons include quantum cryptography, optical quantum computing, light-matter entanglement, and atom-photon state mapping. All of these have been successfully demonstrated.

For most of these applications, sources of single photons based on discrete, isolated quantum system are ideally suited, given their capability of emitting streams of indistinguishable photons on demand. Examples of a discrete quantum system are a single atom or molecule, or an engineered system like a quantum dot or a color center in a solid-state matrix. These systems are inherently simple and robust, as they can only emit one single photon in a de-excitation process. Here, we discuss both atomic and solid-state sources of single photons on demand. We examine two atomic sources, single atoms and single ions; and, two solid-state sources, strain-induced epitaxial quantum dots and nitrogen-vacancy centers in diamonds. Important fundamental properties of on-demand single-photon sources are analyzed for these four cases, including single-photon purity and indistinguishability. The interactions of these matter states with optical cavities is important for our fundamental understanding as well as the development of improved single-photon emitters. These interactions are examined in the context of cavity-quantum electrodynamic effects.

13.2 SINGLE PHOTONS FROM ATOMS AND IONS - A. KUHN

A large number of atomic species provide simple electronic level structures. Therefore they can be excited in a way that one atom emits exactly one single photon of well-defined frequency and polarization upon either spontaneous or stimulated emission. With all atoms or ions of the same isotope being identical, different photon sources based on the same species can produce indistinguishable photons without further measures, provided the same transitions are used and the electromagnetic environment is identical for all atoms. This makes them ideal candidates for the implementation of large-scale quantum computing networks. However, harnessing their emission into one single optical mode, or holding a single atom or ion trapped in place, are both challenging tasks that are not easy to meet. Here, we first discuss the emission

of single photons from freely moving or trapped atoms or ions into free space and then highlight a couple of major achievements, such as the entanglement of remote entities. Second, we introduce the basic principles of cavity-quantum electrodynamics (CQED), and show how to apply these to channel the photon emission into a single mode of the radiation field, with the vacuum field inside the cavity stimulating the process. Third, we elucidate how to determine and control the coherence properties of these photons in the time domain and use that degree of control for information encoding.

13.2.1 Emission into Free Space

In 1977, Kimble *et al.* [3] have been investigating the photon statistics of light emitted from single atoms. Figure 13.1a and b illustrates their setup along with their results. Sodium atoms in an atomic beam are excited on the $2^2S_{1/2}(F = 2, m_F = 2) \longrightarrow 3^2P_{3/2}(F = 3, m_F = 3)$ transition and behave like an effective two-level system. The fluorescence from the excitation region is collected with a lens of high numerical aperture and then directed to a pair of photon counters in a Hanbury Brown-Twiss arrangement (c.f. Chapter 2) to measure the $g^{(2)}(\tau)$ intensity correlation of the fluorescence light. A minimum around zero detection-time delay is evident. This can be easily understood as the atom is in its ground state immediately after a photon emission has taken place. Hence the probability for emitting another photon drops instantly thereafter to zero and then slowly rises again to the average photon-emission probability. For an ideal single-photon emitter, one would expect to find $g^{(2)}(0) = 0$. However, because of the random distribution of atoms within the atomic beam, a somewhat larger residual signal was found in this experiment.

The situation is different if one analyzes the light emerging from a single trapped emitter, like a single ion in a Paul trap [4]. In this case, a deeper anti-bunching dip where $g^{(2)}(0) = 0$ is observed, see Fig. 13.1c. If the exciting laser is sufficiently intense, the ion is furthermore subject to Rabi oscillations which give rise to the noticeable modulation of the correlation function.

The above experiments [3,4] have in common that an effective two-level system, i.e. atom or ion, is continuously driven. By consequence, one can neither control the exact emission time, nor the number of successive photon emissions, nor the exact time span between those. A straightforward remedy resolving these issues is the application of a pulsed excitation scheme in a three-level atom. For instance, with a laser π-pulse exciting $|e\rangle \longrightarrow |x\rangle$ and the emission taking place upon a transition from $|x\rangle$ to $|g\rangle$, the timing issue may be resolved. Also, no further emissions from the same atom can happen until it is actively brought back into its initial state $|e\rangle$. Monroe [5] and Weinfurter [6] successfully applied such schemes to entangle the polarization of a single photon with the spin of a single ion or atom, respectively. To do so, they realised an excitation scheme leading to two possible final spin states of the atom, $|g_\downarrow\rangle$ and $|g_\uparrow\rangle$ upon emission of either a σ^+ or σ^- polarized photon, thus projecting the whole system into

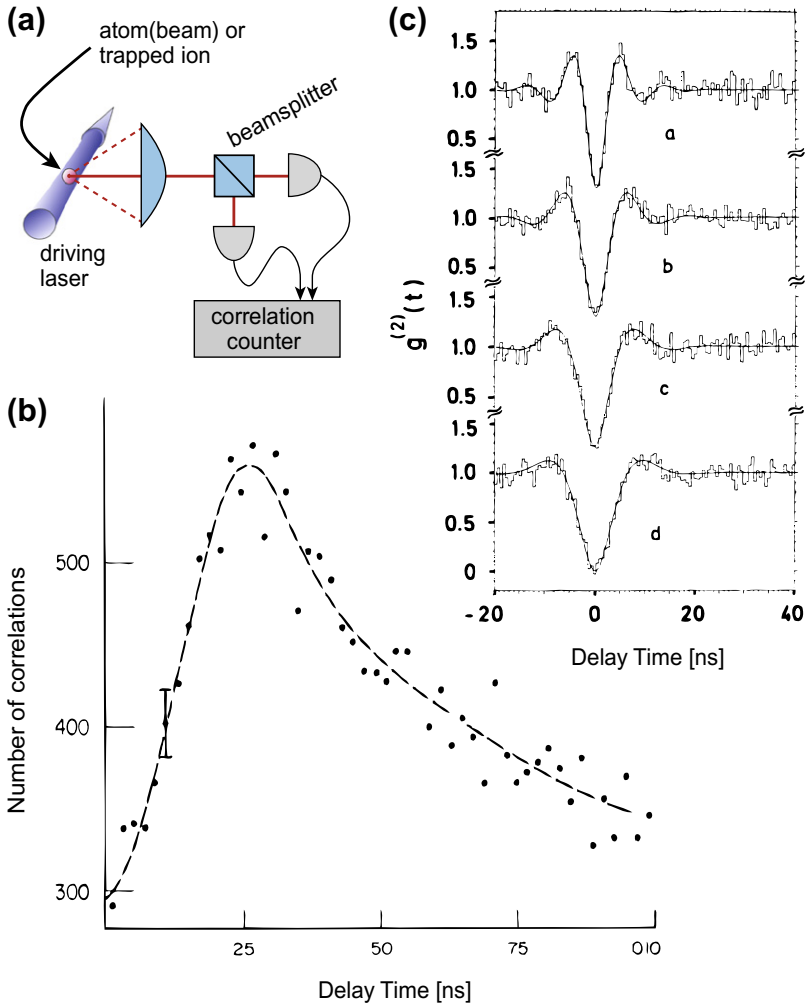

FIGURE 13.1 Intensity correlation function $g^{(2)}(\tau)$ measured using a Hanbury Brown-Twiss arrangement for two-photon coincidence counting (a). Such an arrangement has first been used by Kimble *et al.* [3] to analyse the fluorescence of Sodium atoms in an atomic beam (b), *panel adapted from [3], Copyright (1977) by The American Physical Society*. Thereafter, Diedrich and Walther [4] have been using a similar arrangement to investigate the non-classical photon statistics in the fluorescence of a single trapped ion (c), *panel adapted from [4], Copyright (1987) by The American Physical Society.*

the entangled atom-photon state

$$|\psi^+\rangle = (|g_\downarrow,+\rangle + |g_\uparrow,-\rangle)/\sqrt{2}. \tag{13.1}$$

Projective measurements on pairs of photons emitted from two distant atoms or ions have then been used for entanglement swapping, thus resulting in

the entanglement and teleportation of quantum states [7]. Such photon-matter entanglement has a potential advantage of adding memory capabilities to quantum information protocols. In addition, this provides a quantum matter light interface, thereby using different physical media for different purposes in a quantum information application.

This success story impressively demonstrates the inherent potential of using identical atoms or ions as single-photon emitters. The emission spectra are all identical, and coupling different emitters is relatively easy as compared to, e.g. solid-state sources, which need to be tuned individually. However, the spontaneous emission of photons into all directions is an inherent limitation. Even the best collection optics captures at most 25% of the photons [8], with actual experiments reaching overall photon-detection efficiencies of $\approx 5 \times 10^{-4}$ [6]. Combined with the spontaneous character of the emission, these sources are rendered probabilistic and scaling is a serious issue. We shall see in the following that the coupling of atoms or ions to optical cavities is one effective solution to this problem. First, the direction of emission is imposed, with all photons emitted into a single cavity mode, and second, the photon emission is stimulated by the vacuum field of the cavity, with the driving laser allowing for an unprecedented control of the emission process.

13.2.2 Cavity-Based Single-Photon Emitters

In the following, we closely follow, summarize and extend our review published in Contemporary Physics [9] to introduce the concepts, characteristic properties, and major implementations of state-of-the-art single-photon sources based on single atoms or ions in cavities. These have all the potential to meet the requirements of optical quantum computing and quantum networking schemes, namely deterministic single-photon emission with unit efficiency, directed emission into a single spatial mode of the radiation field, indistinguishable photons with immaculate temporal and spatial coherence, and reversible quantum state mapping and entanglement between atoms and photons.

Starting from the elementary principles of cavity-quantum electrodynamics, we discuss how a single quantum system couples to the quantised field within optical resonators. We then show how to exploit these effects to generate single photons on demand in the strong-coupling regime and the bad cavity limit, using either an adiabatic driving technique or a sudden excitation of the emitter. To conclude, we discuss the most prominent experimental achievements and examine the different approaches for obtaining single photons from cavities using either atoms or ions as photon emitters.

13.2.2.1 Atom-Photon Interaction in Resonators

Here we discuss how a single quantum system, which shows discrete energy levels like an individual atom or ion, couples to the quantized modes of the radiation field in a cavity. We introduce the relevant features of cavity-QED

and the Jaynes-Cummings model [10,11], and extend these to three-level atoms with two dipole transitions driven by two radiation fields. One of the fields is from a laser, the other is the cavity field coupled to the *atom* (which stands in here for any quantum system showing discrete energy levels). We furthermore explain how the behavior of a coupled atom-cavity system depends on the most relevant cavity parameters, such as the cavity's mode volume and its finesse.

Field quantization in cavity QED: We consider a Fabry-Perot cavity with mirror separation l and reflectivity $\mathcal{R}$. The cavity has a free spectral range $\Delta\omega_{\mathrm{FSR}} = 2\pi \times c/(2l)$, and its finesse is defined as $\mathcal{F} = \pi\sqrt{\mathcal{R}}/(1-\mathcal{R})$. In the vicinity of a resonance, the transmission profile is Lorentzian with a linewidth (FWHM) of $2\kappa = \Delta\omega_{\mathrm{FSR}}/\mathcal{F}$, which is twice the decay rate, κ, of the cavity field. Curved mirrors are often used to restrict the cavity eigenmodes to geometrically stable Laguerre-Gaussian or Hermite-Gaussian modes. In most cases, just one of these modes is of interest, characterized by its mode function $\psi_{\mathrm{cav}}(\mathbf{r})$ and its resonance frequency ω_{cav}. The state vector can therefore be expressed as a superposition of photon-number states, $|n\rangle$, and for n photons in the mode the energy reads $\hbar\omega_{\mathrm{cav}}(n+\frac{1}{2})$. The equal energy spacing allows for an analog treatment of the cavity as an harmonic oscillator. Creation and annihilation operators for a photon, $\hat{a}^\dagger$ and $\hat{a}$, are then used to express the Hamiltonian of the cavity,

$$H_{\mathrm{cav}} = \hbar\omega_{\mathrm{cav}}\left(\hat{a}^\dagger\hat{a} + \frac{1}{2}\right). \tag{13.2}$$

This Hamiltonian does not account for any losses. In a real cavity, all photon-number states decay until thermal equilibrium with the environment is reached. In the optical domain, the latter corresponds to the vacuum state, $|0\rangle$, with no photons remaining in the cavity.

Two-level atom: We now analyse how the cavity field interacts with a two-level atom with ground state $|g\rangle$ and excited state $|x\rangle$ of energies $\hbar\omega_{\mathrm{g}}$ and $\hbar\omega_{\mathrm{x}}$, respectively, and transition dipole moment μ_{xg}. The Hamiltonian of the atom is

$$H_{\mathrm{A}} = \hbar\omega_{\mathrm{g}}|g\rangle\langle g| + \hbar\omega_{\mathrm{x}}|x\rangle\langle x|. \tag{13.3}$$

The coupling to the field mode of the cavity is expressed by the atom-cavity coupling constant,

$$g(\mathbf{r}) = g_0\,\psi_{\mathrm{cav}}(\mathbf{r}), \quad \text{with } g_0 = \sqrt{(\mu_{\mathrm{xg}}^2\omega_{\mathrm{cav}})/(2\hbar\epsilon_0 V)}, \tag{13.4}$$

where V is the mode volume of the cavity. As the atom barely moves during the interaction, we can safely disregard its external degrees of freedom. Furthermore we assume maximum coupling, i.e. $\psi_{\mathrm{cav}}(\mathbf{r}_{\mathrm{atom}}) = 1$, so that one obtains $g(\mathbf{r}) = g_0$. In a closed system, any change of the atomic state goes hand-in-hand with a corresponding change of the photon number, n. Hence the interaction Hamiltonian of the atom-cavity system reads

$$H_{\mathrm{int}} = -\hbar g_0\left[|x\rangle\langle g|\hat{a} + \hat{a}^\dagger|g\rangle\langle x|\right]. \tag{13.5}$$

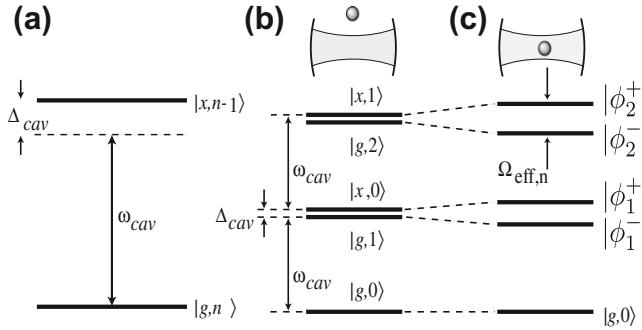

FIGURE 13.2 **(a)** A two-level atom with ground state $|g\rangle$ and excited state $|x\rangle$ coupled to a cavity containing n photons. In the dressed-level scheme of the combined atom-cavity system with the atom outside (b) or inside (c) the cavity, the state doublets are either split by Δ_{cav} or by the effective Rabi frequency, $\Omega_{\text{eff,n}}$, respectively.

For a given excitation number n, the cavity only couples $|g,n\rangle$ and $|x,n-1\rangle$. If the cavity mode is resonant with the atomic transition, the population then oscillates with the Rabi frequency $\Omega_{\text{cav}} = 2g_0\sqrt{n}$ between these states.

The eigenfrequencies of the total Hamiltonian, $H = H_{\text{cav}} + H_{\text{A}} + H_{\text{int}}$, can be found easily. In the rotating wave approximation, they read

$$\omega_{\text{n}}^{\pm} = \omega_{\text{cav}}\left(n + \frac{1}{2}\right) + \frac{1}{2}\left(\Delta_{\text{cav}} \pm \sqrt{4ng_0^2 + \Delta_{\text{cav}}^2}\right), \tag{13.6}$$

where $\Delta_{\text{cav}} = \omega_{\text{x}} - \omega_{\text{g}} - \omega_{\text{cav}}$ is the detuning between atom and cavity. Figure 13.2 illustrates this level splitting. Two corresponding eigenstates get split by $\Omega_{\text{eff,n}} = \sqrt{4ng_0^2 + \Delta_{\text{cav}}^2}$, which is the effective Rabi frequency at which the population oscillates between states $|g,n\rangle$ and $|x,n-1\rangle$. The cavity field stimulates the emission of an excited atom into the cavity, thus de-exciting the atom and increasing the photon number by one. Subsequently, the atom is re-excited by absorbing a photon from the cavity field, and so forth. In particular, an excited atom and a cavity containing no photon are sufficient to start the oscillation between $|x,0\rangle$ and $|g,1\rangle$ at frequency $\sqrt{4g_0^2 + \Delta_{\text{cav}}^2}$. This phenomenon is known as vacuum-Rabi oscillation. On resonance, i.e. for $\Delta_{\text{cav}} = 0$, the oscillation frequency $2g_0$ is therefore called vacuum-Rabi frequency. To summarize, the atom-cavity interaction splits the photon-number states into doublets of non-degenerate dressed states, which are named after Jaynes and Cummings [10,11]. Only the ground state $|g,0\rangle$ is not coupled to other states and is not subject to any energy shift or splitting.

Three-level atom: We now consider an atom with a Λ-type three-level scheme providing transition frequencies $\omega_{\text{xe}} = \omega_{\text{x}} - \omega_{\text{e}}$ and $\omega_{\text{xg}} = \omega_{\text{x}} - \omega_{\text{g}}$ as depicted in Fig. 13.3. The $|e\rangle \leftrightarrow |x\rangle$ transition is driven by a classical light field

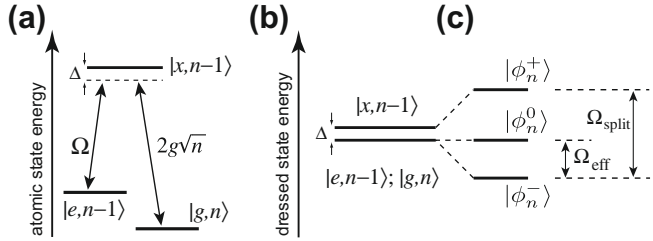

FIGURE 13.3 (a) A three-level atom driven by a classical laser field of Rabi frequency Ω, coupled to a cavity containing n photons. (b) Dressed-level scheme of the combined system without coupling, and (c) for an atom interacting with laser and cavity. The triplet is split by $\Omega_{\text{split}} = \sqrt{4ng_0^2 + \Omega^2 + \Delta^2}$. In the limit of a large detuning Δ, the Raman transition $|e,n-1\rangle \leftrightarrow |g,n\rangle$ is driven at the effective Rabi frequency $\Omega_{\text{eff}} = \frac{1}{2}\left(\Omega_{\text{split}} - |\Delta|\right) \approx (4ng_0^2 + \Omega^2)/|4\Delta|$.

of frequency ω_{L} with Rabi frequency Ω, while a cavity mode with frequency ω_{cav} couples to the $|g\rangle \leftrightarrow |x\rangle$ transition. The respective detunings are defined as $\Delta_{\text{L}} = \omega_{\text{xe}} - \omega_{\text{L}}$ and $\Delta_{\text{cav}} = \omega_{\text{xg}} - \omega_{\text{cav}}$. Provided the driving laser and the cavity only couple to their respective transitions, the interaction Hamiltonian

$$\begin{aligned} H_{\text{int}} = \hbar[&\Delta_{\text{L}}|e\rangle\langle e| + \Delta_{\text{cav}}|g\rangle\langle g| - \frac{\Omega}{2}(|x\rangle\langle e| + |e\rangle\langle x|) \\ &-g_0(|x\rangle\langle g|a + a^{\dagger}|g\rangle\langle x|)] \end{aligned} \tag{13.7}$$

determines the behavior of the system. Given an arbitrary excitation number n, this Hamiltonian couples only the three states $|e,n-1\rangle, |x,n-1\rangle, |g,n\rangle$. For this triplet and a Raman-resonant interaction with $\Delta_{\text{L}} = \Delta_{\text{cav}} \equiv \Delta$, the eigenfrequencies of the coupled system read

$$\begin{aligned} \omega_{\text{n}}^0 &= \omega_{\text{cav}}\left(n + \frac{1}{2}\right) \quad \text{and} \\ \omega_{\text{n}}^{\pm} &= \omega_{\text{cav}}\left(n + \frac{1}{2}\right) + \frac{1}{2}\left(\Delta \pm \sqrt{4ng_0^2 + \Omega^2 + \Delta^2}\right). \end{aligned} \tag{13.8}$$

The previously discussed Jaynes-Cummings doublets are now replaced by triplets,

$$\begin{aligned} |\phi_{\text{n}}^0\rangle &= \cos\Theta|e,n-1\rangle - \sin\Theta|g,n\rangle, \\ |\phi_{\text{n}}^+\rangle &= \cos\Phi\sin\Theta|e,n-1\rangle - \sin\Phi|x,n-1\rangle \\ &\quad + \cos\Phi\cos\Theta|g,n\rangle, \\ |\phi_{\text{n}}^-\rangle &= \sin\Phi\sin\Theta|e,n-1\rangle + \cos\Phi|x,n-1\rangle \\ &\quad + \sin\Phi\cos\Theta|g,n\rangle, \end{aligned} \tag{13.9}$$

where the mixing angles Θ and Φ are given by

$$\tan\Theta = \frac{\Omega}{2g_0\sqrt{n}}, \quad \tan\Phi = \frac{\sqrt{4ng_0^2+\Omega^2}}{\sqrt{4ng_0^2+\Omega^2+\Delta^2}-\Delta}. \tag{13.10}$$

We note that the interaction with the light lifts the degeneracy of the eigenstates. However, $|\phi_n^0\rangle$ is neither subject to an energy shift, nor does the excited atomic state contribute to it. Therefore it's a "dark state" that does not decay by spontaneous emission.

In the limit of vanishing Ω, the states $|\phi_n^\pm\rangle$ correspond to the Jaynes-Cummings doublet and the third eigenstate, $|\phi_n^0\rangle$, coincides with $|e,n-1\rangle$. Also the eigenfrequency ω_n^0 is not affected by Ω or g_0. Therefore transitions between the dark states $|\phi_{n+1}^0\rangle$ and $|\phi_n^0\rangle$ are always in resonance with the cavity.

Cavity-coupling regimes: So far, we have been considering the interaction Hamiltonian and the associated eigenvalues and dressed eigenstates that one obtains whenever a two- or three-level atom is coupled to a cavity. We have been neglecting the atomic polarization decay rate, γ, and the field-decay rate of the cavity, κ (Note that the population decay rate of the atom is 2γ, and the photon loss rate from the cavity is 2κ). It is evident that both relaxation rates result in a damping of a possible vacuum-Rabi oscillation between states $|x,0\rangle$ and $|g,1\rangle$. Only in the regime of *strong atom-cavity coupling*, with $g_0 \gg \{\kappa,\gamma\}$, the damping is weak enough so that vacuum-Rabi oscillations can occur. The other extreme is the *bad-cavity regime*, with $\kappa \gg g_0^2/\kappa \gg \gamma$, which results in strong damping and quasi-stationary quantum states of the coupled system if it is continuously driven.

Two properties of the cavity can be used to distinguish between these regimes: First the strength of the atom-cavity coupling, $g_0 \propto 1/\sqrt{V}$ (dependant upon the mode volume of the cavity), and second the finesse $\mathcal{F} = \pi\sqrt{R}/(1-R)$ of the resonator, which depends on the mirror reflectivity R. The finesse gives the mean number of round trips in the cavity before a photon is lost by transmission through one of the cavity mirrors, and it is also identical to the ratio of free spectral range $\Delta\omega_{FSR}$ to cavity linewidth 2κ. To reach strong coupling, a high value of g_0 and therefore a short cavity of small mode volume are normally required. Keeping κ small enough at the same time then calls for a high finesse and a mirror reflectivity $R \geq 99.999\%$.

13.2.2.2 Single-Photon Emission

For the deterministic generation of single photons from atom-cavity systems, all schemes implemented to date rely on the Purcell effect [12]. The spatial mode density inside the cavity is altered substantially, such that the spontaneous emission rate can be either enhanced ($f > 1$) or inhibited ($f < 1$) by the Purcell

factor

$$f = \frac{3Q\lambda^3}{4\pi^2 V},$$

depending on the cavity's mode volume, V, and quality factor, Q. More importantly, the probability of spontaneous emission placing a photon into the cavity is given by $\beta = f/(f+1)$. If the mode volume of the cavity is sufficiently small, the emitter and cavity couple so strongly that $\beta \approx 1$, i.e. emissions into the cavity outweigh spontaneous emissions into free space. A deterministic photon emission into a single field mode is therefore possible with an efficiency close to unity. These effects have first been observed by Carmichael *et al.* [13] and De Martini *et al.* [14]. Moreover, with the coherence properties uniquely determined by the parameters of the cavity and the driving process, one should be able to obtain indistinguishable photons from different cavities. Note also that state mapping and entanglement between atomic spin and photon polarization has recently been demonstrated in cavity-based single-photon emitters [15–18]. Additionally the reversibility of the photon generation process, and quantum networking between different cavities has been predicted [19–21], and demonstrated [22–24]. We now introduce different ways of producing single photons from such a system. These include cavity-enhanced spontaneous emission and Raman transitions stimulated by the vacuum field while driven by classical laser pulses. In particular, we discuss a scheme for adiabatic coupling between a single atom and an optical cavity, which is based on a unitary evolution of the coupled atom-cavity system [25,26], and is therefore intrinsically reversible.

For a photon emission from the cavity to take place, it is evident that a finite value of κ is mandatory, otherwise any light would remain trapped between the mirrors. Moreover, as κ is the decay rate of the cavity field, the associated duration of an emitted photon is typically κ^{-1} or more. We also emphasise that γ plays a crucial role in most experimental settings, since it accounts for the spontaneous emission into non-cavity modes, and therefore leads to a reduction of efficiency. The relation of the atom-cavity coupling constant g_0 and the Rabi frequency Ω of the driving field to the two decay rates can be used for marking the difference between three basic classes of single-photon emission schemes from cavity-QED systems.

Cavity-enhanced spontaneous emission: We assume that a sudden excitation process (e.g. a short π pulse with $\Omega \gg \{g_0,\kappa,\gamma\}$, or some internal relaxation cascade from energetically higher states) drives the atom suddenly into its excited state $|x,0\rangle$. From there, a photon gets spontaneously emitted either into the cavity or into free space. To analyse the process, we simply consider an excited two-level atom coupled to an empty cavity. This particular situation is the textbook example of CQED that has been thoroughly analysed in the past. In fact, it was proposed by Purcell [12] and demonstrated by Heinzen *et al.* [27] and Morin *et al.* [28] that the spontaneous emission properties of an atom coupled to a cavity are significantly different from those in free space. For

an analysis of the atom's behavior, it is sufficient to consider the evolution of the $n = 1$ Jaynes-Cummings doublet under the influence of the atomic polarization decay rate γ and the cavity-field decay rate κ. Non-cavity spontaneous decay of the atom and photon emission through one of the cavity mirrors both lead the system into state $|g,0\rangle$, which does not belong to the $n = 1$ doublet. Therefore we can deal with these decay processes phenomenologically by introducing non-hermitian damping terms into the interaction Hamiltonian,

$$H'_{\text{int}} = -\hbar g_0 \left(|x\rangle\langle g|\hat{a} + \hat{a}^\dagger |g\rangle\langle x| \right) - i\hbar\gamma |x\rangle\langle x| - i\hbar\kappa \hat{a}^\dagger \hat{a}. \tag{13.11}$$

Figure 13.4a shows the time evolution of the atom-cavity system when $\kappa > g_0$. The strong damping of the cavity inhibits any vacuum-Rabi oscillation, since the photon is emitted from the cavity before it can be reabsorbed by the atom. Therefore the transient population in state $|g,1\rangle$ is negligible and the adiabatic approximation $\dot{c}_{\text{g}} \approx 0$ can be applied, which gives

$$\frac{d}{dt} c_{\text{x}} = -\gamma c_{\text{x}} - \frac{g_0^2}{\kappa} c_{\text{x}}, \tag{13.12}$$

with the solution

$$c_{\text{x}}(t) = \exp\left(-\left[\gamma + \frac{g_0^2}{\kappa} \right] t \right). \tag{13.13}$$

It is straightforward to see that the ratio of the emission rate into the cavity, g_0^2/κ, to the spontaneous emission probability into free space becomes $g_0^2/(\kappa\gamma) \equiv f$, i.e. the Purcell factor. It equals twice the one-atom cooperativity parameter, C, originally introduced in the context of optical bistability [29]. Hence the photon-emission probability from the cavity reads $P_{\text{Emit}} = 2C/(2C+1)$. Note that the atom radiates mainly into the cavity if $g_0^2/\kappa \gg \gamma$. Together with $\kappa \gg g_0$, this condition constitutes the bad-cavity regime.

The other extreme is strong coupling, with $g_0 \gg (\kappa,\gamma)$. In this case vacuum Rabi oscillations between $|x,0\rangle$ and $|g,1\rangle$ occur, with both states decaying at the respective rates γ and κ. Figure 13.4b shows a situation where the atom-cavity coupling, g_0, saturates the $|x,0\rangle \leftrightarrow |g,1\rangle$ transition. On average, the probabilities to find the system in either one of these two states are equal, and therefore the average ratio of the emission probability into the cavity to the spontaneous emission probability into free space is given by κ/γ. The vacuum-Rabi oscillation then gives rise to an amplitude modulation of the photons emitted from the cavity.

Bad-cavity regime: To take the effect of a slow excitation process into account, we consider a Λ-type three-level atom coupled to a cavity. In the bad-cavity regime, $\kappa \gg g_0^2/\kappa \gg \gamma$, the loss of excitation into unwanted modes of the radiation field is small and we may follow Law *et al.* [30,31]. We assume that the atom's $|e\rangle - |x\rangle$ transition is excited by a pump laser pulse while the atom

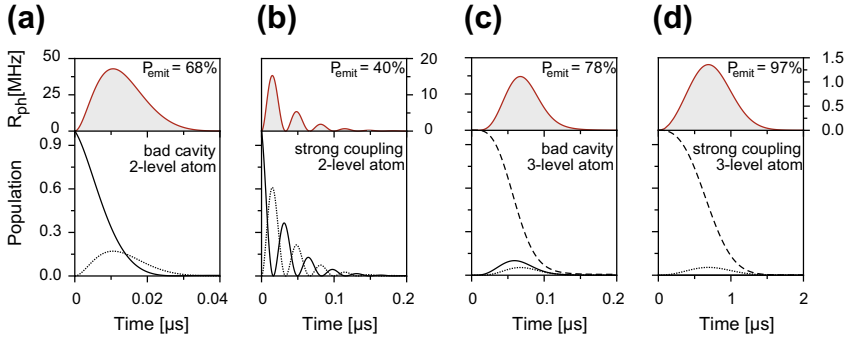

FIGURE 13.4 Evolution of the atomic states and photon emission rate $R_{\rm ph} = 2\kappa\rho_{\rm gg}$ in different coupling cases. (a) and (b) are for an excited two-level atom coupled to the cavity, showing populations $\rho_{\rm xx}$ (solid) and $\rho_{\rm gg}$ (dotted) of the product states $|x,0\rangle$ and $|g,1\rangle$. (c) and (d) are for a three-level atom-cavity system prepared in $|e,0\rangle$ and exposed to a pump pulse driving $|e\rangle - |x\rangle$ while the cavity couples $|x\rangle$ and $|g\rangle$. The initial-state population $\rho_{\rm ee}$ is dashed. (a) and (c) display the bad-cavity regime with $(g_0,\gamma,\kappa) = 2\pi \times (15,3,20) \times 10^6\ {\rm s}^{-1}$, while (b) and (d) depict the strong-coupling case with $(g_0,\gamma,\kappa) = 2\pi \times (15,3,2) \times 10^6\ {\rm s}^{-1}$. The pump pulses read $\Omega(t) = g_0 \sin(\pi t/200\ {\rm ns})$ in (c), and $\Omega(t) = g_0 \times t/1\ \mu{\rm s}$ in (d). No transient population is found in $\rho_{\rm xx}$ in the latter case. The overall photon-emission probability reads always $P_{\rm Emit} = \int R_{\rm ph}\, dt$.

emits a photon into the cavity by enhanced spontaneous emission. The cavity-field decay rate κ sets the fastest time scale, while the spontaneous emission rate into the cavity, g_0^2/κ, dominates the incoherent decay of the polarization from the excited atomic state. Provided any decay leads to a loss from the three-level system, the evolution of the wave vector is governed by the non-Hermitian Hamiltonian

$$H'_{\rm int} = H_{\rm int} - i\hbar\kappa\hat{a}^\dagger\hat{a} - i\hbar\gamma|x\rangle\langle x|, \tag{13.14}$$

with $H_{\rm int}$ from Eq. (13.7). To simplify the analysis, we take only the vacuum state, $|0\rangle$, and the one-photon state, $|1\rangle$, into account, thus that the state vector reads

$$|\Psi(t)\rangle = c_{\rm e}(t)|e,0\rangle + c_{\rm x}(t)|x,0\rangle + c_{\rm g}(t)|g,1\rangle, \tag{13.15}$$

where $c_{\rm e}, c_{\rm x}$, and $c_{\rm g}$ are complex amplitudes. Their time evolution is given by the Schrödinger equation, $i\hbar\frac{d}{dt}|\Psi\rangle = H'_{\rm int}|\Psi\rangle$, which yields

$$\begin{aligned} i\dot{c}_{\rm e} &= \tfrac{1}{2}\Omega(t)c_{\rm x} \\ i\dot{c}_{\rm x} &= \tfrac{1}{2}\Omega(t)c_{\rm e} + g_0 c_{\rm g} - i\gamma c_{\rm x} \\ i\dot{c}_{\rm g} &= g_0 c_{\rm x} - i\kappa c_{\rm g}, \end{aligned} \tag{13.16}$$

with the initial condition $c_{\rm e}(0) = 1, c_{\rm x}(0) = c_{\rm g}(0) = 0$ and $\Omega(0) = 0$. An adiabatic solution of (13.16) is found if the decay is so fast that $c_{\rm x}$ and $c_{\rm g}$ are nearly time independent. This allows one to make the approximations $\dot{c}_{\rm x} = 0$

and $\dot{c}_g = 0$, with the result

$$\begin{aligned} c_e(t) &\approx \exp\left(-\frac{\alpha}{4}\int_0^t \Omega^2(t')dt'\right), \\ c_x(t) &\approx -\tfrac{i}{2}\alpha\Omega(t)c_e(t), \\ c_g(t) &\approx -\tfrac{i}{\kappa}g_0 c_x(t), \end{aligned} \tag{13.17}$$

where $\alpha = 2/(2\gamma + 2g_0^2/\kappa)$. Photon emissions from the cavity occur if the system is in $|g,1\rangle$, at the photon-emission rate $R_{ph}(t) = 2\kappa|c_g(t)|^2$. This yields a photon-emission probability of

$$\begin{aligned} P_{Emit} &= \int R_{ph}(t)dt \\ &= \frac{g_0^2\alpha}{\kappa}\left[1 - \exp\left(-\frac{\alpha}{2}\int \Omega^2(t)dt\right)\right] \longrightarrow \frac{g_0^2\alpha}{\kappa}. \end{aligned} \tag{13.18}$$

Note that the exponential in Eq. (13.18) vanishes if the area $\int \Omega(t)dt$ of the exciting pump pulse is large enough. In this limit, the overall photon-emission probability does not depend on the shape and amplitude of the pump pulse. With a suitable choice of g_0, α, and κ, high photon-emission probabilities can be reached [31]. Furthermore, as the stationary state of the coupled system depends on $\Omega(t)$, the time envelope of the photon can be controlled to a large extend.

Strong-coupling regime: To study the effect of the exciting laser pulse in the strong-coupling regime, we again consider a Λ-type three-level atom coupled to a cavity. We assume that the strong-coupling condition also applies to the Rabi frequency of the driving field, i.e. $\{g_0, \Omega\} \gg \{\kappa, \gamma\}$. In this case, we can safely neglect the effect of the two damping rates on the time scale of the excitation. We then seek for a method to effectively stimulate a Raman transition between the two ground states that also places a photon into the cavity. For instance, the driving process can be implemented in form of an adiabatic passage (STIRAP process [25,26]) or a far-off-resonant Raman process to avoid any transient population of the excited state, thus reducing losses due to spontaneous emission into free space. An efficiency for photon generation close to unity can be reached this way. Once a photon is placed into the cavity, it gets emitted due to the finite cavity lifetime.

The most promising approach is to implement an adiabatic passage in the optical domain between the two ground states [32,33]. In fact, adiabatic passage methods have been used for coherent population transfer in atoms or molecules for many years. For instance, if a Raman transition is driven by two distinct pulses of variable amplitudes, effects like electromagnetically induced transparency (EIT) [34,35], slow light [36,37], and stimulated Raman scattering by adiabatic passage (STIRAP) [26] are observed. These effects have been demonstrated with classical light fields and have in common that

the system's state vector, $|\Psi\rangle$, follows a dark eigenstate, e.g. $|\phi_n^0\rangle$, of the time-dependent interaction Hamiltonian. In principle, the time evolution of the system is completely controlled by the variation of this eigenstate. However, a more detailed analysis [38,32] reveals that the eigenstates must change slowly enough to allow adiabatic following. Only if this condition is met, a three-level atom-cavity system prepared in $|\phi_n^0\rangle$ stays there long enough to control the relative population of $|e,n-1\rangle$ and $|g,n\rangle$ by adjusting the pump Rabi frequency Ω. This is obvious for a system initially prepared in $|e,n-1\rangle$. As can be seen from Eq. (13.9), that state coincides with $|\phi_n^0\rangle$ if the condition $2g_0\sqrt{n} \gg \Omega$ is initially met. Once the system has been prepared in the dark state, the ratio between the populations of the contributing states reads

$$\frac{|\langle e,n-1|\Psi\rangle|^2}{|\langle g,n|\Psi\rangle|^2} = \frac{4ng_0^2}{\Omega^2}. \tag{13.19}$$

As proposed in [25], we assume that an atom in state $|e\rangle$ is placed into an empty cavity, which nonetheless drives the $|g,1\rangle \leftrightarrow |x,0\rangle$ transition with the Vacuum-Rabi frequency $2g_0$. The initial state $|e,0\rangle$ therefore coincides with $|\phi_1^0\rangle$ as long as no pump laser is applied. The atom then gets exposed to a laser pulse coupling the $|e\rangle \leftrightarrow |x\rangle$ transition with a slowly rising amplitude that leads to $\Omega \gg 2g_0$. In turn, the atom-cavity system evolves from $|e,0\rangle$ to $|g,1\rangle$, thus increasing the photon number by one. This scheme can be seen as vacuum-stimulated Raman scattering by adiabatic passage, also known as V-STIRAP. If we assume a cavity decay time, κ^{-1} much longer than the interaction time, a photon is emitted from the cavity with a probability close to unity and with properties uniquely defined by κ, after the system has been excited to $|g,1\rangle$.

In contrast to such an idealized scenario, Fig. 13.4d shows a more realistic situation where a photon is generated and already emitted from the cavity during the excitation process. This is due to the cavity decay time being comparable or shorter than the duration of the exciting laser pulse. Even in this case, no secondary excitations or photon emissions can take place. The system eventually reaches the decoupled state $|g,0\rangle$ once the photon escapes. However, the photon-emission probability is slightly reduced as the non-Hermitian contribution of κ to the interaction Hamiltonian is affecting the dark eigenstate $|\phi_1^0\rangle$ of the Jaynes-Cummings triplet (13.9). It now has a small admixture of $|x,0\rangle$ and hence is weakly affected by spontaneous emission losses [32].

13.2.2.3 Single-Photon Emission from Atoms or Ions in Cavities

Many revolutionary photon generation schemes have recently been demonstrated, such as a single-photon turnstile device based on the Coulomb blockade mechanism in a quantum dot [39], the fluorescence of a single molecule [40,41], or a single color center (Nitrogen vacancy) in diamond [42,43], or the photon emission of a single quantum dot into free space [44–46]. All these schemes emit photons upon an external trigger event. However, the

photons are spontaneously emitted into various modes of the radiation field, e.g. into all directions, and they usually show a broad energy distribution. For the same reason, the emission process cannot be described by a Hamiltonian evolution. Hence the process is not reversible, and does not allow for coherent quantum state mapping from source to photon and back. This does not prevent one from using these photons for quantum cryptography and communication, but it represents a major obstacle to many applications in quantum computing or quantum networking. As discussed above most of these limitations can be overcome by cavity-enhanced emission techniques into well-defined modes of the radiation field. Here we focus on these.

Neutral atoms: A straightforward implementation of a cavity-based single-photon source consists of a single atom placed between two cavity mirrors, with a stream of laser pulses traveling perpendicular to the cavity axis to trigger photon emissions. The simplest approach to achieve this is by sending a dilute atomic beam through the cavity, with an average number of atoms in the mode far below one. However, for a thermal beam, the obvious drawback would be an interaction time between atom and cavity far too short to achieve any control of the photon emission time. Hence cold (and therefore slow) atoms are required to overcome this limitation. The author followed this route [47,48], using a magneto-optical trap to cool a cloud of rubidium atoms below 100 μK beneath the cavity. Atoms released from the trap eventually travel through the cavity, either falling from above or being injected from below in an atomic fountain. Atoms enter the cavity randomly, but interact with its mode for 20–200 μs. Within this limited interaction time, between 20 and 200 single-photon emissions can be triggered. Figure 13.5 illustrates this setup, together with the excitation scheme between hyperfine states in ^{87}Rb used to generate single photons by the adiabatic passage technique discussed on Section 13.2.2.2.

Bursts of single photons are emitted from the cavity whenever a single atom passes through the mode of the cavity, and strong antibunching is found in the photon statistics, as shown in Fig. 13.5a. Sub-Poissonian photon statistics are found when conditioning the experiment on the actual presence of an atom in the cavity [49]. In many cases, this is automatically granted—a good example is the characterization of the photons by two-photon interference discussed in section (c.f. Chapter 2). For these experiments, pairs of photons are needed that meet simultaneously at a beamsplitter. With just one source under investigation, this is achieved with a long optical fiber delaying the first photon of a successively emitted pair. With the occurrence of such photon pairs being the precondition to observe any correlation and the probability for successive photon emissions being vanishingly small without atoms, the presence of an atom is actually assured whenever any photon-photon correlations are recorded.

Only lately, refined versions of this type of photon emitter have been realised, with a single atom held in the cavity using a dipole-force trap. McKeever *et al.* [50] managed to hold a single Cs atom in the cavity with a dipole-trapping beam

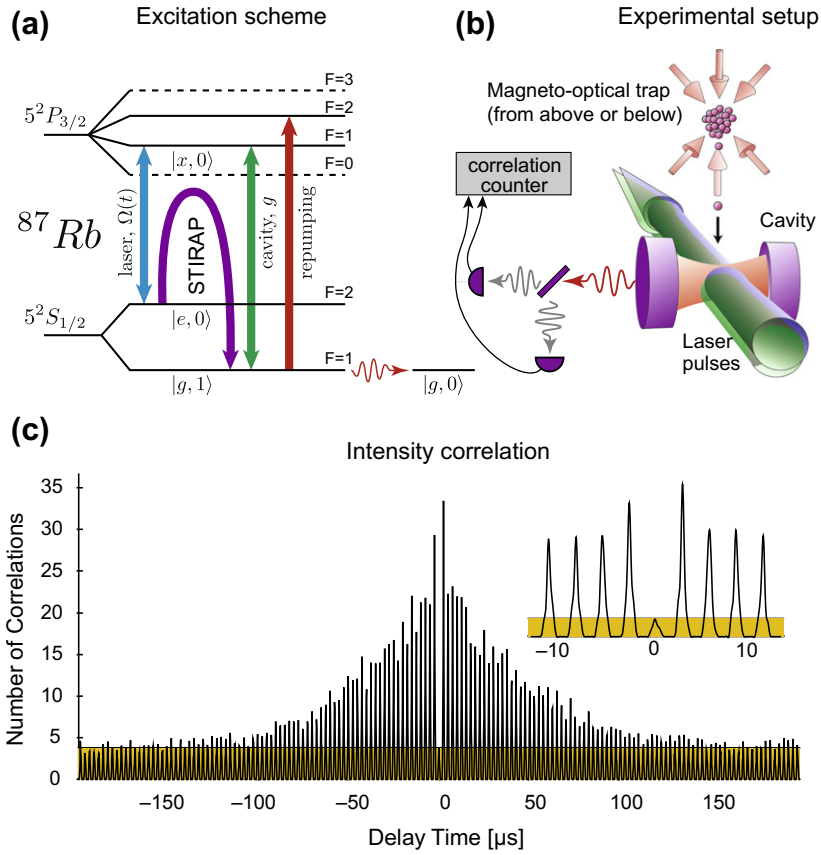

FIGURE 13.5 Single-photon source based on atoms traveling through an optical cavity. (a) Excitation scheme realised in ^{87}Rb for the pulsed single-photon generation. The atomic states labeled $|e\rangle$, $|x\rangle$ and $|g\rangle$ are involved in the Raman process, and the states $|0\rangle$ and $|1\rangle$ denote the photon number in the cavity. (b) A cloud of laser-cooled atoms moves through an optical cavity either from above [47], or from below using an atomic fountain [48]. Laser pulses travel perpendicular to the cavity axis to control the emission process. The light is analysed using a Hanbury Brown & Twiss (HBT) setup with a pair of single-photon avalanche photodiodes. (c) Intensity correlation of the emitted light measured with the HBT setup, with atoms injected using an atomic fountain [48].

running along the cavity axis, while Hijlkema *et al.* [51] use a combination of dipole-trapping beams running perpendicular and along the cavity to catch and hold a single Rb atom in the cavity mode. As illustrated in Fig. 13.6, the trapped atom is in both cases exposed to a sequence of laser pulses alternating between triggering the photon emission, cooling, and repumping the atom to its initial state to repeat the sequence. The atom is trapped, so that the photon statistics are not affected by fluctuations in the atom number and therefore are sub-Poissonian, see Fig. 13.6c. Moreover, with trapping times for single atoms up to a minute, a quasi-continuous bit-stream of photons is obtained.

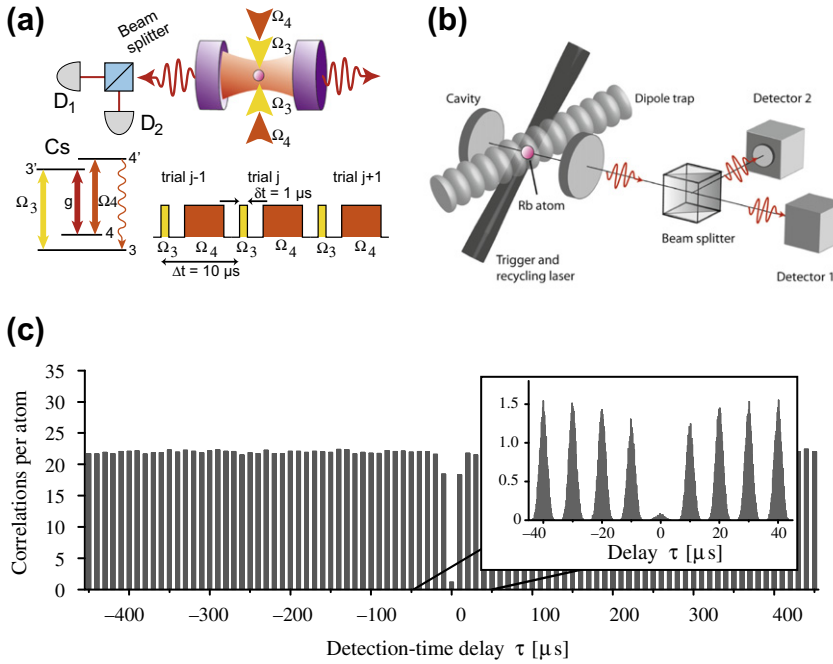

FIGURE 13.6 Atom-cavity systems with a single atom at rest in the cavity mode. (a): The setup by McKeever *et al.* [50] uses a dipole trap oriented along the cavity axis to hold a single Caesium atom in the cavity. The cavity is symmetric, so that half the photons are directed toward a pair of detectors for analyzing the photon statistics. (b): The Kuhn *et al.* uses a dipole trap oriented perpendicular to the cavity axis to hold a single Rubidium atom trapped in the cavity [51]. The cavity is asymmetric, and photons emitted through its output coupler are directed to a pair of photon counters to record the second-order correlation function of the photon stream. In both cases, the trapped atom is exposed to a sequence of laser pulses that trigger the photon emission, cool the atom, and re-establish the initial condition by optical pumping. (c): Intensity correlation function of the light emitted from a trapped-atom-cavity system, as found by the Kuhn *et al.* [51].

The major advantage of using neutral atoms as photon emitters in Fabry-Perot type cavities is that a relatively short cavity ($\approx$100 μm) of high finesse (between 10^5 and 10^6) can be used. One thus obtains strong atom-cavity coupling, and the photon generation can be driven either in the steady-state regime or dynamically by V-STIRAP. This allows one to control the coherence properties and the shape of the photons to a large extent, as discussed in Section 13.2.3.2. Photon generation efficiencies as high as 65% have been reported with these systems. Furthermore, based on the excellent coherence properties, first applications such as atom-photon entanglement and atom-photon state mapping [15–18] have recently been demonstrated.

Apart from the above Fabry-Perot type cavities, many other microstructured cavities have been explored in recent years. These often provide a much smaller mode volume and hence boost the atom-cavity coupling strength by about an

order of magnitude. However, this goes hand-in-hand with increased cavity losses and thus a much larger cavity linewidth, which might conflict with the desired addressing of individual atomic transitions. Among the most relevant new developments are fiber-tip cavities, which use dielectric Bragg stacks at the tip of an optical fiber as cavity mirrors [52,53]. Due to the small diameter of the fiber, either two fiber tips can be brought very close together, or a single fiber tip can be complemented by a microstructured mirror on a chip to form a high-finesse optical cavity. A slightly different approach are ring-cavities realised in solid state, guiding the light in a whispering gallery mode. An atom can be easily coupled to the evanescent field of the cavity mode, provided it can be brought close to the surface of the substrate. Nice examples are microtoroidal cavities realised at the California Institute of Technology [54,55], and bottle-neck cavities in optical fibers [56]. These cavities have no well-defined mirrors and therefore no output coupler, so one usually arranges for emission into well-defined spatio-temporal modes via evanescent-field coupling to the core of an optical fiber.

Trapped ions: Although neutral-atom systems have their advantages for the generation of single photons, such experiments are sometimes subject to undesired variations in the atom-cavity coupling strength and multi-atom effects. Also trapping times are still limited in the intra-cavity dipole-trapping of single atoms. A possible solution is to use a strongly localized single ion in an optical cavity, as was first demonstrated by Keller *et al.* [57]. In their experiment, an ion is optimally coupled to a well-defined field mode, resulting in the reproducible generation of single-photon pulses with precisely defined timing. The stream of emitted photons is uninterrupted over the storage time of the ion, which, in principle, could last for several days.

The major difficulty in combining an ion trap with a high-finesse optical cavity comes from the dielectric cavity mirrors, which influence the trapping potential if they get too close to the ion. This effect might be detrimental if the mirrors become electrically charged during loading of the ion trap, e.g. by the electron beam used to ionize the atoms. Figure 13.7a shows how this problem has been solved in [57] by shuttling the trapped ion from a spatially separate loading region into the cavity. Nonetheless, the cavity in these experiments is typically more than 10–20 mm long to avoid distortion of the trap. Thus the coupling to the cavity is weak, and although optimized pump pulses were used, the single-photon efficiency in [57] did not exceed 8.0(1.3)%. This is in good accordance with theoretical calculations, which also show that the efficiency can be substantially increased in future experiments by reducing the cavity length. It is important to point out that the low efficiency does not interfere with the singleness of the photons. Hence the $g^{(2)}$ correlation function of the emitted photon stream corresponds to the one depicted in Fig. 13.6c, with $g^{(2)}(0) \to 0$. With an improved ion-cavity setup, Barros *et al.* [60] were able to reach a single-photon emission efficiency of 88(17)% in a cavity of comparable length, using a more favorable mode structure in the near-confocal cavity depicted in

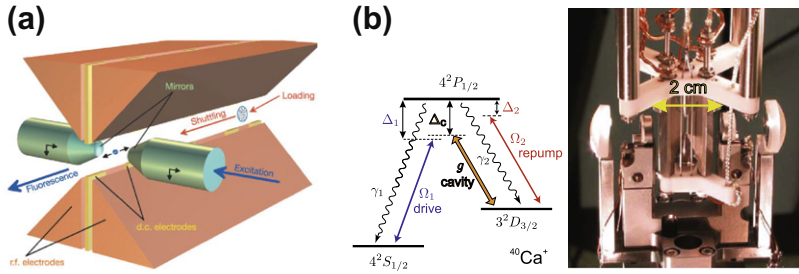

FIGURE 13.7 Arrangement of ion-trap electrodes and cavity in (a) the experiment by Keller *et al.* [57]. The ion is shuttled to the cavity region after loading. Upon excitation of the ion from the side of the cavity, a single photon gets emitted into the cavity mode *(Reprinted by permission from Nature Publishing Group: Nature, Guthöhrlein et al. [58], Copyright 2001)*. The ion-cavity arrangement and excitation scheme in $^{40}Ca^+$ studied by Russo and Barros *et al.* [59,60] in Innsbruck (b) uses a near-concentric cavity which leads to an increased density of otherwise non-degenerate transverse modes *(Panel b adapted with permission from Springer: Applied Physics B, Russo et al. [59], Copyright 2009)*.

Fig. 13.7b and far-off-resonant Raman transitions between magnetic sublevels of the ion.

13.2.3 Photon Coherence, Amplitude, and Phase Control

The vast majority of single-photon applications do not only rely on the deterministic emission of single photons, but also require them to be indistinguishable from one another. In other words, their mutual coherence is often a key element whenever two or more photons are required simultaneously. The most prominent example to that respect is linear optics quantum computing (LOQC) as proposed by Knill *et al.* [2]. Furthermore, with photons used as information carriers, it is common practice to use their polarization, spatio-temporal mode structure or frequency for encoding classical, or quantum state superpositions. To do so, the capability of shaping photonic modes and controlling their coherence properties is essential. Several of these aspects are discussed in the following.

13.2.3.1 Indistinguishability of Photons

At first glance, one would expect any single-photon emitter that is based on a single quantum system of well-defined level structure to deliver indistinguishable photons of well-defined energy. However, this is often not the case for a large number of reasons. For instance, multiple pathways leading to the desired single-photon emission or the degeneracy of spin states might lead to broadening of the spectral mode or to photons in different polarization states, entangled with the atomic spin [15]. Also spontaneous relaxation cascades within the emitter result in a timing jitter of the last step of the cascade,

which is the desired photon emission. Nevertheless, atoms coupled to cavities have been shown to emit nearly indistinguishable photons with well-defined timing. Their coherence properties are normally governed by the dynamics of the Raman process controlling the generation of photons, and—surprisingly—not substantially limited by the properties and lifetime of the cavity mode [61].

Probing photons for indistinguishability is normally done with a two-photon interference experiment of the Hong-Ou-Mandel (HOM) type as discussed in Chapter 2. For two identical photons that arrive simultaneously at different inputs of a 50:50 beamsplitter, they bunch and leave as a photon pair into either one or the other output port. Hence no correlations are found between two detectors that monitor the two outputs. This technique has been well established in connection with photons emitted from spontaneous parametric-down conversion (SPDC) sources, with the correlations between the outputs measured as a function of the *arrival*-time delay between photons.

For the cavity-based emitters discussed here, the situation is somewhat different. The bandwidth of these photons is very narrow, and therefore their coherence time (or length) might be extremely long, i.e. several μs($\approx$100 m). The time resolution of the detectors is normally 3–4 orders of magnitude faster than this photon length, so that the two-photon correlation signal is now determined as a function of the detection-time delay, with the arrival-time delay of the long photons deliberately set to zero [63,62]. This can be regarded as a quantum-homodyne measurement at the single-photon level, with a single local-oscillator photon arriving at one port of a beamsplitter, and a single signal photon arriving at the other port.

Prior to the first photodetection, the two photons arrive simultaneously in the input modes A and B at the beamsplitter and the overall state of the system reads $|1_A 1_B\rangle$. The first photodetection at time t_1 in either output port C or D could have been of either photon, thus the remaining quantum state reduces to

$$|\psi(t_1)\rangle = (|1_A 0_B\rangle \pm |0_A 1_B\rangle)/\sqrt{2}, \tag{13.20}$$

where "+" and "−" correspond to the photodetection in port C and D, respectively. We now assume that the second photodetection takes place $\Delta\tau$ later, at time $t_2 = t_1 + \Delta\tau$, with the input modes A and B having acquired a phase difference $\Delta\phi$ (for whatever reason) during that time span. Hence prior to the second detection, the reduced quantum state has evolved to

$$|\psi(t_2)\rangle = (|1_A 0_B\rangle \pm e^{i\Delta\phi}|0_A 1_B\rangle)/\sqrt{2}. \tag{13.21}$$

By consequence, the probability for the second photon being detected in the same port as the first photon is $P_{\text{same}} = \cos^2(\Delta\phi/2)$, while the probability for the second photon being detected in the respective other beam-splitter port reads

$$P_{\text{other}} = \sin^2(\Delta\phi/2). \tag{13.22}$$

The probability P_{CD} for coincidence counts between the two detectors in the beamsplitter's output ports C and D is therefore proportional to $\sin^2(\Delta\phi/2)$.

Any systematic variation of the phase difference $\Delta\phi$ between the two input modes A and B with time $\Delta\tau$ leads to a characteristic modulation of the coincidence function

$$g^{(2)}_{\mathrm{CD}}(\Delta\tau) = \frac{\langle P_C(t)P_D(t+\Delta\tau)\rangle_t}{\langle P_C\rangle\langle P_D\rangle} \propto \sin^2(\Delta\phi(\Delta\tau)/2). \tag{13.23}$$

A good example is the analysis of two photons of different frequency. We consider one photon of well-defined frequency ω_0 acting as the *local oscillator* arriving at port A at the beamsplitter, and another one of frequency $\omega_0 + \Delta\omega$ which we regard as the *signal photon* arriving simultaneously at port B. Their mutual phase is undefined until the first photodetection at t_1, but then evolves according to $\Delta\phi(\Delta\tau) = \Delta\omega \times \Delta\tau$. In this case, the probability for coincidence counts between the beamsplitter outputs,

$$P_{\mathrm{CD}}(\Delta\tau) \propto \sin^2(\Delta\omega \times \Delta\tau/2), \tag{13.24}$$

oscillates at the difference frequency between local oscillator and signal photon. This phenomenon has been extensively discussed in [61,62] and is also illustrated in Fig. 13.8. Furthermore, the figure shows the effect of random dephasing on the time-resolved correlation function. For photons of 1 μs duration, a 470 ns wide dip is found around $\Delta\tau = 0$. Thereafter, the coincidence probability reaches the same mean value that is found with non-interfering photons of, e.g. different polarization. In this case, we conclude that the dip-width in the coincidence function is identical to the mutual coherence time between the two photons. It is remarkable that it exceeds the decay time of both cavity and atom by one order of magnitude in that particular experiment. This proves that the photon's coherence is to a large extend controlled by the Raman process driving the photon generation, without being limited by the decay channels within the system. We now use a similar system to generate much shorter photons. These have no time to lose their mutual phase relation and the integral two-photon coincidence probability drops to 20% of the reference value found with non-interfering photons. This implies that the photons are nearly indistinguishable and therefore well suited for many-photon interference experiments in linear optics arrangements.

13.2.3.2 Arbitrary Shaping of Amplitude and Phase

From the preceding analysis (see Fig. 13.4) we have seen that the dynamic evolution of the atomic quantum states determines the photon emission probability and thereby also the photon's waveform. This raises the question as to what extent one can arbitrarily shape the photons in time by controlling the envelope of the driving field. This is important for applications such as quantum state mapping, where photon wavepackets symmetric in space and time should allow for a time-reversal of the emission process [19]. Employing photons of soliton-shape for dispersion-free propagation could also help boost quantum communication protocols.

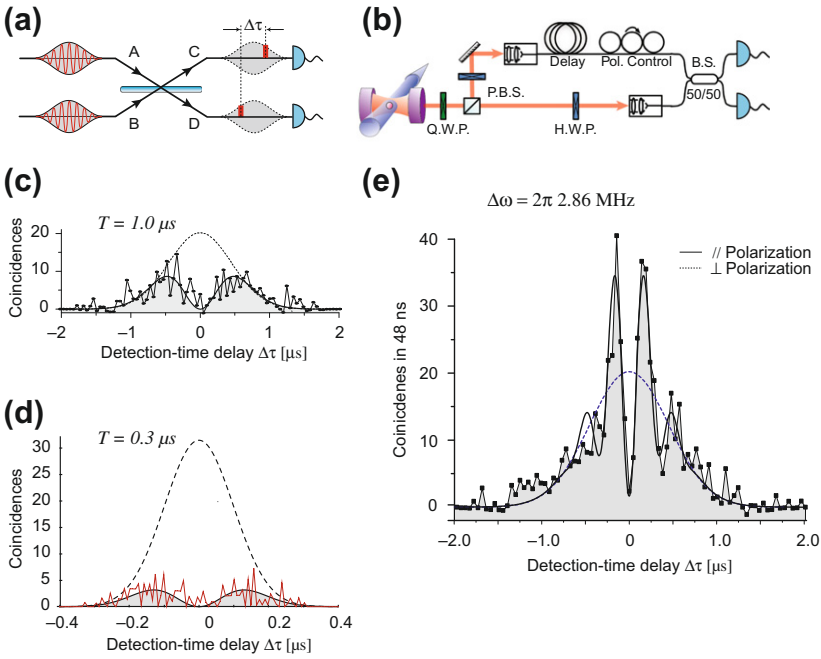

FIGURE 13.8 Time-resolved two-photon interference of photons arriving simultaneously at a beamsplitter (a). With photons emitted successively from one atom-cavity system, this has been achieved using an optical delay line (b). Panel (c) shows the correlation function from [61] for photons of 1.0 μs duration as a function of detection-time delay $\Delta\tau$. A pronounced dip at the origin is found, with the dip-width indicating the photon coherence time. The dotted line shows correlations found if distinguishable photons of perpendicular polarization are used, while the solid line depicts the correlations found if the photon polarization is parallel. Panel (d) shows data from a more recent experiment [48] with photons of 0.3 μs duration. The photons are nearly indistinguishable and the integral two-photon coincidence probability drops to 20% of the reference value found with non-interfering photons. Panel (e) shows data from [61,62] with interfering photons of different frequency. This gives rise to a pronounced oscillation of the coincidence signal as a function of $\Delta\tau$ with the difference frequency $\Delta\omega$.

Photon shaping is normally addressed by solving the Master equation of the atom-photon system, which yields the time-dependent probability amplitudes, and by consequence also the wavefunction of the photon emitted from the cavity [47,57]. Only recently, we have shown [64,21,48] that this analysis can be reversed, giving a unambiguous analytic expression for the time evolution of the driving field in dependence of the desired shape of the photon. This model is not only valid for V-STIRAP in the strong-coupling and bad-cavity regime, but it generally allows control of the coherence and population flow in any Raman process. Designing the driving pulse to obtain photonic wavepackets of any possible desired shape $\psi_{\rm ph}(t)$ is straight forward [64,21]. Starting from the three-level atom discussed on page 9, we consider only the states $|e,0\rangle, |x,0\rangle$,

and $|g,1\rangle$ of the $n = 1$ triplet and their corresponding probability amplitudes $\mathbf{c}(t) = \left[c_e(t), c_x(t), c_g(t)\right]^T$, with the atom-cavity system initially prepared in $|e,0\rangle$. The Hamiltonian (13.7) and the decay of atomic spin and cavity field at rates γ and κ , respectively, define the Master equation of the system,

$$i\hbar\frac{d}{dt}\mathbf{c}(t) = -\frac{\hbar}{2}\begin{pmatrix} 0 & \Omega(t) & 0 \\ \Omega(t) & 2i\gamma & 2g \\ 0 & 2g & 2i\kappa \end{pmatrix}\mathbf{c}(t). \tag{13.25}$$

The cavity-field decay rate unambiguously links the probability amplitude of $|g,1\rangle$ to the desired wavefunction $\psi_{\rm ph}(t)$ of the photon. Furthermore, $|g,1\rangle$ only couples to $|x,0\rangle$ with the well-defined atom-cavity coupling g, while the Rabi frequency Ω of the driving laser links $|x,0\rangle$ to $|e,0\rangle$. Hence the time evolution of the probability amplitudes and $\Omega(t)$ can be written as

$$c_g(t) = \psi_{\rm ph}(t)/\sqrt{2\kappa}, \tag{13.26}$$

$$c_x(t) = -\frac{i}{g}\left[\dot{c}_g(t) + \kappa c_g(t)\right], \tag{13.27}$$

$$\Omega(t)c_e(t) = 2\left[i\dot{c}_x(t) + i\gamma c_x(t) - g c_g(t)\right]. \tag{13.28}$$

We can use the continuity of the system, taking into account the decay of atom polarization and cavity field at rates γ and κ, to get to an independent expression for

$$|c_e(t)|^2 = 1 - |c_x(t)|^2 - |c_g(t)|^2 - \int_0^t dt\left[2\gamma|c_x(t)|^2 + 2\kappa|c_g(t)|^2\right]. \tag{13.29}$$

For an Hamiltonian that does not comprise any detuning and assuming $\psi_{\rm ph}$ to be real, one can easily verify that the probability amplitude $c_x(t)$ is purely imaginary, while $c_e(t)$ and $c_g(t)$ are both real. Hence with the desired photon shape as a starting point, we get analytic expressions for all probability amplitudes. These then yield the Rabi frequency

$$\Omega(t) = \frac{2\left[i\dot{c}_x(t) + i\gamma c_x(t) - g c_g(t)\right]}{\sqrt{1 + c_x^2(t) - c_g^2(t) + \int_0^t dt\left[2\gamma c_x^2(t) - 2\kappa c_g^2(t)\right]}}, \tag{13.30}$$

which is a real function defining the driving pulse required to obtain the desired photon shape.

Figure 13.9 compares some of the results obtained in producing photons of arbitrary wavefunction. The driving laser pulse shown in Fig. 13.9g has been calculated according to Eq. (13.30) to produce the photon shape from Fig. 13.9h. From all the data and calculations, it is obvious that stronger driving is required

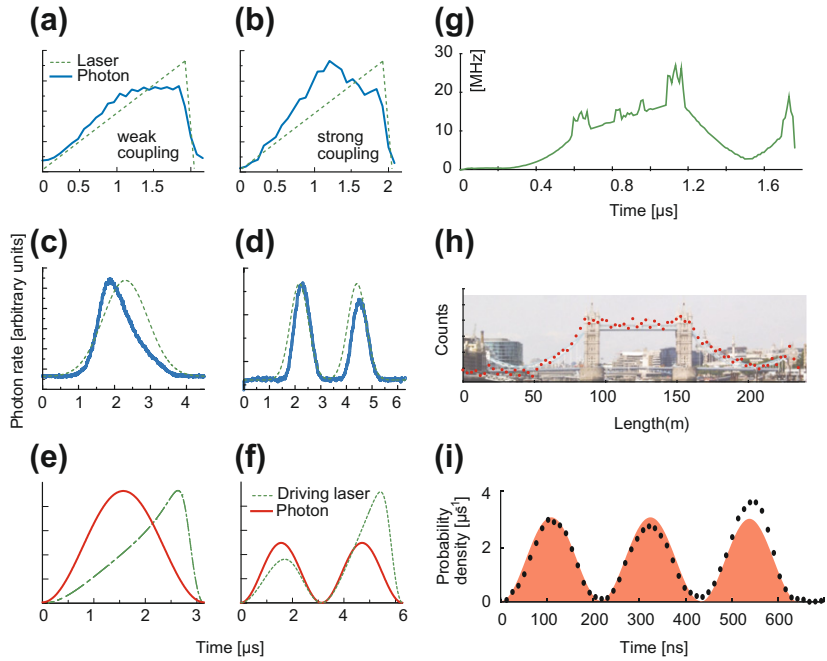

FIGURE 13.9 Photons made to measure: **(a–d)** show photon shapes realised in several experiments and their driving laser pulses. The histogram of the photon-detection time has been recorded for several hundred single-photon emissions. The data shown in **(a + b)** is taken from [47], with neutral atoms falling through a high-finesse cavity acting as photon emitters. The linear increase in Rabi frequency is the same in both cases, and the difference in photon shape is caused by variations in the coupling strength to the cavity. The data shown in **(c + d)** is taken from [57], with a single ion trapped between the cavity mirrors. It shows that the photon shape depends strongly on the driving laser pulse *(Panels c + d adapted with permission from Nature Publishing Group: Nature, M. Keller et al. [57], Copyright 2004)*. **(e + f)** show the Rabi frequency one needs to apply to achieve symmetric single or twin-peak photon pulses with an efficiency close to unity. This is a result from an analytic solution of the problem discussed in [64]. The latter scheme has been applied successfully for generating photons of various arbitrary shapes [48], with examples shown in **(g–i)**.

to counterbalance the depletion of the atom-cavity system. Therefore a very asymmetric driving pulse leads to the emission of photons symmetric in time, and vice versa, as can be seen from comparing Fig. 13.9c and e.

Among the large variety of shapes that have been produced, their possible sub-division into various peaks within separate time-bins is a distinctive feature that allows for time-bin encoding of quantum information. For instance, we recently imprinted different mutual phases on various time bins of multi-peak photons [65], and then successfully retrieved this phase information in a time-resolved quantum-homodyne experiment based on two-photon interference. The latter is illustrated in Fig. 13.10, with subsequently emitted triple-peak

photons from the atom-cavity system arriving simultaneously at a beamsplitter. While the mechanism described above is used to subdivide the photons into three peaks of equal amplitude, i.e. three well-separated time bins or temporal modes, we also impose phase changes from one time bin to the next. The latter is accomplished by phase-shifting the driving laser. Eventually, signal photons get emitted from the cavity that are prepared in a *W*-state with arbitrary relative phases between their constituent temporal modes,

$$|\Psi_{\text{photon}}\rangle = (e^{i\phi_1}|1,0,0\rangle + e^{i\phi_2}|0,1,0\rangle + e^{i\phi_3}|0,0,1\rangle)/\sqrt{3}. \tag{13.31}$$

We may safely set $\phi_1 = 0$, as only relative phases are of any relevance. Every signal photon gets delayed in an optical fiber to arrive simultaneously with a subsequently emitted local-oscillator photon at a beamsplitter. The local-oscillator photon is not subject to phase shifts between its constituents, but is otherwise identical to the signal photon. The time resolution of the photo detectors C and D allows easy identification of whether photons are detected during the first, second, or third peak. The probability for photon-photon correlations is therefore governed by the phase change within the photons–i.e. the probability for correlations between the two detectors monitoring the beam-splitter output depends strongly on the timing of the photodetections. For instance, the coincidence probability $P(C_\text{i}, D_\text{j})$ for detector C clicking in time bin i and detector D in time bin j reads

$$P(C_\text{i}, D_\text{j}) \propto \sin^2((\phi_\text{i} - \phi_\text{j})/2). \tag{13.32}$$

We explored this effect [65] with the experiment illustrated in Fig. 13.10, using two types different signal photons. One with no mutual phase shifts, i.e. $\phi_1 = \phi_2 = \phi_3 = 0$, and the other with $\phi_1 = 0, \phi_2 = \pi, \phi_3 = 0$. In the first case, signal and local oscillator photons are identical. By consequence, no correlations between the two detectors arise (apart from a constant background level due to detector noise). In the second case the adjacent time bins within the signal photon are π out of phase. Therefore the probability for correlations between the two detectors increases dramatically if the detectors fire in adjacent time bins, but it stays zero for detections within the same time bin, and for detections occurring in the first and third time bin. These new findings demonstrate nicely that atom-cavity systems give us the capability of fully controlling the temporal evolution of amplitude and phase within single deterministically generated photons. Their characterization with time-resolved Hong-Ou-Mandel interference used for quantum homodyning the photons then reveals these phases again in the photon-photon correlations.

The availability of time bins as an additional degree of freedom to LOQC in an essentially deterministic photon-generation scheme is a big step toward large-scale quantum computing in photonic networks [66]. Arbitrary single-qubit operations on time-bin encoded qubits seem straightforward to implement with phase-coherent optical delay lines and active optical routing to either

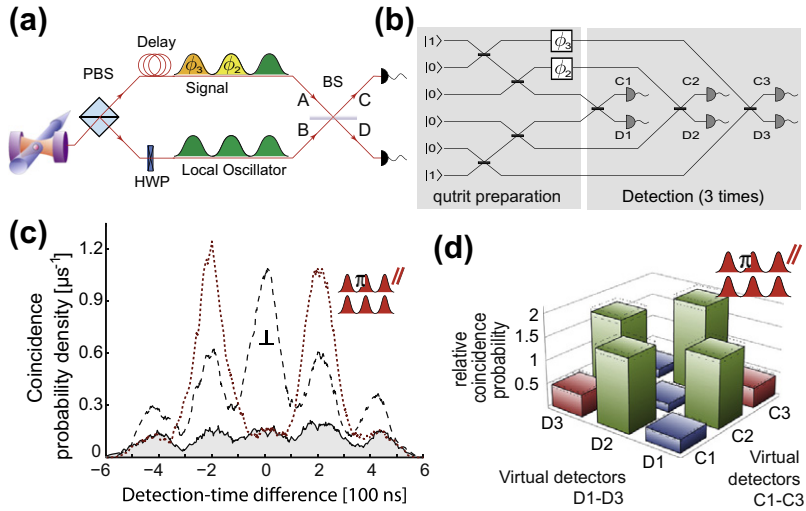

FIGURE 13.10 Qutrits, from [65]: (a) Pairs of triple-peak photons subsequently emitted are delayed such they arrive simultaneously at a beamsplitter. Time-resolved coincidences are then registered between output ports C and D. The signal photon carries mutual phases ϕ_1 and ϕ_2 between peaks, the local oscillator does not. (b) Time-resolved homodyne signal for photons of perpendicular (dashed) and parallel (solid) polarization, with the signal photon having a phase shift in the central time bin of $\phi_1 = \pi$ (dotted). The solid traces result from summing all coincidences found within a 60 ns wide interval around each point of the trace. For some of these data points, the statistical uncertainty is shown. (c) Corresponding virtual circuit if the same experiment was done in the spatial domain. The actual physical system, consisting of one beamsplitter and two detectors, would then correspond to a six-detector setup. All time-resolved photodetections in the real system can be easily associated with the corresponding virtual detectors firing. (d) Relative coincidence probabilities between virtual detectors (diagonal: detections within the same time bin; high columns: detections in successive time bins; outermost columns: detections two time-bins apart).

switch between temporal and spatial modes, or to swap the two time bins. Controlling the atom-photon coupling might also allow the mapping of atomic superposition states to time-binned photons [21,17]; and the long coherence time, combined with fast detectors, makes real-time feedback possible during photon generation.

13.3 SINGLE PHOTONS FROM SEMICONDUCTOR QUANTUM DOTS - G. S. SOLOMON

13.3.1 Introduction

Semiconductor III–V compounds, those made from columns three and five elements of the periodic table, are important for a wide range of optical and

electronic devices. For example, optical devices from these materials range from lasers for telecommunications, for chemical sensing, and for cutting tools; a wide variety of light-emitting diodes, such as those used for lighting; and solar cells. While the success of Si-related devices in electronics is partly due to the high-quality interface between Si and it's insulating oxides, III-V devices owe their success in optoelectronics to high-quality interfaces with compounds of different band-gap energies; for example, AlGaAs and GaAs, and InGaAsP-InP. These defect-free, high-quality interfaces allow for quantum confinement, high-efficiency carrier transport through multiple interfaces and relatively low non-radiative recombination rates.

Invariably, new device applications led researchers to push the accepted boundaries of material combinations, and in the late 1980s this included the highly lattice-mismatched material systems of Ge-Si [67] and InGaAs-GaAs [68]. There has been excellent progress in both of these systems, but at the time quantum wells (QWs) of Ge in Si and high alloy compositions of $In_xGa_{1-x}As$ in GaAs showed troublesome thickness and compositional modulations, leading to excessively broad QW emission and dislocation-induced low quantum efficiency. It was realized that for very thin QWs the interfaces remained planar, after which the QW material began to island and eventually form deleterious dislocations. By the late 1980s and early 1990s groups [69,70] began to see this transitional islanding regime as a route to the formation of fully three-dimensionally confined regions, quantum dots (QDs), in the host crystal. In the InAs-GaAs system, QDs of InAs and InGaAs have been developed as an excellent source of discrete single photons. Single-photon emission from these QDs will be discussed in this section.

13.3.2 InAs-Based Quantum-Dot Formation

In homoepitaxial crystal growth of cubic materials the (1 0 0) growth surface is the lowest-energy facet plane [71]. If the growth temperature and flux rates are appropriate, mobile atoms on the surface, called adatoms, attach to the growth surface at atomic step edges of broad flat regions, for instance at kink and ledge sites, or to the edges of flat island nucleation regions. Thus, the crystal growth proceeds by lateral growth at kinks and ledges, or by the expansion of flat, monolayer-scale high islands. Ideally, as one monolayer is filled, new, monolayer-high nucleation sites are created, and the 2D (1 0 0) growth surface propagates. In most cases, the surface is quasi-2D, extending a few monolayers, yet still dominated by lateral growth through adatom attachment. In contrast, during heterogeneous crystal growth, as more adatoms are deposited onto the growing surface, this growth surface can go through structural changes such as changes in surface reconstruction, surface roughness, or reduced abruptness of a heterointerface [72–75]. In the case of InAs on GaAs, the lattice mismatch is 7.2%. Because of the large lattice mismatch, models generally poorly predict the critical thickness for relaxation by dislocation generation and propagation;

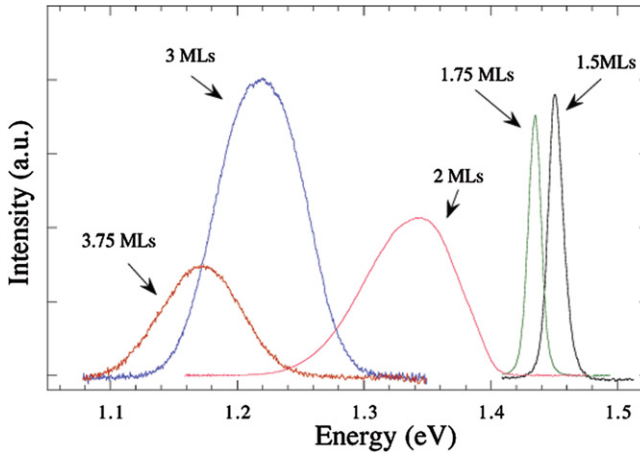

FIGURE 13.11 Photoluminescence (PL) of samples at 8 K containing equivalently planar InAs thickness in GaAs that vary between 1.5 and 3.75 mls. There is a transition from planar growth to quantum island growth between 1.75 and 2 mls. The photoluminescence intensity decrease between 3 and 3.75 mls is due to non-radiative recombination associated with dislocations.

estimates are between 0 and 15 InAs monolayers (mls) depending on the model [76,77]. Because of the similar InAs and GaAs crystal structures, at least one chemisorbed monolayer of InAs can be assumed to be stable on the GaAs substrate. Below the critical thickness or after a chemisorbed layer, a metastable phase can exist. This intermediate growth regime was reported by Stranski and Krastanow in 1938 [78], and is called the Stranski-Krastanow (SK) growth regime. In the SK growth of InAs on GaAs there is a thickness region where the excess strain is partially accommodated by surface islanding. This growth regime is a transitional growth mode between the compliant, planar growth regime that characterizes ideal molecular-beam epitaxy (MBE) growth, and plastically relaxed growth, since as islands grow and merge, the surface area can no longer expand to accommodate the increasing strain energy. It was first observed in semiconductor materials in the Ge-Si system by Eaglesham and Cerullo[79].

Experimentally, as shown in Fig. 13.11, InAs QDs form as islands after a little less than 2 mls of equivalently planar deposition. The islands grow in size and density until about 3.5 mls, where when buried in GaAs, dislocations are observed in transmission-electron microscopy (TEM) [80], and the photoluminescence is diminished [81].

13.3.3 Exciton Energetics

InAs-based islands can be formed dislocation-free, and when subsequently overgrown with a higher band-gap material such as GaAs, high-quality QDs are created. These QDs retain the direct-bandgap character of InAs: conduction-band and valance-band states have aligned minima and maxima in momentum

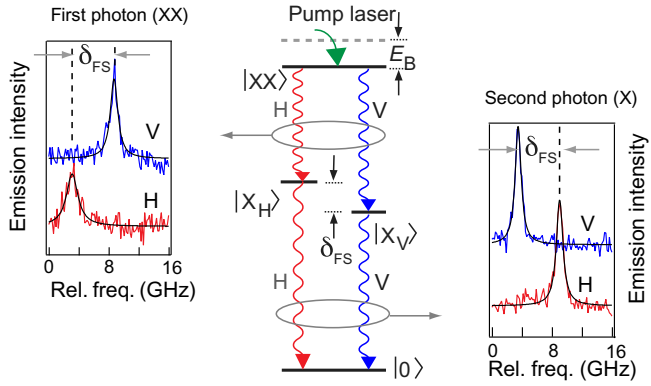

FIGURE 13.12 The decay of the optically active biexciton state, $|XX\rangle$ to the vacuum state, $|0\rangle$, through either of two intermediate single exciton states, $|X_H\rangle$,$|X_V\rangle$. The single exciton states are ideally degenerate, but are often energetically split by δ_{FS}, leading to linearly polarized optical emission, V,H. The relative energies of the two polarizations are switched between the $|XX\rangle$ decay and the $|X|\rangle$ decay. For InAs QDs, the biexciton binding energy is larger than the exciton binding energy (by E_B), so that in general both $|XX\rangle$ decays (left) are redshifted from the $|X\rangle$ decays (right).

space. In addition, conduction-band electrons and valance-band holes created through an excitation process are naturally localized in the three dimensionally confined QD. The single carrier description ignores the interactions between such localized carriers, so a multi-particle (or local polarization) description—the exciton description, is more appropriate. Many-body interactions described by exciton states are important in many semiconductor processes, but because of three-dimensional localization in QDs, they take on added significance—the single particle, electron-hole description cannot be used in any meaningfully way to described QD states. The canonical excitonic Hamiltonian includes the individual free carrier terms described by the band structure within the single particle approximation and two additional terms: a Coulomb term representing the attractive or repulsive nature of the charged carriers, and an exchange term representing the interactions of the constituent spins with each other and the lattice atoms.

In bulk materials, the excitonic spectrum reflects optical transitions based on the principle quantum numbers [82]. This is seen in ensemble measurements of QDs [83], and in more detailed, single-QD spectroscopy [84]. However, because of localization, multi-excitonic states, particularly the biexciton, is pronounced in QD spectroscopy. The biexciton state ($|XX\rangle$) is a single state composed of two electrons and two holes, where additional interactions make it energetically lower than two single excitons. When excited to the optically active biexciton ground state, the system decays optically through two channels to single exciton states, and these optically decay to the vacuum state. See Fig. 13.12.

The single-particle basis states for excitons are based on the symmetry of the crystal and the QDs. Because of quantum confinement, the heavy hole, with its larger effective mass, is the highest occupied valence energy state at the

reciprocal-space zone center (Γ point). The strain in InAs-based QDs breaks the cubic symmetry (Space group $T_d^2 - F43m$) further separating the light- and heavy-hole states (compressive strain). The energy splitting between the two hole states is significant enough so as to neglect the light hole states. The light-heavy hole mixing has been shown theoretically and experimentally to only be on the order of a few percent [85,86]. In addition, the heavy hole-like states also contain a small d-orbital character [87]. While small, the light-heavy hole mixing, and hyperfine interaction of the electron with the nuclei, due to light hole and d-orbital mixing, can relax the selection rules and result in weak but sometime desirable transitions [88]. Thus, the excitons can be constructed from heavy-hole angular moment states $J_h = 3/2, J_{h,z} = \pm 3/2$, and the conduction state electron states $S_e = 1/2, S_{e,z} = \pm 1/2$, where z is aligned to [0 0 1], the growth direction for all QDs discussed here.

Four excitons are formed from the heavy hole and conduction electrons basis states. The [0 0 1] angular momentum projection is ± 2 for two states, and ± 1—the optically active, bright states. Without spin they are degenerate. Using the $\pm|2\rangle$ and $\pm|1\rangle$ states, the exchange Hamiltonian has block diagonal form indicating the dark and bright states do not couple, and furthermore the exchange interaction puts the dark states at lower energy than the bright states by $\approx$150 μeV [89]. Within each block diagonal grouping there is off-diagonal coupling. If the QD has cylindrical symmetry (D_{2d} symmetry), the bright states remain degenerate but the dark states couple, hybridizes into bonding and anti-bonding states [90,91]. However, the usual case is an elliptical in-plane symmetry where the bright states now couple, and the coupling between the dark states can be further altered. The couplings of both the dark and bright states do not produce as large of an energy splitting as the bright-dark separation. This is schematically shown in Fig. 13.13. The optical polarization of these transitions are circular without spin exchange, and the bright state decay remains so with

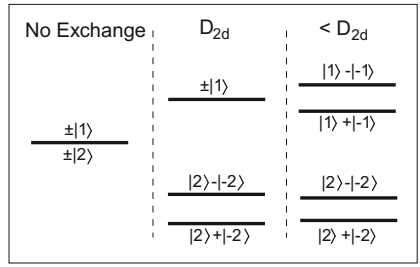

FIGURE 13.13 Schematic diagram of neutral ground state excitons in a QD. With no spin exchange there are four degenerate states, where the two $\pm$ 1 angular momentum states are optically active, and the two $\pm$ 2 angular momentum states are dark. With the inclusion of spin exchange there is an energy splitting between bright and dark states, and the two dark states couple. If the QD does not have cylindrical symmetry ($< D_{2d}$) the bright state also couples and the optical transitions become linearly polarized (see Fig. 13.12).

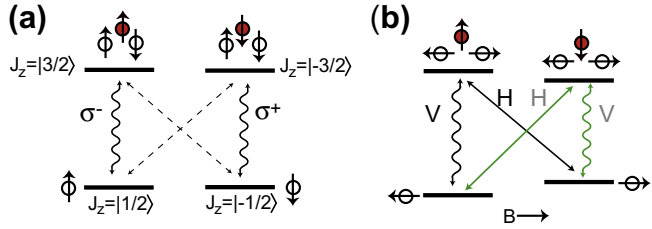

FIGURE 13.14 QD charged exciton decay to a single electron through two circularly polarized transitions (a). Dotted lines indicate ideally forbidden transitions for purely heavy-hole states. (b) In-plane (Voigt configuration) magnetic field splits the electron levels in energy and changes the optical selection rules.

cylindrical symmetry. However, all the neutral exciton transitions are linearly polarized when this symmetry is broken.

The above discussion was for neutral excitons, where the number of electrons and holes are equal; furthermore, it was limited to ground-state excitons and biexcitons. QD emission can result from a variety of excitonic configurations [92,84]. Of the many other types of excitons, the singly charged, ground state exciton, often called a trion, is particularly important. Non-resonantly optically pumping can create excitons, trions and biexcitons. However, without the capture or loss of a charge from the QD, the biexciton—exciton decay cannot yield a trion. The charged exciton can be used in a variety of applications. The energy diagram of the negative trion is shown in Fig. 13.14. For a negative trion with two electrons of opposite spin, there is no spin exchange. The two allowed, optically active transitions are thus circularly polarized. Because the ground state of the decay is an electron or hole, the trion is useful in quantum information, as opposed to the ground state of the neutral exciton manifold which is the vacuum state. When applying an in-plane magnetic field, the degenerate trions are energetically split and the selection rules altered [91]. Thus, the system can be initialized into a particular ground by resonantly or near-resonantly pumping one of the vertically polarized transitions [93]. For instance, in Fig. 13.14, by pumping the lower energy vertical (V) transition, the low-energy electronic ground state can be initialized through the horizontally (H) polarized transition.

13.3.4 Optically Accessing Single Quantum Dots

The ensemble photoluminescence (PL) measurements shown in Fig. 13.11 represent emission from many QDs. To create discrete single photons, individual QD states must be isolated. To resolve individual exciton states, two approaches are used. One uses lithography, typically electron-beam lithography to make etched structures, such as mesas, with dimensions in the 10's to 100's of nanometers. When QD samples are cooled to near liquid He temperatures, the

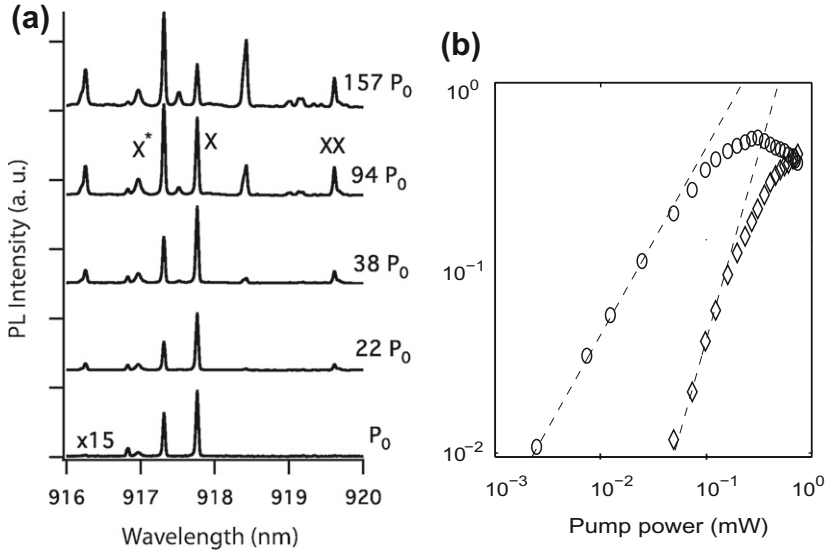

FIGURE 13.15 Photoluminescence of single QD emission with above-bandgap excitation at 4.2 K. (a) The pump power, P_0 is varied and the corresponding spectra are vertically off set for comparison. As the pump power increases the $|XX\rangle$ emission line increases. Notice at higher pump power that the $|X\rangle$ emission intensity begins to decrease. (b) Log-log plot of pump power and PL intensity on a different QD sample. There is a linear rise in $|X\rangle$ emission (circles) and a quadratic rise in the $|XX\rangle$ emission (diamonds) with pump power.

smooth PL peaks in Fig. 13.11 fracture into many small spectral features—evidence of individual QD state decay [94,89,95]. Another approach is to produce samples with dilute QD densities and use near resolution-limited focusing for the PL [96], sometimes with the aid of a solid-immersion lens [97,98]. Often, especially in conjunction with low-mode volume optical cavities, a combination of small structures and low QD density are used. This has historically made the search for QD states aligned both spectrally and spatially to a cavity mode random and time consuming; however, recent improvements using *in situ* optical lithography has made this approach deterministic [99].

In Fig. 13.15 micropost cavities are used in conjunction with low density QD growth for the isolation of single QD states, in a similar manner as in [95,45]. Figure 13.15a shows spectra with above-bandgap excitation at various powers. As the pump power rises the exciton emission intensity rises and the biexciton begins to appear (at $22P_0$). At higher pump powers, the exciton intensity decreases since, on average, the biexcition state population increases in the QD. This is shown in Fig. 13.15b where the log-log plot of intensity versus pump power is shown. The exciton emission saturates and drops, and at the highest powers the biexciton emission intensity is larger than the single exciton emission intensity.

13.3.5 Single Photons From Single Quantum Dots

The lowest-energy excitonic manifold of the quantum dot, containing neutral-exciton, charged-exciton, and biexciton states, has a discrete energy spectrum because of various and strong Coulomb interactions among the confined carriers. Photons result from those excitonic decays having ± 1 changes in angular momentum. These include the two bright excitons, the two charged excitons for each of the positively and negatively charged states, and the bright biexciton. Therefore, within the specific energy region of one of these bright states, single photons will be produced. No more than one photon can be produced at a time from the decay of one of these quasi-particles, and on average one photon should be emitted during the radiative lifetime of the state.

Classical sources of light are from thermal sources where the photons in an optical mode are grouped, or bunched; and lasers, where the photon arrive randomly, i.e. a Poissonian distributed. A semiconductor example of a thermal source is a LED, and an example of a Poissonian distributed source is the semiconductor laser. A Poissonian light source can produce on average one photon in a given time, but this is not our interest. For these light sources, no matter how low their intensity there is always a possibility of having more than one photon emitted.[1] Here, we desire a single-photon source where there is only one photon at a time.

The single-photon character of light can be measured using second-order intensity correlation statistics. It is well-developed in Chapter 2. For time difference $\tau = t_2 - t_1$, between times t_1 and t_2, the second-order correlation function, $g^{(2)}(\tau)$ is defined as

$$g^{(2)}(\tau) = \frac{\langle I(t)I(t+\tau)\rangle}{\langle I(t)\rangle\langle I(t+\tau)\rangle} = \frac{\langle E^*(t)E^*(t+\tau)E(t+\tau)E(t)\rangle}{\langle E^*(t)E(t)\rangle\langle E^*(t+\tau)E(t+\tau)\rangle}, \quad (13.33)$$

where $I(t)$ and $E(t)$ are the intensity and electric field at time t, and $E^*(t)$ is the complex conjugate of the field. $\langle\ \ \rangle$ is the time average. While Eq. (13.33) is second order in intensity, it is fourth order in the field. For single mode fields, the quantum mechanical representation of $g^{(2)}(\tau)$, with photon creation operator, $a^\dagger$ and annihilation operator, a, is

$$g^{(2)}(\tau) = \frac{\langle a^\dagger(t)a^\dagger(t+\tau)a(t+\tau)a(t)\rangle}{\langle a^\dagger(t)a(t)\rangle\langle a^\dagger(t+\tau)a(t+\tau)\rangle}. \quad (13.34)$$

The measurement is made by recording intensity on two detectors as a function of time difference, τ. Note that $g^{(2)}(\tau)$ is not time dependent, but only dependent of the time difference, $t_2 - t_1$. Because detectors have a finite

[1] The Poisson number distribution is $P(n) = (\mu^n/n!)e^{-\mu}$, where $P(n)$ is the probability of the distribution containing n photons, and μ is the mean photon number. For a mean photon number, $\mu = 1$ there is a finite probability of having zero or more than one photon.

response time (or more specifically, dead time), this measurement is usually made using a beamsplitter and two detectors. τ can be positive or negative, and results are typically symmetric around $\tau = 0$. For a coherent field such as a laser, there is equal probability of detecting photons at t and $t + \tau$, and thus $g^{(2)}(\tau) = 1$. For thermal light, there is a higher probability of detecting photons in the same or nearby time windows—the source is *bunched*, and $g^{(2)}(0) = 2$. For single photons, coming from the decay of a single two-level system, like a QD exciton, if a photon is detected, then another photon cannot be emitted from the two-level decay until the upper level is repopulated. For pulsed laser excitation, the upper level is populated only once per pulse. For CW excitation, photon emission will on average occur within the radiative decay time. With either excitation technique, the probability of detecting a photon on each of the detectors at $\tau = 0$ is ideally zero, and the single-photon source is called *anti-bunched*. For more details, see Chapter 2.

An example of a $g^{(2)}(\tau)$ measurement made with a cw pump source is shown in Fig. 13.16. The measurement is made on colloidal QDs made from CdSe cores with a surrounding shell of wider band gap ZnS [44]. The measurements were at room temperature. The upper data were made from an ensemble of many QDs, while the lower data were measured on a single CdSe/ZnS QD. The dip in the coincidence counts gives $g^{(2)}(0) < 1$. If $g^{(2)}(0)$ is below 0.5, the emission can only be explained by a process involving a single emitter. However, for an isolated two-level system emitting discrete single photons, $g^{(2)}(0) = 0$. The anti-bunching shown in Fig. 13.16 can be modeled with an exponential function

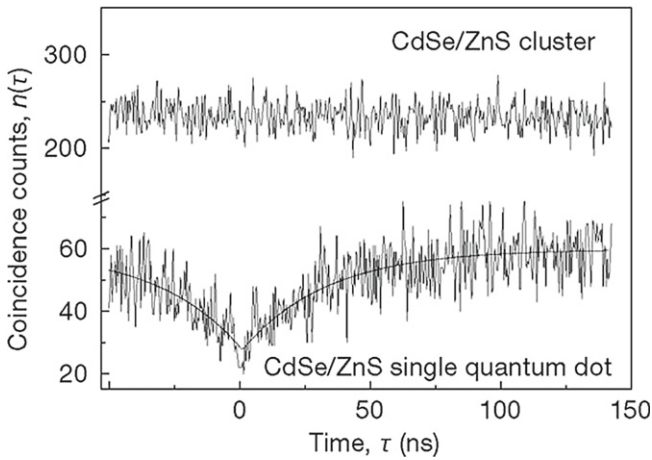

FIGURE 13.16 Second-order correlation counts (unnormalized) of CdSe/ZnS colloidal QDs using cw pumping. (upper data) Measurements on an ensemble of CdSe/ZnS QDs showing no second-order correlation (Poissonian light). (lower data) Measurements on a single QD showing anti-bunching at $\tau = 0$, where τ is the time difference $t_2 - t_1$. From [44]. *Reprinted by permission from Macmillan Publishers Ltd.*

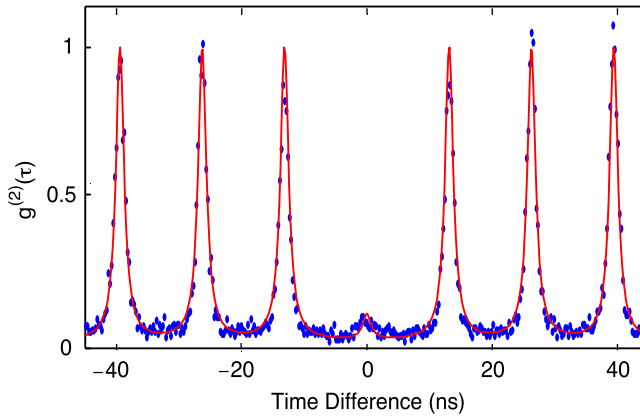

FIGURE 13.17 Second-order correlation measurement of an InAs QD using a 76 MHz repetition rate pump laser. The integrated counts in the time difference, $\tau = 0$ window normalized to nearby peaks is 0.09, which includes the non-zero background floor. *Adapted from [100].*

of the form $g^{(2)}(\tau) = 1 - \mathrm{e}^{-(\Gamma+W_p)\tau}$, where Γ is the radiative recombination rate, and W_p is the pumping rate.

In many fundamental and application-oriented experiments, regulated photons are desired, where by *regulated* we mean the creation of photons synchronized with the pulsed cycle from the pump source. For a regulated single-photon source, we desire just one photon per pulsed cycle. With a pump repetition rate slower than the radiative excitonic decay rate, non-resonant excitation can be used if the excitonic decay is the slowest decay in the total decay process. This generally ensures that only one photon will be emitted from the exciton in each pump cycle. An example of a second-order correlation measurement made using a 76 MHz repetition rate pump laser is shown in Fig. 13.17, where $g^{(2)}(0) \ll 0.5$ is a clear indication of non-classicality, and since $g^{(2)}(0) \approx 0$ this photon emission has very high single-photon purity.

Typically, early measurements of $g^{(2)}(\tau)$ on individual QD photons were made using disk and post microcavities [101,45] where the three-dimensionally confined optical modes improved the collection efficiency because of directional emission and the weak-coupling radiative decay enhancement.[2] Now these three-dimensional cavity—QD systems are used as bright MHz sources of nearly pure single photons [102,103]. Over 80% of the emitted photons are collected and $g^{(2)}(\tau)$ values below 0.15 are obtained [102]. As well, because of improved measurement efficiencies, $g^{(2)}(\tau)$ on single QDs are now often conducted on samples without these strongly confined cavities [100,104], albeit with significantly less collection efficiencies, and often with poorer

[2] For a more detailed development of two-level emitter—optical cavity coupling see Section 13.2.2.1 in this chapter.

indistinguishability. As in Figs. 13.16 and 13.17, these experiments can be pumped non-resonantly, which adds flexibility to single-photon sources; for instance, by significantly simplifying experiments and devices, and allowing different systems to be pumped simultaneously [105]. However, non-resonant pumping also induces variation in the initiation of the exciton decay, leading to reduced indistinguishability [106]. Resonant excitation using π-pulses has been demonstrated, showing excellent $g^{(2)}(0)$ (0.012) and high photon count rates (exceeding 200,000 s^{-1}) [104]. While using a solid-immersion lens, the experiments in Ref. [104] do not use a three-dimensional microcavity. They collect ≈6% of the photons from the QD, which can be improved by an order of magnitude with microdisk or micropost cavity [102].

13.3.6 Weak QD-Cavity Coupling

The QD exciton has a large oscillator strength; and modern GaAs-based crystal growth, lithography and etching lead to high quality-factor, low mode volume cavities; creating an ideal system to study cavity-quantum electrodynamics (CQED) in a solid-state environment.

A significant body of successful and intriguing strong-coupling QD—microcavity research exists, where the cavity and two-level system coherently exchange energy. This is detailed in Section 13.2.2.1 of this chapter. The weak-coupling regime of CQED is a significant component of QD-based single-photon sources [95,107]. The enhanced spontaneous emission decay rate increases the single-photon count rate and often improves the photon indistinguishability. Light from the QD decay preferentially couples to the discrete distribution of optical modes present in these cavities. The optical field intensity of these modes is no longer uniform, and in many cases in these small cavity structures the field intensity can be extremely large. These concepts are also developed from an atom/ion perspective in Section 13.2.2.1 of this chapter. Enhanced emission rates and collection efficiency result from orienting the modes of the modified field to the excitonic dipole of the QD. The radiative decay rate, γ is enhanced or suppressed from the isotropic rate, γ_0 by the spontaneous emission rate enhanced factor (the Purcell factor), f, defined as

$$f = \frac{\gamma}{\gamma_0} = \frac{3Q\lambda_c^3}{4\pi^2 n_e^3 V}\left(\frac{\delta\lambda_c^2}{\lambda_c^2 - 4\left(\lambda_e - \lambda_c\right)^2}\right)\frac{\left|\overline{E}\left(\overline{r}\right)\right|^2}{\left|\overline{E}_{\max}\right|^2}\left(\frac{\overline{d}\cdot\overline{E}\left(\overline{r}\right)}{\left|\overline{d}\right|\left|\overline{E}\left(\overline{r}\right)\right|}\right)^2 + \Im. \tag{13.35}$$

Q is the cavity quality factor, λ_c is the wavelength of the cavity resonance, n_e is the effective index of refraction and V is the cavity mode volume. The three bracketed terms are the spectral, spatial and polarization alignments of the QD exciton with the cavity mode, where $\delta\lambda_c$ and λ_e are the cavity linewidth and excitonic emission wavelength; and $\overline{E}(\overline{r})$ is the electric field at the exciton and $\overline{\mu}$ is the electric dipole of the exciton. Here, we assume that the excitonic linewidth is small compared to λ_c. $\Im$ is the geometric coupling into loss modes. The radiation

lost into these modes, $\gamma_0\Im$ is due to the geometry of these microcavities [95,108]. Emitted light incident on the microcavity edges at angles smaller than the critical angle for total internal reflection will be lost, as well as light incident on the mirrors at an angle greater than the limit of the angular stopband [108]. $\gamma_0\Im$ has been shown to be $\approx$0.3 for small microposts [95]. Besides the wavelength, position and polarization detuning terms, this formulation of f differs from that in Section 13.2.2.1 by the solid-state effective index n_e of the cavity structure, and $\Im$.

The epitaxial growth process used to make strain-induced QDs is well suited for the incorporation of optical microcavities. These microcavities are made by varying combinations of epitaxial crystal growth and processing. For instance, disk microcavities (Fig. 13.18) require a pedestal supporting a disk of typically 2.5–10 μm in diameter. The QDs are centered vertically in the plane of the disk, and are distributed randomly in-plane throughout the disk. Only QDs located near the disk in-plane perimeter couple efficiently to the whispering gallery modes located there. For InAs-based QDs, these layers are made by epitaxial growth and the disk is made by optical lithography. The pedestal layer is usually a high AlAs alloy of AlGaAs so it can be selectively undercut from the GaAs disk. Planar microcavities are also used. They are formed from distributed Bragg reflector (DBR) mirrors separated by a cavity region of $N\lambda/2n$ thickness, where N is an integer. Each DBR mirror is composed of pairs of $\lambda/4n$-thick layers of contrasting refractive index material, so that when many pairs are combined they form a mirror with large effective reflectivity.

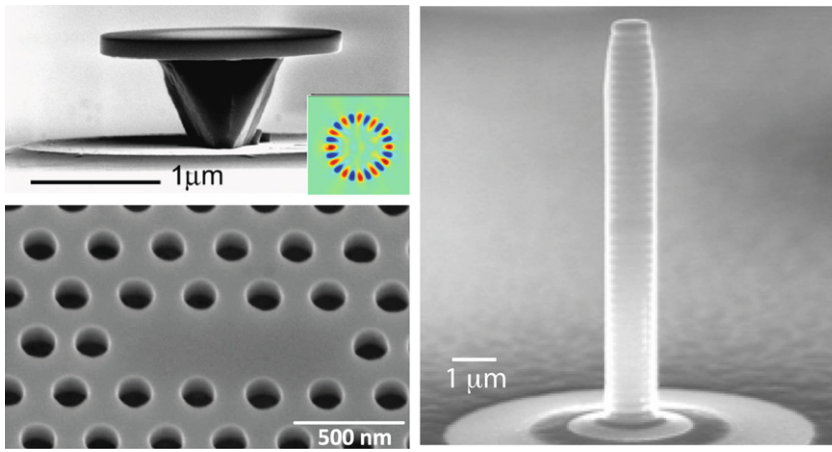

FIGURE 13.18 Three different types of microcavities with InAs quantum dots. (Upper Left) Disk microcavity where the cavity modes of interest are whispering gallery modes at the disk perimeter (top view of the mode structure in the insert). (Lower Left) Photonic crystal cavity, where the cavity is formed from three missing air holes (dark regions). *Adapted from [109].* (Right) Post microcavity formed from alternating AlAs/GaAs layers, lithography and dry etching. The cavity region is the slightly wider, middle gray region. *Reprinted by permission from Macmillan Publishers Ltd: [110].*

For example, GaAs and AlAs, or different alloys of $Al_xGa_{1-x}As$ are often used, where $n_{GaAs} = 3.5$ and $n_{AlAs} = 2.9$. The quality factors for GaAs disk microcavities depend on the diameter, as well as processing. For 2.5 μm diameter microdisks Q's of 10^5 have been reported in transmission [111]. Often the Q is measured through emission of the QD gain medium, and Q's in the 10^4 range are reported [112,113]. Similarly, the single-mode quality factors of DBR planar microcavities are also $\approx 10^5$ [114]. The planar DBR microcavities have a continuous distribution of modes that can be made into a discrete distribution by providing in-plane optical confinement. This is conveniently accomplished by etching posts from the planar DBR cavity, where the refractive index contrast between the semiconductor and air provides the lateral optical confinement, see Fig. 13.18. As discussed in Section 13.2.2.2, the fraction of photons created from the exciton decay that coupled to a single optical mode can be described as

$$\beta = \frac{\gamma}{\gamma_0 + \gamma} = \frac{f}{1+f}. \tag{13.36}$$

For no enhanced emission coupling $\beta = 0.5$, while if the emitter is completely off-resonance with the mode, so that no coupling occurs, $\beta = 0$.[3] Full three-dimensional mode confinement is important, since within the bad cavity limit, as f increases through larger Q and smaller V the single optical-mode coupling increases, and hence light extraction increases. Besides the disk and post microcavity, the photonic crystal cavity (PCC) is another three-dimensional microcavity in common use (Fig. 13.18). The PCC has extremely small mode volume, on the order of $\frac{1}{2}\left(\lambda/n\right)^3$ [115], whereas for the post microcavity, $V \approx 2\left(\lambda/n\right)^3$, and for a disk microcavity, $V \approx 5\left(\lambda/n\right)^3$. In these three types of microcavities the spontaneous emission enhancement factors are in the range of 4–10 [95,101,115].

As the optical fields in these high f, three-dimensionally confined cavities become increasingly localized, it is increasingly unlikely that a QD will be spatially and spectrally aligned with the cavity mode. Thus, many cavity structures need to be evaluated to find good exciton-cavity alignment. One solution is to build the cavities around the QD and two approaches have been used. Through detailed atomic-force microscopy (AFM) an isolated QD can be found, and lithographic marking made to indicate its location. Then, the cavity can be built around this located QD. This approach is useful when the QD is close to the surface. Otherwise, if the QD is far below the surface, the epitaxial growth front will planarize and QDs below cannot be imaged by AFM. This AFM-based approach has been successfully used to align QDs with PCCs [116]. A more recent approach spatially and spectrally images the QD at the near

[3] Other definitions of β are in use. For instance, in [95,107], $\beta \approx 1 - \frac{\gamma_0}{\gamma}$. In this formulation, when there is no decay-rate enhancement, then $\beta = 0$. For enhanced optical-mode coupling, $0 < \beta \leq 1$, and for suppressed mode coupling, $\beta < 0$.

4K measurement temperature after the sample has been covered with optically sensitive resist [99]. After finding exciton emission with good characteristics, they expose the resist, and remove the sample to process post microcavities. Once this lithography is completed, the sample is again cooled to measurement temperature ($\approx 4\ K - 10\ K$) to check the cavity-exciton spectral alignment. A cycle of fine-tuned etching and measurement is repeated until spectral overlap is achieved [99]. Various alternative approaches of patterning QDs in regular arrays by processing the semiconductor sample before QD deposition are also used [117–120], and occasionally this patterning has been incorporated into fully confined microcavities [121].

13.3.7 Quantum-Dot Photon Indistinguishability

Photons emitted from quantum dots can be highly anti-bunched, and with the aid of fully confined microcavities, they can be collected with high efficiency—nearly 80%—and can be delivered with 10^6 repetition rate. Motivated by both fundamental and applied perspectives, we now turn to the question of indistinguishability of the QD photons. While in classical physics identical entities can be distinguishable, in quantum mechanics identical states are fundamentally indistinguishable (see, for example, [122]). Photons are bosonic, and therefore, if a pair of photons are characterized by the same mode of the electromagnetic field, or equivalently if the photons have identical wavepackets, they will coalesce into a single multi-photon state if made to interfere. With the notable exception of the BB84 quantum encryption scheme [123], indistinguishable single photons are a resource critical to the success of many quantum information processing applications [2,19]. The question of indistinguishability is particularly interesting in QDs because of the rich solid-state environment interacting with them.

When two classical fields interfere at a 50-50 beamsplitter, the visibility of the interference seen in the second-order correlation cannot exceed 50% [124]. Since photons follow Bose-Einstein statistics, quantum mechanics says that when identical single photons enter the two ports of a 50/50 beamsplitter, that regardless of their histories, they bunch together, leaving from one of the two output ports as a single two-photon state, rather than each of the two single photons independently choosing an output port (see Chapter 2). As a result, quantum mechanics predicts the probability of joint detection at the two ports is zero, that is, the light is fully anti-bunched. Two-photon bunching was first studied by Hong *et al.* [125]. It is a central concept in quantum optics and has wide applicability, particularly in quantum information science.

In Fig. 13.19 two photons are incident on the two inputs of the beamsplitter (A, B in the figure). Four outcomes are possible and are illustrated in the figure. Of the four, two appear to produce identical results (tt and rr); however, in each of these two cases the photons leaving each port have different origins: The tt and rr cases are only identical when the two input photons

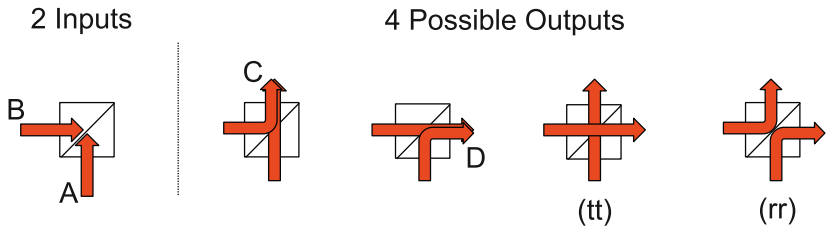

FIGURE 13.19 When two photons are incident on a 50/50 beam splitter (A, B) assuming no losses, there are four possible outcomes. If the two photons are indistinguishable then the (tt) and (rr) cases cancel since transmission and reflection differ by a $\pi/2$ phase shift. The result is the two-photon state, $|\Psi\rangle = \frac{1}{\sqrt{2}}\left(|2,0\rangle + |0,2\rangle\right)$.

are identical. Thus, coalescence probability hinges on the indistinguishability of the photons involved. Since the transmission and reflection coefficients differ by a $\pi/2$ phase shift, the tt and rr probabilities cancel for indistinguishable photons, the two single-photon states coalesce into a two-photon state, $|\Psi\rangle = \frac{1}{\sqrt{2}}\left(|2,0\rangle + |0,2\rangle\right)$.

The original Hong *et al.* [125] experiment showed that when pairs of photons produced by parametric-down conversion (PDC) interfere, the reduction in output coincidence detection can be well below 50%, reaching zero for an ideal source of indistinguishable photon pairs. It could be argued that the photons in the PDC experiment have a common history, because they were emitted in the same fluorescence process [126], which motivated efforts to demonstrate indistinguishable photons from physically distinct processes and sources. Indistinguishability measurements of photons from a QD exciton decay was measured by Santori *et al.* [127]. Because of the enhancement of spontaneous emission decay in the post microcavity, the photon indistinguishability is improved as non-radiative dephasing processes are reduced. The pump laser produces two QD photons from the same excitonic state in the same QD, but separated in time by 2 ns (with a 76 MHz repetition rate). The photons enter a Michelson interferometer with arms of unequal length, see Fig. 13.20a. The difference in arm length is the same 2 ns time difference between the two QD photons. With equal probability, photons can take the short or the long path. There are four options, where photons do not temporally overlap, and one option, represented by peak 3 in Fig. 13.20b where they do overlap. Classically, the probabilities of outcomes represented by peaks 2 and 4 are the same, and differ from peak 3 by a factor of two. However, in Fig. 13.20b the $g^{(2)}(t_2 - t_1)$ at $t_2 - t_1 = 0$ for peak 3 has significantly lower integrated counts than the nearby peaks, 2 and 4. This count suppression is due to the indistinguishability of the two photons. Accounting for imperfections in the measurement system, the two-photon overlap can be as large as 0.8 in [127]. The best results occur with short spontaneous emission lifetimes (90 ps), indicating the importance of the microcavity spontaneous emission enhancement.

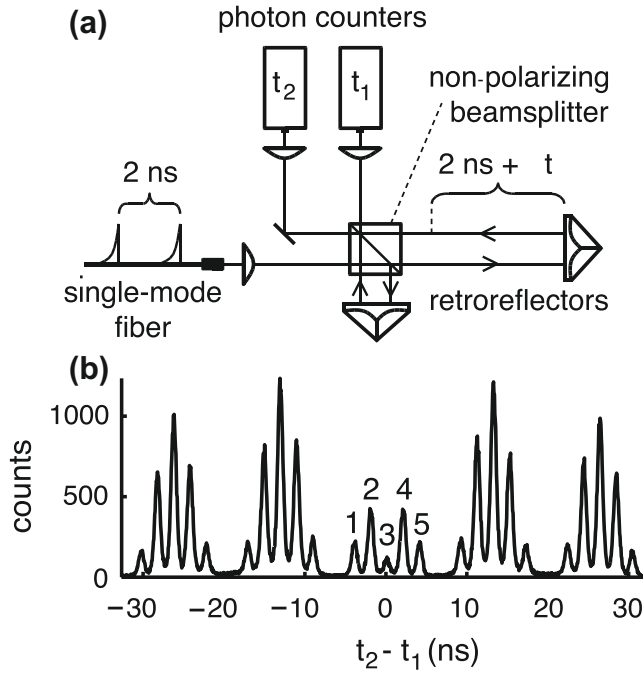

FIGURE 13.20 Two-photon interference from QD exciton photons. (a) Photons separated by 2 ns enter an interferometer, taking one of two paths of different lengths. They reflect at the retroreflectors, again are incident on the beamsplitter, and are detected at photon counters, t_1 and t_2. (b) Five peaks are labeled corresponding to three types of coincidence events. Peak 3 corresponds to the first photon taking the long path and the second photon taking the short path, thus simultaneously arriving at the beamsplitter before exiting the interferometer. The suppression of peak 3 indicates a fraction of the single photons have coalesced into a two-photon state, exiting the same port of the beamsplitter with probability greater than 50%. *From [127].*

The QD photon indistinguishability has also been measured for photons from QD states in different samples. This is fundamentally intriguing because these QD photons share less common history than in the previous single QD experiment, although they still share a common nonresonant pump laser. From an applications perspective, in a distributed quantum information system, photons will likely be emitted from different sources and may even reply on unrelated processes. This means that in many cases photons will require significant manipulation to be made indistinguishable. Recently, Flagg *et al.* observed the interference of photons emitted by two QDs, where each QD is embedded in separate sample (see Fig. 13.21) [100]. This experiment was subsequently done in the diamond NV center system (see Section 13.4).

Flagg *et al.* used different types of cavities for each QD sample. One sample is a planar DBR microcavity with 15.5 lower (10 upper) DBR pairs of GaAs and AlAs; the cavity mode is centered at $\lambda = 920$ nm. The other sample is an

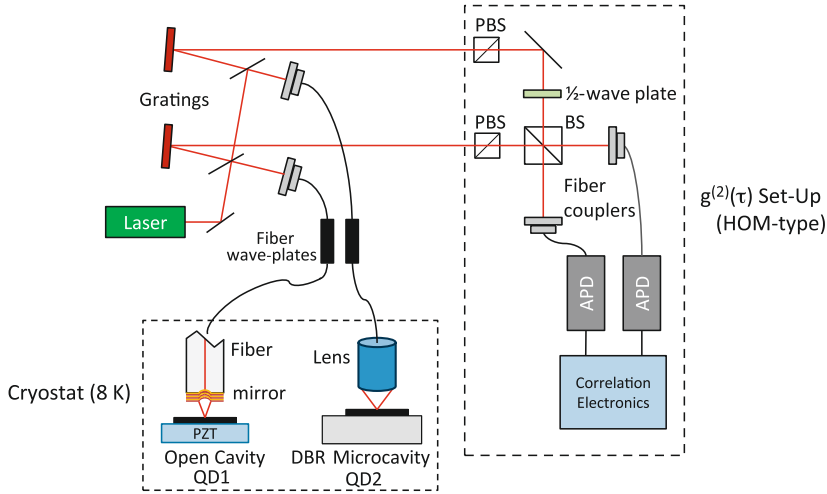

FIGURE 13.21 Schematic of a two-photon interference experiment using InAs QD photons from two different samples [100]. Two cavities at 8 K are used to couple QD photons to the two-photon interference set-up (Hong-Ou Mandel (HOM)-type). A $\frac{\lambda}{2}$ plate rotates the polarization of one input arm to the HOM setup to make the photons completely *distinguishable* as a reference. *Adapted from [100].*

open cavity comprising a lower DBR (35.5 pairs) and an upper external mirror attached to an optical fiber described in [128]. The two types of cavities allow the searching for similar QD states, and the tuning of these states to overlap their emission frequencies. After finding a QD in the fiber-DBR cavity which demonstrated significant anti-bunching and a narrow linewidth, denoted QD1 in Fig. 13.21, the planar DBR microcavity is searched for a second QD, denoted QD2 in Fig. 13.21, whose emission energy is within the $\approx$10 GHz tuning range of QD1's emission. The fiber cavity sample is glued to a piezoelectric transducer (PZT) so that changing the voltage applied to the PZT strains the sample and tunes the emission energy of the QD [129]. Using the PZT, they align the frequencies of the photons emitted by QD1 and QD2.

Both samples are excited by a common mode-locked laser with a repetition rate of 76 MHz (period $\approx$13 ns). The emission from the QDs is coupled through optical fibers to gratings and polarizers, and interferes at the beamsplitter of the $g^{(2)}(\tau)$ setup. The spectral and temporal overlaps for the excitonic photons are shown in Fig. 13.22.

The voltage bias on the PZT of the fiber cavity allows for good overlap. The photon fluxes for each QD are adjusted such that their emission intensities are the same; thus the areas under both curves are equal. The coherence times can be extracted from the linewidths; $T_2^{(\mathrm{QD1})} = 580$ ps and $T_2^{(\mathrm{QD2})} = 390$ ps. The linewidths and lifetimes are not externally controlled. The lifetimes are

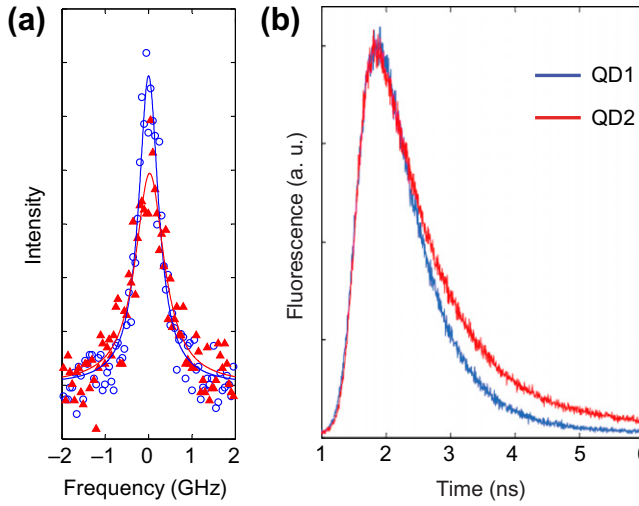

FIGURE 13.22 (a) Spectral alignment of the photons from two QDs at 8 K using a voltage on a piezoelectric transducer to strain-tune one of the QD states. (b) Temporal alignment of the two-photon wavepackets. There is no external tuning in (b). *Adapted from [100]*

$T_1^{(\mathrm{QD1})} = 610$ ps and $T_1^{(\mathrm{QD2})} = 950$ ps. For both QDs, $T_2 < 2T_1$, i.e. the coherence times are not lifetime-limited. Blocking the output from each of the cavities one at a time, the $g^{(2)}(\tau)$ set-up can be used to measure the anti-bunching properties of the individual photons. The $g^{(2)}(0)$ values for the two QD-photons are below 0.1, indicating quite pure single-photon emission.

Despite differences between the QDs in coherence time and lifetime, their photons still interfere. Figures 13.23a and b show the second-order correlation of the light exiting the two output ports of the interferometer for orthogonal and parallel polarizations, respectively. For parallel polarizations, the height of the $\tau = 0$ peak is lower than that for orthogonal polarizations (completely *distinguishable* photons), indicating that photons from the two different QDs have a non-zero coalescence probability. Figure 13.23c shows a close-up of the center peak for both relative polarizations. While the total coincidence counts in the $\tau = 0$ peak is not influenced by the time response of the detectors, the depth of the dip is reduced.

The central dip in Fig. 13.23c is caused by coalescence of the photons. The probability of coalescence is given by $P_c = \frac{A_\perp - A_\parallel}{A_\perp}$, where $A_{\perp,\parallel}$ is the integrated number of counts in $g^{(2)}_{\perp,\parallel}(\tau)$ during one repetition period around $\tau = 0$. From the data in Fig. 13.23 $P_c = 18\%$. Residual counts in the $\tau = 0$ peak remain because the QDs' coherence time is not lifetime-limited [131]. Though the photons' temporal extent is given by the QD lifetimes, T_1, the time over which they can interfere is given by the coherence times, T_2. Thus, the width of the peaks are determined by T_1, and the width of the dip is determined

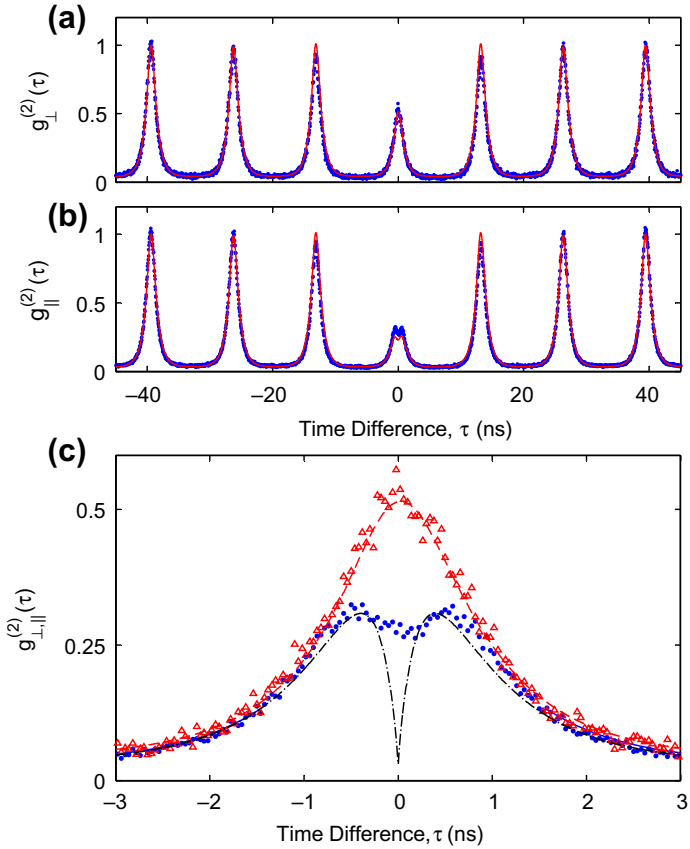

FIGURE 13.23 (a) Correlation of the interference for orthogonal polarizations. (b) Correlation of the interference for parallel polarizations. (c) Close-up of $\tau = 0$ peak for orthogonal (▵) and parallel (•) polarizations. The dash curve in Fig. 13.23c is the result of a simulation based on [130] and shows the shape expected if the detectors were infinitely fast and as expected the single-QD $g^{(2)}(\tau)$ goes to zero at $\tau = 0$. From [100]. (For interpretation of the references to color in this figure legend, the reader is referred to the web version of this book.)

by T_2. If the coherence times were lifetime-limited we would have $T_2 = 2T_1$ and the dip would be wide enough to nearly eliminate the $\tau = 0$ peak. Some residual counts would remain because the two-QD lifetimes are different.

One of the differences between the two-photon interference experiments done by Santori *et al.* using photons from a single excitonic state and the experiment done above on photons from two different states is likely the spontaneous emission enhancement in the first example. Using the fully confined cavity, the radiative lifetime is reduced to 90 ps in one case in the single QD experiment, whereas in the two-QD experiment, fully confined cavities of low mode volume are not used and there is negligible spontaneous emission enhancement.

13.4 SINGLE DEFECTS IN DIAMOND - C. SANTORI

13.4.1 Introduction

Diamond contains hundreds of known optically active defects [132], a few of which have been investigated for single-photon generation and for use as spin-based quantum bits (qubits). Here, we begin by describing in detail the optical and spin properties of the most thoroughly studied defect in diamond, the nitrogen-vacancy (NV) center. While the NV center can be used simply as a single-photon source, it is the possibility of obtaining a single-photon source coupled to a long-lived matter qubit that makes this system exceptional, and of great interest for potential quantum networking and computation applications. We also discuss briefly some other known defects, which can act as brighter single-photon sources, but may not be as useful as spin qubits. We then describe current progress on coupling defects to optical structures such as solid-immersion lenses and microcavities, and finally we describe recent work on using single-photon emission, interference and measurement to entangle the spins of spatially separated spins, a potential route toward scalable quantum computing.

13.4.2 The Nitrogen-Vacancy Center

The nitrogen-vacancy center has, by now, been studied in great detail. This must be in part because the NV center is quite common and easily seen in many types of diamond. But more importantly, the NV center is exceptional in providing an electron spin with long-lived coherence that can be individually addressed at room temperature. These properties have enabled a number of pioneering experiments, including experiments on single-photon generation and quantum key distribution [42,43,133], optically detected magnetic resonance of single electronic and nuclear spins [134–140], magnetometry using single spins as probes [141,142], and most recently, remote entanglement of solid-state qubits [143]. In this section, we review the basic properties of the NV center, the first experiments on single-photon generation using this defect, and its capabilities as a spin qubit. Recent experiments involving quantum communication between NV centers are discussed later, in Section 13.4.5.

13.4.2.1 Structure and Formation

While the spectral signature of the NV center has long been known, the structure of the corresponding defect was established in the 1960s and 1970s through irradiation and annealing experiments combined with optical spectroscopy [144]. As shown in Fig. 13.24a, the NV center consists of a substitutional nitrogen atom next to a missing carbon atom (vacancy) in the diamond lattice. The axis connecting the nitrogen atom to the adjacent vacancy can lie along any of the four (1 1 1) crystallographic directions of the diamond lattice. Since either

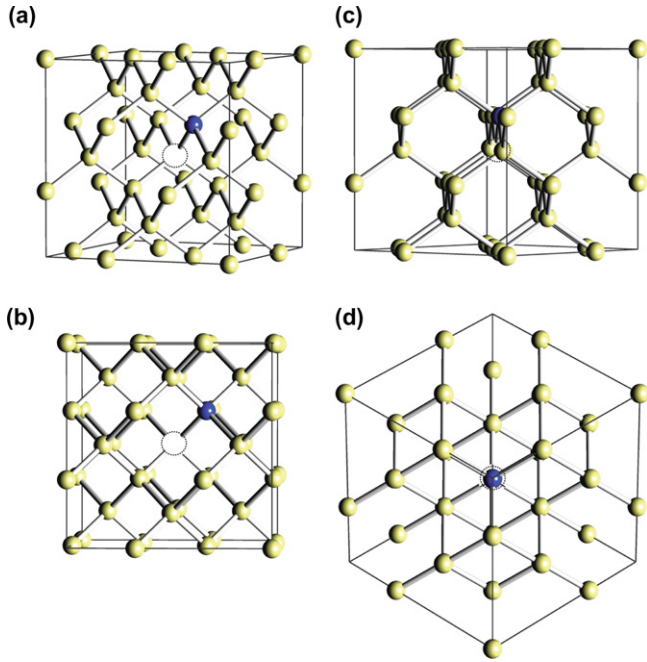

FIGURE 13.24 Structure of the nitrogen-vacancy center in diamond, as seen from (a) a low-symmetry direction, (b) along [1 0 0], (c) along [1 1 0], and (d) along [1 1 1]. The yellow spheres, blue spheres, and dashed circles represent carbon atoms, nitrogen atoms, and vacancies, respectively.

the nitrogen or vacancy can rest at a particular site, a total of eight configurations are allowed. The NV center has trigonal symmetry (point group C_{3v}) with a threefold rotational symmetry about the N-V axis. As discussed below, the NV center has two optical transitions with dipole moments orthogonal to the N-V axis. As a result, the polarization of light emitted by an NV center depends both on the orientation of the N-V axis, and on the direction of the light emission, and hence on the crystal orientation of the polished surface. Figure 13.24b–d illustrates this geometry for diamond samples polished along (1 0 0), (1 1 0), and (1 1 1). For a (1 0 0) surface, the magnitude of the angle between the N-V axis and the surface normal is the same for all orientations, but when collecting light normal to this surface, one will observe preferential polarization along either of two possible directions. For a (1 1 0) surface there are two orientations with the N-V axis parallel to the surface, providing poor optical access, while the other orientations, which are predominantly out-of-plane, have a more favorable collection geometry. For a (1 1 1) surface, there are three N-V orientations with poor optical access, but the fourth orientation has the N-V axis exactly normal to the surface, so that both dipole transitions can be optimally excited, and the emission most efficiently collected.

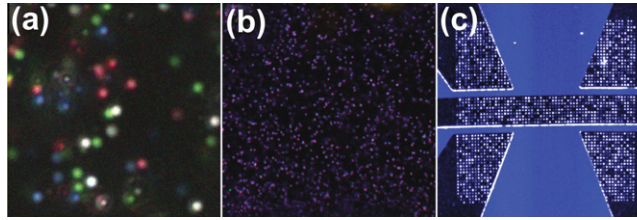

FIGURE 13.25 Confocal microscopy images of NV centers. In (a, b), the dependence of the emission intensity on laser polarization has been encoded into color. (a) NV centers in natural diamond, imaged through a (1 1 1) surface. The four orientations are clearly distinguished through their polarization dependence. Scan size: 12 μm. See Alegre *et al.*, Ref. [145]. (b) NV centers in synthetic diamond grown on a (1 1 0) surface, showing preferential out-of-plane orientation. Scan size: 77 μm. See Edmonds *et al.*, Ref. [146]. (c) NV centers made by nitrogen ion implantation through lithographically defined nano-apertures. *Image courtesy of David Toyli. See also Ref. [154].*

NV centers can be created in several ways. For diamond of a given purity, NV centers created during diamond growth appear to have the best low-temperature optical linewidths and spin coherence properties. Figure 13.25a shows an optical confocal microscopy image of single NV centers in a natural diamond sample. Since the surface of this sample is polished along (1 1 1), the four orientations of NV centers can be uniquely determined through the excitation polarization dependence alone [145]. It has recently been found [146] that in synthetic diamond grown by chemical vapor deposition (CVD) on a (1 1 0) surface, NV centers can be grown preferentially in the two out-of-plane orientations, $[1\ \bar{1}\ \bar{1}]$ and $[\bar{1}\ 1\ \bar{1}]$, as shown in Fig. 13.25b. As mentioned above, if the NV center is excited non-resonantly, or at room temperature, the resulting mixture of light emitted from the two dipole transitions can be collected more efficiently for this geometry than for NV centers below a (1 0 0)-polished surface. It has also been shown that NV centers with good properties can be obtained in thin films grown by CVD [147–149].

To obtain a higher density of NV centers, or to obtain a useful density in ultra-pure diamond with nitrogen concentrations in the part-per-billion range, various implantation and irradiation techniques have been developed. For example, nitrogen ions may be implanted with depths ranging from a few nanometers to a few microns, depending on the chosen accelerating voltage. The sample is then annealed in an oxygen-free environment at temperatures ranging typically from 600 to 1000 °C, where vacancies become mobile and can combine with nitrogen impurities to form NV centers [150–152]. The efficiency of converting an implanted nitrogen atom into an NV center is typically only in the ≈5% range, but may be increased using co-implantation with carbon to increase the number of vacancies [153]. The ion implantation may be performed through a lithographically defined mask [154], as shown in Fig. 13.25c, or through a scanned aperture [155,156], to control the positions where NV centers will form to within a few tens of nanometers. The optical and spin properties of

NV centers formed by nitrogen ion implantation and annealing are typically degraded, compared with as-grown NV centers in the same material. This is thought to result from interactions between the NV center and other defects in its vicinity resulting from implantation damage. Additional high-temperature annealing steps have been developed to recover better properties [157].

One can also convert existing nitrogen into NV centers using MeV electron irradiation to create vacancies, followed by annealing [144,158,159]. While this method, by itself, does not provide control over the position of the NV centers (the electrons can travel for millimeters through the crystal at the energies required to create vacancies), NV centers created by this method can have properties as good as those of NV centers created during crystal growth [160]. Implantation with other particles such as protons, neutrons, helium ions, and gallium ions may also be used [161–164].

None of the methods demonstrated to date can deterministically create a single NV center at a precise location and with a controlled orientation. Even deterministic ion implantation [165,166] would not be sufficient, since the conversion efficiency from an implanted ion to an NV center is low using existing techniques.

13.4.2.2 Optical Transitions and Level Structure

Our current understanding of the NV center is the result of a number of experiments performed over the last few decades that have revealed the detailed level structure. The electron-spin resonance (ESR) signal from spin-triplet states was first reported by Loubser and van Wyk [167]; they also proposed the six-electron model for the negatively charged NV center that is still considered correct. Later, optically detected magnetic resonance (ODMR) [168] and spectral hole-burning [169] experiments established that the spin-triplet states are the ground states of NV^-, and revealed some information about the excited-state structure.

The basic level structure of NV^- is shown in Fig. 13.26. The ground states, denoted $^3A_2$, are formed from a single orbital state with three electron-spin sublevels. Due to a spin-spin interaction, the $m_s = \pm 1$ spin sublevels are approximately 2.88 GHz higher in energy than the lowest-energy $m_s = 0$ spin sublevel. These ground states are connected by optical transitions to a set of six excited states, denoted ^3E_x and ^3E_y, formed from two orbital states and three spin sublevels. The dipole moments of these optical transitions are orthogonal to the N-V axis (defined here to be the z-axis) and to each other. The spontaneous emission lifetime of these excited states is approximately 12 ns. In addition, the black arrows between the ^3E_x and ^3E_y orbital states represent phonon-assisted population relaxation between them, which becomes faster than the spontaneous decay to the ground states at temperatures above $\approx$20 K [170]. The excited states may also decay through a set of spin-singlet states, denoted $^1A_1$ and ^1E. This decay path affects primarily the $m_s = \pm 1$ spin sublevels of

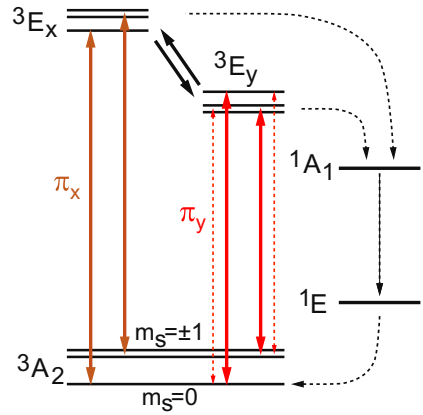

FIGURE 13.26 Schematic energy level diagram of the negatively charged NV center, showing the ground-state spin triplet levels ($^3A_2$), the optically excited triplet levels (^3E_x and ^3E_y), and spin singlet levels ($^1A_1$ and ^1E), along with the π_x- and π_y-polarized optical transitions and additional decay channels.

the excited states [171], and is important for spin polarization and readout of the NV center, as discussed below. This decay path includes a recently discovered optical transition at 1042 nm [172,173]. The lowest-energy singlet state has a relatively long lifetime of ≈200–400 ns, depending on temperature [173,174]. Thus, while the radiative efficiency from the $m_s = 0$ excited states has been estimated to be >0.7 [175], the presence of this fairly long-lived shelving state decreases the overall efficiency of the NV center as a single-photon source.

Figure 13.27 shows typical photoluminescence (PL) spectra from NV centers under various conditions. The spectrum in Fig. 13.27a was obtained from a dense ensemble of NV centers under non-resonant excitation (532 nm) at liquid-helium temperature. The main features that can be seen are the zero-phonon lines (ZPL) from NV^- and NV^0 at 637 nm and 575 nm, respectively, and the associated phonon sidebands (PSB). The dominant emission here is from NV^-, as is often seen in samples with a high concentration of nitrogen impurities. The phonon sideband features arise because of a strong, linear electron-phonon coupling term. Within the Franck-Condon picture, the electronic ground and excited states of the NV center each include a set of vibronic sublevels, corresponding to different motional states of the nuclei near the NV center. If the NV center begins in its electronic excited state and vibronic ground state, and transitions to its electronic ground state and vibronic ground state by emitting a photon (the zero-phonon process), the frequency of the emitted photon is well-defined. On the other hand, if the NV center transitions to an excited vibronic state, one or more phonons are created, and since these phonons have a continuum of energies, the emitted photon has a large spectral bandwidth. The Debye-Waller factor, which measures the fraction of the total

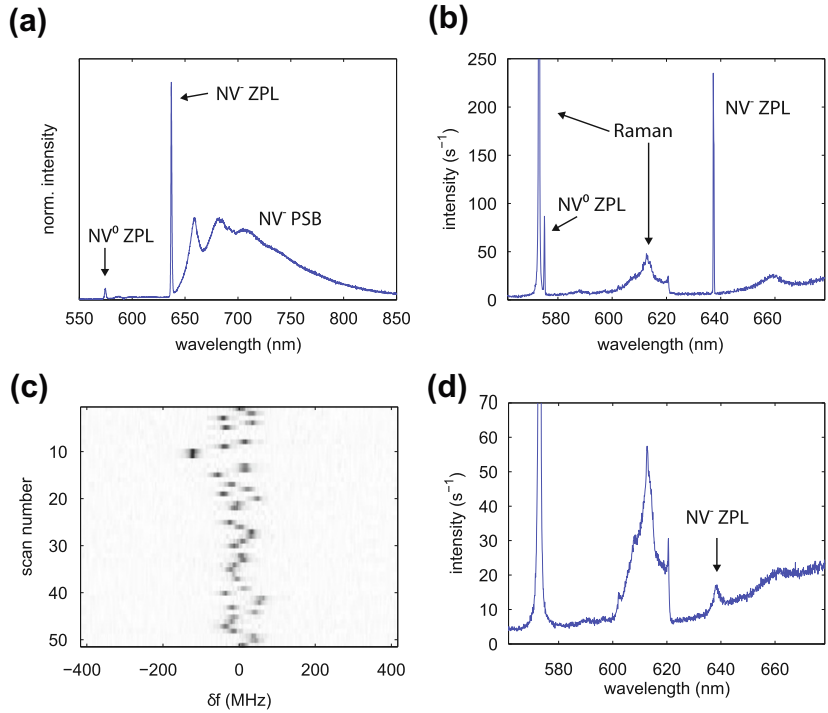

FIGURE 13.27 Typical optical spectra of NV centers: (a) Low-temperature photoluminescence spectrum from a dense ensemble under 532 nm excitation, showing predominantly NV^- emission. Only a few percent of the total emission occurs through the narrow zero-phonon line (ZPL) at 637 nm, with the remainder occurring through broad phonon sidebands (PSB) at longer wavelengths. (b) Low-temperature photoluminescence spectrum of a single NV center under 532 nm excitation, showing both NV^- and NV^0 emission, along with the familiar diamond Raman features of the surrounding crystal. (c) Low-temperature (6 K) photoluminescence excitation spectrum of a single NV center in high-purity diamond containing ≈1 ppb nitrogen, showing a nearly lifetime-broadened single-scan linewidth, with spectral diffusion of ≈100 MHz between scans. In this measurement, an intense 532 nm repump pulse was applied after each scan. Greyness from light to dark represents increased photon emission intensity. (d) Typical room-temperature spectrum from a single NV center, showing a broadened zero-phonon line.

photon emission occurring through the zero-phonon line, is determined by the lattice wavefunction overlap between the ground and excited states, which depends on the strength of the electron-phonon coupling. For NV^-, the Debye-Waller factor is only about 3%, a serious drawback for quantum communication applications requiring spectrally indistinguishable photons.

Figure 13.27b shows a typical PL spectrum obtained from a single NV center under intense (≈1 mW excitation at 532 nm). Even for single NV centers, one typically sees both NV^0 and NV^- emission under such excitation conditions, which cause the charge state to fluctuate rapidly in time. The photo-ionization process driving this charge fluctuation process has recently been studied in

detail [176,177]. The ratio between the NV^- and NV^0 ZPL intensities shown here is typical for high-purity diamond with nitrogen concentration in the part-per-billion range.

The most commonly used technique for measuring the low-temperature linewidth of the zero-phonon transitions is photoluminescence excitation (PLE) spectroscopy. In this technique, a laser is scanned across the zero-phonon lines near 637 nm while the photoluminescence intensity through the phonon sidebands is measured. Figure 13.27c shows such a measurement performed on a single NV center in high-purity diamond. In this measurement, each laser scan lasted 10s, and was followed by an intense repump pulse at 532 nm to reset the charge state. This is necessary to reverse photoionization that occurs eventually under resonant excitation. However, the repump pulse is also the main cause of the spectral jumps of the ZPL frequency that are seen to occur from scan to scan. The single-scan linewidth in this sample is below 20 MHz, close to the Fourier transform limit of 13 MHz [178]. In a simple PLE measurement, one usually sees only a single line, corresponding to excitation from the $m_s = 0$ ground state to the $m_s = 0$ spin sublevel of the upper orbital branch in the excited states. The other transitions are normally hidden due to optical pumping effects, but can be revealed by using either optical modulation [179,180] or microwave excitation [180,181] to reverse optical pumping.

At room temperature, the zero-phonon line becomes much broader, as shown in Fig. 13.27d. The phonon sidebands remain qualitatively similar, the most noticeable change being the appearance of anti-Stokes emission on the blue side of the ZPL in emission. Also, at room temperature, phonon-assisted population relaxation between the excited orbital states occurs so rapidly that these states are effectively "averaged" together, as far as the spin properties are concerned [182–184]. For single-photon generation, another consequence is that photons are emitted with random polarization, π_x or π_y, regardless of the excitation polarization.

The excited-state structure at low temperature has been studied in detail, experimentally [144,169,186,187,178,180,171,181,188,189], theoretically [190–194], and computationally [195,196]. Under perfect C_{3v} symmetry, the excited-state energy levels are determined by a combination spin-orbit and spin-spin interactions. These levels, denoted $E_{1,2}$ (twofold degenerate), $E_{x,y}$ (twofold degenerate), A_1, and A_2, are shown in Fig. 13.28a. However, the random electric fields or strains present even in the best-quality diamond material are typically sufficient to split the energies of the orbital states by $\approx$10 GHz, an amount that is at least comparable to the strength of the spin-orbit and spin-spin interactions. Thus, NV centers with nearly perfect C_3v symmetry are usually found only by extensive searching [181,188] or by applying external fields [178,160,185] to cancel the built-in fields. Figure 13.28b shows an example of using an externally applied electric field to change the orbital splitting. Here, the orbital splitting is seen in emission spectroscopy, using a high-resolution grating-based spectrometer and non-resonant excitation at 532 nm. Under such

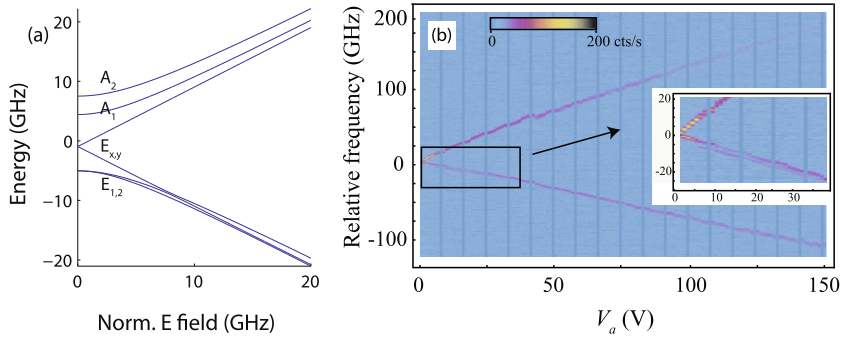

FIGURE 13.28 (a) Theoretical excited-state level structure as a function of electric field, in this case applied normal to the N-V axis and perpendicular to a reflection plane. (b) High-resolution photoluminescence spectra from a single NV center, plotted as a function of voltage applied across microfabricated electrodes on a diamond surface. An orbital splitting of up to 300 GHz is observed. A satellite peak appears in the lower orbital branch at intermediate electric field strengths, corresponding to non-spin-conserving optical transitions. From Acosta *et al.*, Ref. [185]. *Copyright 2012 by The American Physical Society.*

excitation conditions, the spin of the NV center is polarized predominantly into the $m_s = 0$ state. However, for a range of orbital splittings, non-spin-conserving transitions occur in the lower orbital branch, allowing a satellite emission line to appear, corresponding to a transition to the $m_s = \pm 1$ ground states.

By varying the electric and magnetic fields applied to an NV center, a rich variety of energy level structures can be obtained, which can simultaneously include spin-conserving (cycling) transitions and non-spin-conserving transition. It has been shown that the cycling transitions can be used for single-shot readout of the electron spin [189]. The non-spin-conserving transitions can be used for spin initialization [189], to generate spin-photon entanglement [188], for coherent spin manipulation [297], and for electromagnetically induced transparency [298,187,299], with possible applications including quantum memories [200] and magnetometry [299].

13.4.2.3 Single-Photon Generation

The NV center was one of the first solid-state systems to show stable emission of single photons at room temperature. Initial demonstrations of photon antibunching under cw excitation at 532 nm [42] (Fig. 13.29a) or 514 nm [43] were followed by the demonstration of a triggered single-photon source using pulsed laser excitation [133] (Fig. 13.29b). In these room-temperature demonstrations, most of the spectral bandwidth, including the phonon sidebands, was collected in order to obtain a high enough total count rate of $\approx 20{,}000\ \text{s}^{-1}$ for pulsed operation. Thus, the bandwidth of the single photons was ≈ 100 nm or more. Nevertheless, a proof-of-principle demonstration of BB84 quantum cryptography was performed successfully using this source [201].

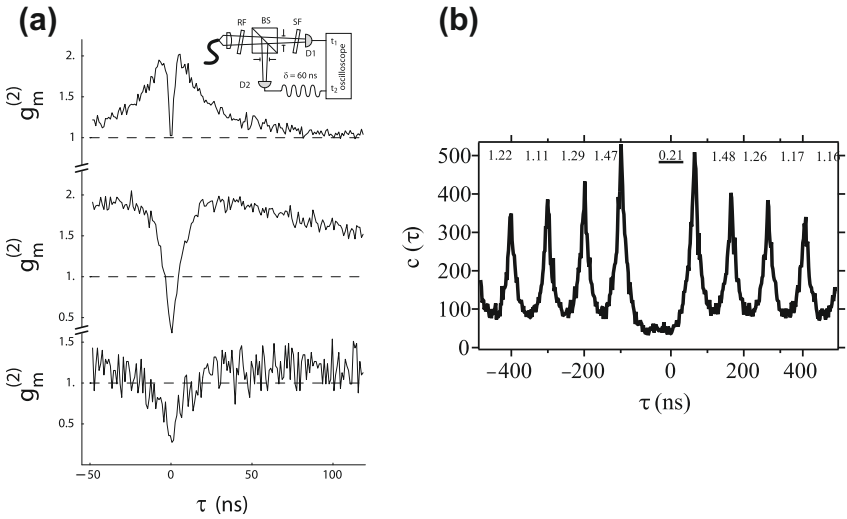

FIGURE 13.29 (a) Early photon antibunching demonstration using an NV center in bulk diamond, excited by a continuous-wave laser, from C. Kurtsiefer *et al.*, Ref. [42]. Copyright 2000 by The American Physical Society. (b) Pulsed single-photon generation from an NV center in a diamond nanocrystal, from Beveratos *et al.*, Ref. [133]. *With kind permission of The European Physical Journal (EPJ)*

As discussed below, nonresonant optical structures have been used to increase the count rate at room temperature by approximately a factor of ten. Diamond nanocrystals also allow for higher collection efficiency since they avoid the problem of total internal reflection at the diamond-air interface. Electrically driven single-photon generation from an NV center in a diamond diode structure has even been demonstrated [260]. The highest reported single-photon count rates from NV centers are now approaching 10^6 s^{-1} [189,202]. Resonant structures can also be used to increase the fraction of light emitted through the narrow zero-phonon line at low temperature to >75% of the total emission [203]. Nevertheless, the NV center appears to have a low overall efficiency, most likely a result of singlet-triplet and charge-state dynamics. Therefore, if one is interested only in generating single photons for applications such as quantum cryptography or linear-optics quantum computation [2], other defects, such as those discussed below, may provide a more ideal two-level structure with correspondingly higher efficiency. The main motivation now for single-photon generation with NV centers is for quantum communication with the long-lived spin states associated with this defect.

13.4.2.4 Spin Properties

Since the first optically detected magnetic resonance (ODMR) experiments were performed on single NV centers [134], it has been realized that the NV

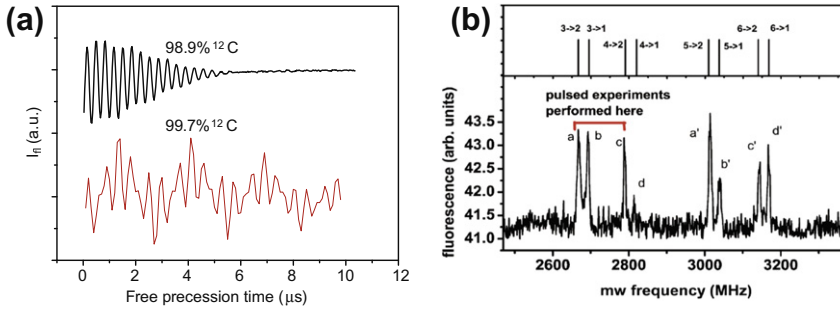

FIGURE 13.30 Optically detected magnetic resonance (ODMR) experiments: (a) Free-induction decay signals from single NV centers in bulk diamond with natural isotopic abundance (top curve), and in isotopically purified diamond (bottom curve). The complicated pattern results from hyperfine coupling between the electronic spin and the nitrogen nuclear spin of the NV center. From G. Balasubramanian *et al.*, Ref. [204]. Reprinted by permission from Macmillan Publishers Ltd: Nature Materials, Copyright 2009. (G. Balasubramanian *et al.*, Nat. Mater. 8, 383–387 (2009).) (b) ODMR spectrum showing hyperfine coupling to a nearest-neighbor ^{13}C nucleus. From Popa *et al.*, Ref. [205]. *Copyright 2004 by The American Physical Society.*

center offered a special combination of long-lived spin coherence and individual addressability. The NV center is particularly well suited for ODMR at room temperature because, as noted above, non-resonant optical excitation results in a high degree of spin polarization into the $m_s = 0$ ground state, ≈ 0.8 [174]. Furthermore, because of the long shelving time in the singlet states, the photoluminescence intensity will initially be higher if the NV center begins in the $m_s = 0$ state, so the PL signal can be used for spin-state readout. Recently, it has been shown that higher initialization fidelities, as well as single-shot readout, can be obtained using resonant excitation at low temperature [189].

Because carbon and silicon consist primarily of isotopes with zero nuclear spin (^{12}C has 98.9% natural abundance and ^{28}Si has 92.2% natural abundance), paramagnetic impurities and defects in these materials can potentially have long-lived electron-spin coherence, provided that the concentration of other paramagnetic impurities is sufficiently low. Figure 13.30a, from Ref. [204], shows two examples of free-induction decay signals obtained from NV centers in high-purity diamond, either with natural isotopic abundance, or isotopically enriched. In such an experiment, the spins are first polarized into the $m_s = 0$ state using a laser pulse, typically of ≈ 1 μs duration. A microwave $\pi/2$ pulse is then applied to create a superposition between the $m_s = 0$ and $m_s = 1$ states. After a variable delay, a second microwave $\pi/2$ pulse is applied, which rotates the state to a new superposition of $m_s = 0$ and $m_s = 1$, with probability amplitudes varying sinusoidally with the delay. A final laser pulse is used to read out the resulting $m_s = 0$ population.

Currently, the best achievable free-induction decay lifetimes measured for single NV centers in isotopically purified materials are $T_2^* \approx 50 - 100$ μs [147]. Using a Hahn echo pulse sequence, in which an additional microwave

π-pulse is applied in between the two $\pi/2$-pulses to cancel magnetic noise that fluctuates on very long timescales, the coherence lifetime can be extended into the millisecond range [204]. Using dynamical decoupling sequences consisting of many microwave pulses, spin coherence lifetimes as long as 0.5 s have been reported [206].

One of the most spectacular achievements using NV centers has been the demonstration of controlled coupling between the electronic spin and one or more nuclear spins. This was first demonstrated using an NV center for which one of the nearest-neighbor carbon atoms is ^{13}C, which has nuclear spin of $1/2$ and a 130 MHz hyperfine coupling with the electronic spin of the NV center. As shown in Fig. 13.30b, from Ref. [205], this hyperfine interaction is easily resolved in an ODMR spectrum, and thus it was possible to implement two-qubit gates between the electronic and nuclear spins [135]. More recently, it has been shown that the spin of the NV center can be controllably coupled to more distant ^{13}C nuclear spins [136,137], or to the nuclear spin of the nitrogen atom of the NV center [138–140]. Thus, the NV center can serve as a quantum "register" in which the electronic spin is used to control or detect several longer-lived nuclear spins. Recently, it has been shown that repeated probing of the electronic spin of an NV center at room temperature can allow single-shot readout of the nitrogen nuclear spin [207]. By combining these capabilities with single-photon generation, it is hoped that quantum repeater systems [208] and methods for scalable computation [209] may be developed.

13.4.3 Other Defects

While the nitrogen-vacancy center is quite interesting as a single-photon source coupled to a long-lived matter qubit, its slow radiative decay, small Debye-Waller factor, and apparently low overall efficiency due to shelving dynamics make it less than ideal if one is interested purely in single-photon generation.

A number of other defects in diamond have recently been investigated which, in some cases, have superior properties for single-photon generation. Much of this work has been summarized in two recent review articles [210,211], but here we briefly summarize some recent developments:

- Silicon-vacancy centers: these have an emission line at 738 nm, and are believed to consist of a silicon atom positioned between two vacancies. The first experiment reporting single-photon emission from this defect used a diamond crystal that was implanted with silicon ions and annealed [212]. This experiment reported a short photoluminescence lifetime of 1.2 ns, but very low count rates of $\approx 10^3$ s^{-1}. However, count rates up to 4.8×10^6 s^{-1} were recently reported for silicon-vacancy centers in nanodiamonds grown on an iridium substrate [213]. This is apparently the highest single-photon count rate measured to date for any defect in diamond. The Debye-Waller

factor was ≈0.8, the room-temperature linewidth was 0.7 nm, and the low-temperature linewidth was 0.17 nm.

- Suspected chromium-related defects: defects with emission lines in the 748 – 760 nm range have recently been discovered in diamond nanocrystals grown on sapphire [214], and in single-crystal diamond implanted with chromium and oxygen ions [215]. Single-photon count rates up to 3.2×10^6 s^{-1} were reported [214], with an 11 nm optical linewidth and a 3.7 ns excited-state lifetime.
- Nickel-related or other defects emitting in the near-infrared: Single-photon emission at 802 nm, with a count rate up to 7.5×10^4 s^{-1}, was reported from a defect identified as the NE8 center [216], thought to consist of a nickel atom next to four nitrogen atoms. Pulsed operation has also been achieved [217]. More recently, an unknown defect was found to emit at 734 nm, with a single-photon count rate as high as 1.6×10^6 s^{-1} [218].
- TR12 color center: This defect, thought to consist of an interstitial carbon atom within the diamond lattice, was recently used for single-photon generation at 470 nm wavelength [219]. The defects were produced through high-energy ion implantation of a diamond crystal.

While the study of these numerous defects in diamond continues, several impurities and defects in materials other than diamond have recently shown promise as single-photon emitters, including defects in silicon carbide [220] and zinc oxide [221], and rare-earth ions in crystals (Pr^{3+}:YAG) [222].

13.4.4 Optical Structures in Diamond

Diamond has a fairly high refractive index of $n \approx 2.4$, and for a dipole emitter placed below a planar diamond-air interface, one theoretically expects only ≈4.4% of the emitted light to escape into air when Fresnel losses are included. If immersion oil with $n = 1.5$ is used, the theoretical escape fraction can increase to ≈12%. Of course, the efficiencies are further reduced for actual microscope objectives with limited collection angles. Furthermore, for defects such as the NV center, only a small fraction of the total emission occurs through the zero-phonon line, which is the only part of the emission that can have a linewidth approaching the Fourier transform limit at low temperature, as needed for quantum communications schemes based on optical interference. Thus, there is a strong motivation to place defects such as the NV center into optical structures, both to increase the photon collection efficiency, and to increase the strength of the zero-phonon emission.

Making optical structures in diamond has been difficult because, unlike in III–V semiconductors, it is difficult to grow single-crystal diamond on other materials, and unlike in silicon, one cannot readily obtain a highly uniform, thin layer of diamond bonded to another transparent material with lower refractive index. Nevertheless, several types of optical structures in diamond have been successfully implemented, and some examples are shown in

Fig. 13.31. The first demonstration of spontaneous emission rate enhancement was achieved by coupling NV centers contained inside diamond nanoparticles to gold nanoparticles [225], shown in Fig. 13.31a. In this work, the spontaneous emission rate was increased by a factor up to 9. Other structures that can increase the collection efficiency by a factor of ≈10 without using narrowband resonances include diamond nanopillars [226] made by reactive-ion etching (Fig. 13.31b), and solid-immersion lenses [223,189] made using a focused ion beam (Fig. 13.31c). The solid-immersion lenses have been particularly successful. They do not require tuning, they can be accurately positioned relative to a pre-selected NV center [227,189], and perhaps most importantly, the NV center can be many microns away from any etched surfaces, and thus can have a high degree of spectral stability.

Figure 13.31d–f show examples of all-dielectric (in these cases diamond) microcavity structures that can support modes with high quality factors and small mode volumes; and thus, can be used to selectively enhance the zero-phonon emission. Figure 13.31d shows a microring cavity [228] coupled to a waveguide [224] for efficient light extraction. In such a device, the zero-phonon emission collected from one of the grating couplers was approximately 25 times as bright as a typical zero-phonon signal from an NV center in the unpatterned membrane. This geometry is especially appealing for the long-term goal of building integrating photonic networks [229]. Figure 13.31e shows a two-dimensional photonic crystal cavity [203]. In a similar device, a spontaneous emission enhancement factor as high as 70 was estimated when the cavity was tuned into resonance with an NV center. The fraction of emission occurring through the zero-phonon was estimated to be 75%, compared with ≈3% for bulk diamond. Figure 13.31e shows a nanobeam photonic crystal cavity made using a newly developed angle-etching technique [230]. This approach seems promising for reducing strain and simplifying the fabrication process.

The examples discussed above represent only a small subset of the approaches that have been tried. Other approaches include photonic crystal cavities made from single-crystal diamond grown on a silicon/Ir/YSZ substrate used to enhance emission from SiV centers [231], structures made using various combinations of focused-ion-beam and reactive-ion etching [232–234], structures made from polycrystalline diamond [235,236], gallium-phosphide structures coupled evanescently to bulk diamond [237–239], and diamond pillars coupled to silica microspheres [240], and diamond nanoparticles coupled to silica microspheres [241–243], silica microdisks [244], and gallium phosphide cavities [245–247].

Despite the significant progress that has been made in coupling single defects to cavities with small mode volumes, spectral diffusion of the optical transitions continues to be an obstacle for the use of these structures in quantum networking applications. In interference-based schemes, the visibility scales as $\gamma_{\mathrm{rad}}/\gamma_{\mathrm{tot}}$, where γ_{rad} is the natural linewidth, and γ_{tot} is the total linewidth including spectral diffusion. In some cases, the increased spectral diffusion linewidth

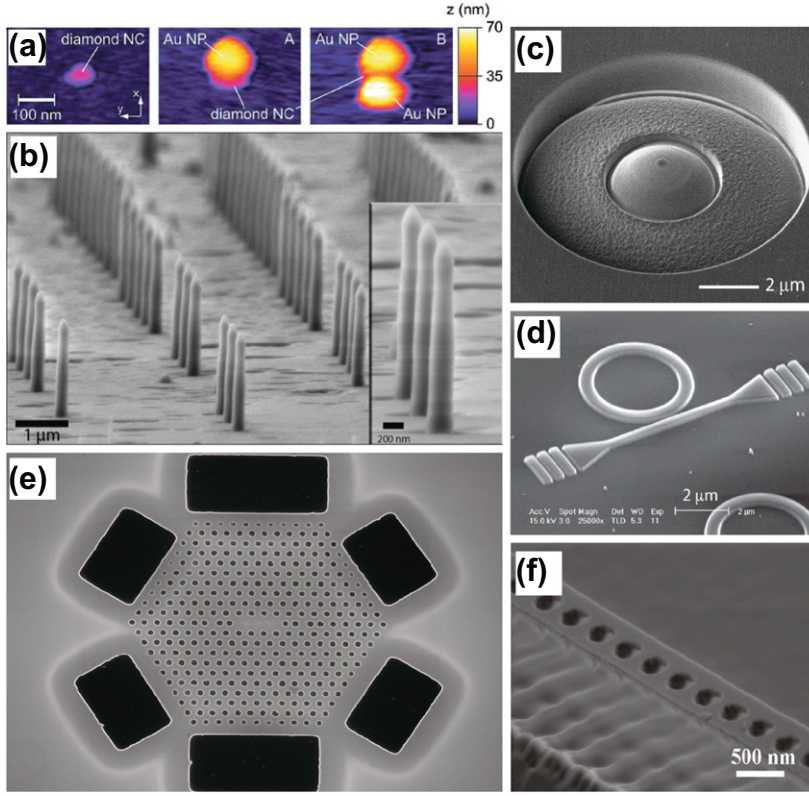

FIGURE 13.31 Optical structures used to enhance NV emission: (a) Gold nanoparticles next to diamond nanoparticles. Reprinted with permission from S. Schietinger, M. Barth, T. Aichele, and O. Benson, Nano Lett. 9, 1694–1698 (2009) [225]. Copyright 2009 American Chemical Society. (b) Diamond nano-pillars. Reprinted by permission from Macmillan Publishers Ltd: Nature Nanotech. T.M. Babinec, B.J.M. Hausmann, M. Khan, Y. Zhang, J.R. Maze, P.R. Hemmer, and M. Loncar, Nat. Nanotechnol. 5, 195–199 (2010) [226], Copyright 2010. (c) Diamond solid-immersion lenses. Courtesy of Sebastian Knauer, J.P. Hadden and Antony C. Stanley-Clarke; see also Ref. [223]. (d) A diamond micro-ring resonator coupled to a waveguide with grating couplers, from Faraon *et al.*, Ref. [224]. (e) A 2D photonic crystal cavity in diamond, from Faraon *et al.*, Ref. [203]. *Copyright 2012 by The American Physical Society.* (f) A nanobeam photonic crystal cavity made by angled reactive-ion etching of diamond. *Reprinted with permission from M.J. Burek, N.P. de Leon, B.J. Shields, B.J. Hausmann, Y. Chu, Q. Quan, A.S. Zibrov, H. Park, M.D. Lukin, and M. Loncar, Nano Lett. 12, 6084–6089 (2012) [230]. Copyright 2012 American Chemical Society.*

caused by proximity to an etched surface can completely offset any gain in collection efficiency. Realizing the full potential of these types of structures will require a combination of materials processing improvements, improved repump methods [176,177] and dynamic compensation [185]. Alternatively, there remains much room to explore structures with larger mode volumes, in which the dipole emitter can be farther from any surfaces.

13.4.5 Quantum Communication

While single NV centers have shown great promise as optically addressable spin qubits, a major challenge in this system (as well as other solid-state defects) is how to connect many qubits together to form scalable networks. Using a photonic network for this purpose could, in principle, allow for nanosecond gate times and micron-scale devices.

At present, numerous schemes have been proposed for quantum-optical networks, including deterministic [19] and nondeterministic (measurement-based) [249,208,250,209] approaches involving single photons. Recent developments suggest that measurement-based approaches may be applied successfully to solid-state defects such as the NV center, if certain technical challenges can be overcome. In Ref. [188], it was shown that if an NV center with nearly ideal C_{3v} symmetry is prepared in its A_2 excited state, the two decay paths, to the $m_s = \pm 1$ ground-state spin levels, emitted photons with orthogonal circular polarization. As a result, the polarization of the emitted photon becomes entangled with the final spin state of the NV center. Separately, as shown in Fig. 13.32, (reprinted from Ref. [248]), two-photon interference was demonstrated for photons emitted by two separate NV centers. Since this can only be observed using the zero-phonon portion of the emitted light, the recent development of solid-immersion lenses in diamond was crucial in obtaining sufficient count rates to perform this experiment. Most recently, two-photon interference from resonantly excited NV centers was used to demonstrate measurement-based entanglement formation between two distant NV centers [248]. The coincidence count rates were such that hours of integration were required to perform this experiment. Nevertheless, this is the first demonstration of its kind in any solid-state quantum system operating at optical frequencies, and represents a significant milestone in the field of solid-state quantum optics.

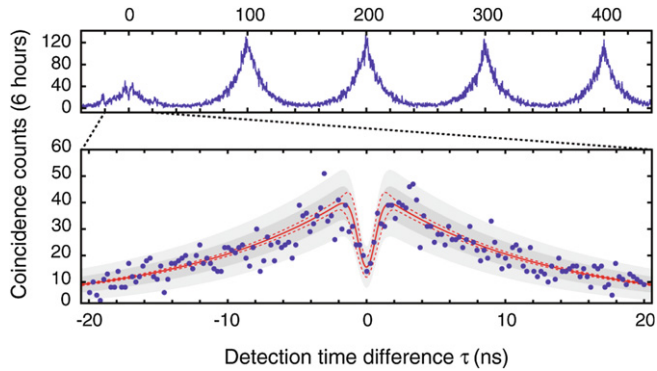

FIGURE 13.32 Demonstration of two-photon interference for light emitted by two different NV centers at low temperature. The drop in coincidences near $\tau = 0$ indicates an interference visibility of $66 \pm 10\%$. From Bernien *et al.*, Ref. [248]. *Copyright 2012 by The American Physical Society.*

Scaling such measurement-based schemes to more than two qubits, or achieving technologically useful entanglement formation rates, will not be easy. As discussed above, the use of resonant cavities to selectively enhance the zero-phonon emission could allow for much higher efficiencies of indistinguishable photon generation. However, resonant structures have their own difficulties: their resonance frequency usually needs to be tuned (experiments so far have used gas condensation inside of a cryostat for tuning), and the spectral stability for NV centers close to an etched structure tends to be degraded. Spectral broadening in turn requires more spectral or temporal filtering to achieve a desired level of photon indistinguishability, and hence lower final count rates. On the other hand, the use of integrated optical networks could allow for stable path lengths (and hence phases) between components. Then, schemes that require only single-photon detection [249,208], but that also require interferometric stability, could be attempted.

13.4.6 Summary

As discussed above, diamond contains a number defects that can be used as optically pumped single-photon sources. Typically, these can operate stably at room temperature, though the spectral linewidth improves with cooling. Some of these defects have yielded single-photon count rates exceeding 10^6 s^{-1}. These may be further improved with the continued development of optical structures and resonators in diamond for enhancing the photon collection efficiency. The NV center is of particular interest because it provides a long-lived spin qubit that is optically addressable at the single-center level. In this system, single-photon emission is a promising route toward quantum communication among a network of spatially separated NV centers, an area of current active research.

13.5 FUTURE DIRECTIONS

We have discussed a variety of ways for producing single photons from simple quantum systems. A large fraction of these photon-production methods lead to on-demand emission of narrowband and indistinguishable photons into a well-defined mode of the radiation field, with efficiencies that can be very close to unity. Therefore these photons are ideal for all-optical quantum computation schemes, as proposed by Knill, Laflamme, and Milburn [2]. These sources are expected to play a significant role in the implementation of quantum networking [19] and quantum communication schemes [251].

The atom- and ion-based sources have already shown to be capable of entangling and mapping quantum states between atoms and photons [15,16]. Processes like entanglement swapping and teleportation between distant atoms or ions, that have first been studied without the aid of cavities [5,252,6,253,254] are beginning to profit enormously from the introduction of cavity-based

techniques [24,17,18], as their success-probability scales with the square of the efficiency of the photon generation process. The high efficiency of cavity-based photon sources also opens new routes toward a highly scalable quantum network, which is essential for providing cluster states in one-way quantum computing [255] and for the quantum simulation of complex solid-state systems [256].

The QD system has benefited from a well-established and well-controlled fabrication process used in the semiconductor industry. This sources are highly efficient, showing nearly 80% efficiency in the emission of single photon out of the device [102], and like single atoms and ions, have excellent single-photon purity. Without employing optical cavities, these sources currently show less than adequate indistinguishability properties. However, based on techniques developed for planar microcavity quantum well devices; for instance, the vertical-cavity surface-emitting laser (VCSEL), the indistinguishability properties become very good [45]. Two-photon-number states have been produced from photons from separate QD states, as well as from a QD and PDC states [100,105]. More recently, entanglement of a spin state (from a QD charged exciton) and a photon has been demonstrated by three groups [257–259]. Like the development of photon sources from NV centers in diamond, this system is less mature than the single atoms and ions, yet progress is coming quickly, and we expect that more advanced demonstrations are on the near horizon.

Finally, diamond hosts a number of defects that can serve as stable single-photon emitters even at room temperature. The NV center in diamond is of particular interest since it provides a long-lived, optically addressable electronic spin coupled to a small number of nuclear spins that can serve as an excellent solid-state memory. This capability, and its potential application to quantum networks, motives the continued development and characterization of devices for efficient single-photon emission in this system.

ACKNOWLEDGMENTS

AK acknowledges partial support by the Engineering and Physical Sciences Research Council (QIP IRC and EP/E023568/1), and the Deutsche Forschungsgemeinschaft (Research Unit 635).

GSS acknowledge partial support from NIST and the NSF Physics Frontier Center at the Joint Quantum Institute. GSS would like to thank A. Muller, E. B. Flagg, T. Thomay, Sergey Polyakov and V. Loo for helpful discussions and experimental contributions.

REFERENCES

[1] D.P. DiVincenzo, "Real and Realistic Quantum Computers," Nature 393, 113–114 (1998).
[2] E. Knill, R. Laflamme, G.J. Milburn, "A Scheme for Efficient Quantum Computing with Linear Optics," Nature 409, 46–52 (2001).

[3] H.J. Kimble, M. Dagenais, L. Mandel, "Photon Antibunching in Resonance Fluorescence," Phys. Rev. Lett. 39, 691–695 (1977).
[4] F. Diedrich, H. Walther, "Nonclassical Radiation of a Single Stored Ion," Phys. Rev. Lett. 58, 203–206 (1987).
[5] B.B. Blinov, D.L. Moehring, L.-M. Duan, C. Monroe, "Observation of Entanglement Between a Single Trapped Atom and a Single Photon," Nature 428, 153–157 (2004).
[6] J. Volz, M. Weber, D. Schlenk, W. Rosenfeld, J. Vrana, K. Saucke, C. Kurtsiefer, H. Weinfurter, "Observation of Entanglement of a Single Photon with a Trapped Atom," Phys. Rev. Lett. 96, 030404 (2006).
[7] S. Olmschenk, D.N. Matsukevich, P. Maunz, D. Hayes, L.-M. Duan, C. Monroe, "Quantum Teleportation Between Distant Matter Qubits," Science 323, 486–489 (2009).
[8] T. Bondo, M. Hennrich, T. Legero, G. Rempe, A. Kuhn, "Time-Resolved and State-Selective Detection of Single Freely Falling Atoms," Opt. Commun. 264, 271–277 (2006).
[9] A. Kuhn, D. Ljunggren, "Cavity-Based Single-Photon Sources," Contemp. Phys. 51, 289–313 (2010).
[10] E.T. Jaynes, F.W. Cummings, "Comparison of Quantum and Semiclassical Radiation Theories with Application to the Beam Maser," Proc. IEEE 51, 89–109 (1963).
[11] B.W. Shore, P.L. Knight, "The Jaynes-Cummings Model," J. Mod. Opt. 40, 1195 (1993).
[12] E.M. Purcell, "Spontaneous Emission Probabilities at Radio Frequencies," Phys. Rev. 69, 681 (1946).
[13] H.J. Carmichael, "Photon Antibunching and Squeezing for a Single Atom in a Resonant Cavity," Phys. Rev. Lett. 55, 2790–2793 (1985).
[14] F. De Martini, G. Innocenti, G.R. Jacobovitz, P. Mataloni, "Anomalous Spontaneous Emission Time in a Microscopic Optical Cavity," Phys. Rev. Lett. 59, 2955–2958 (1987).
[15] T. Wilk, S.C. Webster, A. Kuhn, G. Rempe, "Single-Atom Single-Photon Quantum Interface," Science 317, 488 (2007).
[16] B. Weber, H.P. Specht, J. Bochmann, M. Mücke, D.L. Moehring, G. Rempe, "Photon-Photon Entanglement with a Single Trapped Atom," Phys. Rev. Lett. 102, 030501 (2009).
[17] S. Ritter, C. Nölleke, C. Hahn, A. Reiserer, A. Neuzner, M. Uphoff, M. Mücke, E. Figueroa, J. Bochmann, G. Rempe, "An Elementary Quantum Network of Single Atoms in Optical Cavities," Nature 484, 195–200 (2012).
[18] C. Nölleke, A. Neuzner, A. Reiserer, C. Hahn, G. Rempe, S. Ritter, "Efficient Teleportation Between Remote Single-Atom Quantum Memories," Phys. Rev. Lett. 110, 140403 (2013).
[19] J.I. Cirac, P. Zoller, H.J. Kimble, H. Mabuchi, "Quantum State Transfer and Entanglement Distribution Among Distant Nodes in a Quantum Network," Phys. Rev. Lett. 78, 3221–3224 (1997).
[20] D.P. DiVincenzo, "The Physical Implementation of Quantum Computation," Fortschr. Phys. 48, 771 (2000).
[21] J. Dilley, P. Nisbet-Jones, B.W. Shore, A. Kuhn, "Single-Photon Absorption in Coupled Atom-Cavity Systems," Phys. Rev. A 85, 023834 (2012).
[22] A.D. Boozer, A. Boca, R. Miller, T.E. Northup, H.J. Kimble, "Reversible State Transfer Between Light and a Single Trapped Atom," Phys. Rev. Lett. 98, 193601 (2007).
[23] M. Mücke, E. Figueroa, J. Bochmann, C. Hahn, K. Murr, S. Ritter, C. J. Villas-Boas, G. Rempe, "Electromagnetically Induced Transparency with Single Atoms in a Cavity," Nature 465, 755–758 (2010).
[24] H.P. Specht, C. Nölleke, A. Reiserer, M. Uphoff, E. Figueroa, S. Ritter, G. Rempe, "A Single-Atom Quantum Memory," Nature 473, 190 (2011).
[25] A. Kuhn, M. Hennrich, T. Bondo, G. Rempe, "Controlled Generation of Single Photons from a Strongly Coupled Atom-Cavity System," Appl. Phys. B 69, 373–377 (1999).
[26] N.V. Vitanov, M. Fleischhauer, B.W. Shore, K. Bergmann, "Coherent Manipulation of Atoms and Molecules by Sequential Laser Pulses," Adv. At. Mol. Opt. Phys. 46, 55–190 (2001).
[27] D.J. Heinzen, J.J. Childs, J.E. Thomas, M.S. Feld, "Enhanced and Inhibited Spontaneous Emission by Atoms in a Confocal Resonator," Phys. Rev. Lett. 58, 1320–1323 (1987).
[28] S.E. Morin, C.C. Yu, T.W. Mossberg, "Strong Atom-Cavity Coupling Over Large Volumes and the Observation of Subnatural Intracavity Atomic Linewidths," Phys. Rev. Lett. 73, 1489–1492 (1994).
[29] L.A. Lugiato, "Theory of Optical Bistability," in Progress in Optics, edited by E. Wolf, volume XXI, Elsevier Science Publishers, B. V., 71–216 (1984).

[30] C.K. Law, J.H. Eberly, "Arbitrary Control of a Quantum Electromagnetic Field," Phys. Rev. Lett. 76, 1055 (1996).
[31] C.K. Law, H.J. Kimble, "Deterministic Generation of a Bit-Stream of Single-Photon Pulses," J. Mod. Opt. 44, 2067–2074 (1997).
[32] A. Kuhn, G. Rempe, "Optical Cavity QED: Fundamentals and Application as a Single-Photon Light Source," in Experimental Quantum Computation and Information, edited by F. De Martini, C. Monroe, volume 148, IOS-Press, Amsterdam, 37–66 (2002).
[33] A. Kuhn, M. Hennrich, G. Rempe, "Strongly-Coupled Atom-Cavity Systems," in Quantum Information Processing, edited by T. Beth, G. Leuchs, Wiley-VCH, Berlin, 182–195 (2003).
[34] S.E. Harris, "Electromagnetically Induced Transparency with Matched Pulses," Phys. Rev. Lett. 70, 552–555 (1993).
[35] S.E. Harris, "Electromagnetically Induced Transparency," Phys. Today 50, 36 (1997).
[36] L.V. Hau, S.E. Harris, Z. Dutton, C.H. Behroozi, "Light Speed Reduction to 17 metres per second in an Ultracold Atomic Gas," Nature 397, 594–598 (1999).
[37] D.F. Phillips, A. Fleischhauer, A. Mair, R.L. Walsworth, M.D. Lukin, Storage of Light in Atomic Vapor," Phys. Rev. Lett. 86, 783–786 (2001).
[38] A. Messiah, "Quantum Mechanics," volume 2, J. Wiley & Sons, NY (1958).
[39] J. Kim, O. Benson, H. Kan, Y. Yamamoto, "A Single Photon Turnstile Device," Nature 397, 500–503 (1999).
[40] C. Brunel, B. Lounis, P. Tamarat, M. Orrit, "Triggered Source of Single Photons Based on Controlled Single Molecule Fluorescence," Phys. Rev. Lett. 83, 2722–2725 (1999).
[41] B. Lounis, W.E. Moerner, "Single Photons on Demand from a Single Molecule at Room Temperature, Nature 407, 491–493 (2000).
[42] C. Kurtsiefer, S. Mayer, P. Zarda, H. Weinfurter, "Stable Solid-State Source of Single Photons," Phys. Rev. Lett. 85, 290–293 (2000).
[43] R. Brouri, A. Beveratos, J.-P. Poizat, P. Grangier, "Photon Antibunching in the Fluorescence of Individual Color Centers in Diamond," Opt. Lett. 25, 1294–1296 (2000).
[44] P. Michler, A. Imamoğlu, M.D. Mason, P.J. Carson, G.F. Strouse, S.K. Buratto, "Quantum Correlation Among Photons from a Single Quantum Dot at Room Temperature," Nature 406, 968–970 (2000).
[45] C. Santori, M. Pelton, G. Solomon, Y. Dale, Y. Yamamoto, "Triggered Single Photons from a Quantum Dot," Phys. Rev. Lett. 86, 1502–1505 (2001).
[46] Z. Yuan, B.E. Kardynal, R.M. Stevenson, A.J. Shields, C.J. Lobo, K. Cooper, N.S. Beattie, D.A. Ritchie, M. Pepper, "Electrically Driven Single-Photon Source," Science 295, 102–105 (2002).
[47] A. Kuhn, M. Hennrich, G. Rempe, "Deterministic Single-Photon Source for Distributed Quantum Networking," Phys. Rev. Lett. 89, 067901 (2002).
[48] P.B.R. Nisbet-Jones, J. Dilley, D. Ljunggren, A. Kuhn, "Highly Efficient Source for Indistinguishable Single Photons of Controlled Shape," New J. Phys. 13, 103036 (2011).
[49] M. Hennrich, T. Legero, A. Kuhn, G. Rempe, "Photon Statistics of a Non-stationary Periodically Driven Single-Photon Source," New J. Phys. 6, 86 (2004).
[50] J. McKeever, A. Boca, A.D. Boozer, R. Miller, J.R. Buck, A. Kuzmich, H.J. Kimble, "Deterministic Generation of Single Photons from One Atom Trapped in a Cavity," Science 303, 1992–1994 (2004).
[51] M. Hijlkema, B. Weber, H.P. Specht, S.C. Webster, A. Kuhn, G. Rempe, "A Single-Photon Server with Just One Atom," Nat. Phys. 3, 253–255 (2007).
[52] Y. Colombe, T. Steinmetz, G. Dubois, F. Linke, D. Hunger, J. Reichel, Strong Atom-Field Coupling For Bose-Einstein Condensates in an Optical Cavity on a Chip, Nature 450, 272–276 (2007).
[53] M. Trupke, J. Goldwin, B. Darquié, G. Dutier, S. Eriksson, J. Ashmore, E.A. Hinds, "Atom Detection and Photon Production in a Scalable, Open, Optical Microcavity," Phys. Rev. Lett. 99, 063601 (2007).
[54] B. Dayan, A.S. Parkins, T. Aoki, E.P. Ostby, K.J. Vahala, H.J. Kimble, "A Photon Turnstile Dynamically Regulated by One Atom," Science 319, 1062–1065 (2008).
[55] T. Aoki, A.S. Parkins, D.J. Alton, C.A. Regal, B. Dayan, E. Ostby, K.J. Vahala, H.J. Kimble, "Efficient Routing of Single Photons by One Atom and a Microtoroidal Cavity," Phys. Rev. Lett. 102, 083601 (2009).

[56] M. Pöllinger, D. O'Shea, F. Warken, A. Rauschenbeutel, "Ultrahigh-Q Tunable Whispering-Gallery-Mode Microresonator," Phys. Rev. Lett. 103, 053901 (2009).
[57] M. Keller, B. Lange, K. Hayasaka, W. Lange, H. Walther, "Continuous Generation of Single Photons with Controlled Waveform in an Ion-Trap Cavity System," Nature 431, 1075–1078 (2004).
[58] G.R. Guthörlein, M. Keller, K. Hayasaka, W. Lange, H. Walther, "A Single Ion as a Nanoscopic Probe of an Optical Field," Nature 414, 49–51 (2001).
[59] C. Russo, H. Barros, A. Stute, F. Dubin, E. Phillips, T. Monz, T. Northup, C. Becher, T. Salzburger, H. Ritsch, P. Schmidt, R. Blatt, "Raman Spectroscopy of a Single Ion Coupled to a High-Finesse Cavity," Appl. Phys. B 95, 205–212 (2009).
[60] H.G. Barros, A. Stute, T.E. Northup, C. Russo, P.O. Schmidt, R. Blatt, "Deterministic Single-Photon Source from a Single Ion," New J. Phys. 11, 103004 (2009).
[61] T. Legero, T. Wilk, M. Hennrich, G. Rempe, A. Kuhn, "Quantum Beat of Two Single Photons," Phys. Rev. Lett. 93, 070503 (2004).
[62] T. Legero, T. Wilk, A. Kuhn, G. Rempe, "Characterization of Single Photons Using Two-Photon Interference," Adv. At. Mol. Opt. Phys. 53, 253 (2006).
[63] T. Legero, T. Wilk, A. Kuhn, G. Rempe, "Time-Resolved Two-Photon Quantum Interference," Appl. Phys. B 77, 797–802 (2003).
[64] G.S. Vasilev, D. Ljunggren, A. Kuhn, "Single Photons Made-to-Measure," New J. Phys. 12, 063024 (2010).
[65] P.B.R. Nisbet-Jones, J. Dilley, A. Holleczek, O. Barter, A. Kuhn, "Photonic Qubits, Qutrits and Ququads Accurately Prepared and Delivered on Demand," New J. Phys. 15, 053007 (2013).
[66] A.J. Bennett, D.G. Gevaux, Z.L. Yuan, A.J. Shields, P. Atkinson, D.A. Ritchie, "Experimental Position-Time Entanglement with Degenerate Single Photons," Phys. Rev. A 77, 023803 (2008).
[67] D.J. Eaglesham, M. Cerullo, "Low Temperature Growth of Ge on Si(100)," Appl. Phys. Lett. 58, 2276–2279 (1991).
[68] B. Elman, E.S. Koteles, P. Melman, C. Jagannath, J. Lee, D. Dugger, In-situ Measurements of Critical Layer Thickness and Optical Studies of InGaAs Quantum Wells Grown on GaAs Substrates," Appl. Phys. Lett. 55, 1659–1661 (1989).
[69] M. Tabuchi, S. Nodaand, A. Sasaki, "Mesoscopic Structure in Lattice-Mismatched Heteroepitaxial Interface Layers," in Science and Technology of Mesoscopic Structures, edited by S. Namba, C. Hamaguchi, T. Ando, Springer-Verlag, Tokyo, Japan, 379–384 (1992).
[70] D. Leonard, M. Krishnamurthy, C.M. Reaves, S.P. Denbaars, P.M. Petroff, "Direct Formation of Quantum-Sized Dots from Uniform Coherent Islands of InGaAs on GaAs Surfaces," Appl. Phys. Lett. 63, 3203–3205 (1993).
[71] W.A. Tiller, "The Science of Crystallization: Microscopic Interfacial Phenomena," Cambridge University Press, Cambridge, England (1991).
[72] H. Gao, "A Boundary Perturbation Analysis For Elastic Inclusions and Interfaces," Int. J. Solids Struct. 28, 703–725 (1991).
[73] L.B. Freund, F. Jonsdottir, "Instability of a Biaxial Stressed Thin Film on a Substrate Due to Material Diffusion," J. Mech. Phys. Solids 41, 1245–1264 (1993).
[74] B.G. Orr, D. Kessler, C.W. Synder, L. Sander, "A Model for Strain-Induced Roughening and Coherent Island Growth," Europhys. Lett. 19, 33 (1992).
[75] D. Vanderbilt, L.K. Wickham, "Elastic Energies of Coherent Germanium Islands on Silicon," Mat. Res. Symp. Proc. 202, 555 (1991).
[76] J.W. Matthews, A.E. Blakeslee, "Defects in Epitaxial Multilayers. I. Misfit Dislocations," J. Cryst. Growth 27, 118 (1974).
[77] R. People, J.C. Bean, "Calculations of Critical Layer Thickness Versus Lattice Mismatch for GeSi/Si Strain-Layer Heterostructures," Appl. Phys. Lett. 47, 322 (1985).
[78] I.N. Stranski, L. Krastanow, "Abhandlungen der Mathematisch-Naturwissenschaftlichen Klasse IIb," Akademie der Wissenschaften Wien 146, 797–810 (1938).
[79] D.J. Eaglesham, M. Cerullo, "Dislocation-Free Stranski-Krastanow Growth of Ge on Si(100)," Phys. Rev. Lett. 64, 1943–1946 (1990).

[80] S. Guha, A. Madhukar, K.C. Rajkumar, "Onset of Incoherency and Defect Introduction in the Initial Stages of Molecular Beam Epitaxical Growth of Highly Strained $In_xGa_{1-x}As$ on GaAs(100)," Appl. Phys. Lett. 57, 210 (1990).
[81] G.S. Solomon, C. Santori, M. Pelton, J. Vučković, D.F.E. Waks, Y. Yamamoto, "Efficient, Regulated Single Photons from Quantum Dots in Post Microcavities," in Optics of Quantum Dots And Wires, edited by G. W. Bryant, G. S. Solomon, Artech House, Boston, MA, 483–536 (2005).
[82] P.W. Baumeister, "Optical Absorption of Cuprous Oxide," Phys. Rev. 121, 359–362 (1961).
[83] S. Fafard, Z.R. Wasilewski, C.N. Allen, M.S.D. Picard, J.P. McCaffrey, P.G. Piva, "Manipulating the Energy Levels of Semiconductor Quantum Dots," Phys. Rev. B 59, 15368 (1999).
[84] E. Poem, Y. Kodriano, C. Tradonsky, B.D. Gerardot, P.M. Petroff, D. Gershoni, "Radiative Cascades from Charged Semiconductor Quantum Dots," Phys. Rev. B 81, 085306 (2010).
[85] G. Bester, S. Nair, A. Zunger, "Pseudopotential Calculation of the Excitonic Fine Structure of Million-Atom Self-Assembled $In_{1-x}Ga_xAs$-GaAs Quantum Dots," Phys. Rev. B 67, 161306–161310 (2003).
[86] C.Y. Lu, Y. Zhao, A.N. Vamivakas, C. Matthiesen, S. Fält, A. Badolato, M. Atatüre, "Direct Measurement of Spin Dynamics in InAs/GaAs Quantum Dots Using Time-Resolved Resonance Fluorescence," Phys. Rev. B 81, 035332–035337 (2010).
[87] E.A. Chekhovich, M.M. Glazov, A.B. Krysa, M. Hopkinson, P. Senellart, A. Lemaître, M.S. Skolnick, A.I. Tartakovskii, "Element-Sensitive Measurement of the Holenuclear Spin Interaction in Quantum Dots," Nat. Phys. 9, 74–78 (2013).
[88] S.T. Ylmaz, P. Fallahi, A. Imamoğlu, "Quantum-Dot-Spin Single-Photon Interface," Phys. Rev. Lett. 105, 033601–033605 (2010).
[89] M. Bayer, O. Stern, A. Kuther, A. Forchel, "Spectroscopic Study of Dark Excitons in $In_xGa_{1-x}As$ Self-Assembled Quantum Dots by a Magnetic-Field-Induced Symmetry Breaking," Phys. Rev. B 61, 7293–7276 (2000).
[90] V.D. Kulakovskii, G. Bacher, R. Weigand, T. Kmmell, A. Forchel, E. Borovitskaya, K. Leonardi, D. Hommel, "Fine Structure of Biexciton Emission in Symmetric and Asymmetric CdSe/ZnSe Single Quantum Dots," Phys. Rev. Lett. 82, 1780–1783 (1999).
[91] M. Bayer, G. Ortner, O. Stern, A. Kuther, A.A. Gorbunov, A. Forchel, P. Hawrylak, S. Fafard, K. Hinzer, T.L. Reinecke, S.N. Walck, J.P. Reithmaier, F. Klopf, F. Schäfer, "Fine Structure of Neutral and Charged Excitons in Self-Assembled In(Ga)As/Al(Ga)As Quantum Dots," Phys. Rev. B 65, 195315–195338 (2002).
[92] M. Bayer, O. Stern, P. Hawrylak, S. Fafard, A. Forchel, "Hidden Symmetries in the Energy Levels of Excitonic 'Artificial Atoms'," Nature 405, 923–926 (2000).
[93] X. Xu, Y. Wu, B. Sun, Q. Huang, J. Cheng, D.G. Steel, A.S. Bracker, D. Gammon, C. Emary, L.J. Sham, Fast Spin State Initialization in a Singly Charged InAs-GaAs Quantum Dot by Optical Cooling," Phys. Rev. Lett. 99, 097401–097404 (2007).
[94] J.Y. Marzin, J.M.Gérard, A. Izraël, D. Barrier, G. Bastard, "Photoluminescence of Single InAs Quantum Dots Obtained by Self-Organized Growth on GaAs," Phys. Rev. Lett. 73, 716–719 (1994).
[95] G.S. Solomon, M. Pelton, Y. Yamamoto, "Single-Mode Spontaneous Emission from a Single Quantum Dot in a Three-Dimensional Microcavity," Phys. Rev. Lett. 86, 3903–3906 (2001).
[96] A. Muller, W. Fang, J. Lawall, G.S. Solomon, "Emission Spectrum of a Dressed Exciton-Biexciton Complex in a Semiconductor Quantum Dot," Phys. Rev. Lett. 101, 027401–027404 (2008).
[97] Z. Liu, B.B. Goldberg, S.B. Ippolito, A.N. Vamivakas, M.S. Ünlü, R. Mirin, "Ehigh Resolution, High Collection Efficiency in Numerical Aperture Increasing Lens Microscopy of Individual Quantum Dots," Appl. Phys. Lett. 87, 071905–071907 (2005).
[98] M. Atatüre, J. Dreiser, A. Badolato, A. Imamoglü, "Observation of Faraday Rotation from a Single Confined Spin," Nat. Phys. 3, 101–106 (2007).
[99] A. Dousse, L. Lanco, J. Suffczyński, E. Semenova, A. Miard, A. Lemaître, I. Sagnes, C. Roblin, J. Bloch, P. Senellart, "Controlled Light-Matter Coupling for a Single Quantum Dot Embedded in a Pillar Microcavity Using Far-Field Optical Lithography," Phys. Rev. Lett. 101, 267404–267407 (2008).
[100] E.B. Flagg, A. Muller, S.V. Polyakov, A.M. A. Ling, G.S. Solomon, Interference of Two Photons from Separate Quantum Dots," Phys. Rev. Lett. 104, 137401–137405 (2010).

[101] P. Michler, A. Kiraz, C. Becher, W.V. Schoenfeld, P.M. Petroff, L. Zhang, E. Hu, A. Imamoğlu, "A Quantum Dot Single-Photon Turnstile Device," Science 290, 2282–2285 (2000).
[102] O. Gazzano, S.M. de Vasconcellos, C. Arnold, A. Nowak, E. Galopin, I. Sagnes, L. Lanco, A. Lemaître, P. Senellart, "Bright Solid-State Sources of Indistinguishable Single Photons," Nat. Commun. 4, 1425 (2013).
[103] A. Ulhaq, S. Weiler, S.M. Ulrich, R. Roßbach, M. Jetter, P. Michler, "Cascaded Single-Photon Emission from the Mollow Triplet Sidebands of a Quantum Dot," Nature Photonics 6, 238–242 (2012).
[104] Y.-M. He, Y. He, Y.-J. Wei, D. Wu, M. Atatüre, C. Schneider, S. Höfling, M. Kamp, C.-Y. Lu, J.-W. Pan, "On-demand Semiconductor Single-Photon Source with near-Unity Indistinguishability," Nat. Nanotech. 8, 213–217 (2013).
[105] S.V. Polyakov, A. Muller, E.B. Flagg, A. Ling, N. Borjemscaia, E.V. Keuren, A. Migdall, G.S. Solomon, "Coalescence of Single Photons Emitted by Disparate Single-Photon Sources: The Example of InAs Quantum Dots and Parametric Down-Conversion Sources," Phys. Rev. Lett. 107, 157402–157406 (2011).
[106] E.B. Flagg, S.V. Polyakov, T. Thomay, G.S. Solomon, "Dynamics of Nonclassical Light from a Single Solid-State Quantum Emitter," Phys. Rev. Lett. 109, 163601–163605 (2012).
[107] M. Pelton, C. Santori, J. Vučković, B. Zhang, G.S. Solomon, J. Plant, Y. Yamamoto, "Efficient Source of Single Photons: A Single Quantum Dot in a Micropost Microcavity," Phys. Rev. Lett. 89, 233602–233605 (2002).
[108] M. Pelton, J. Vučković, G.S. Solomon, A. Scherer, Y. Yamamoto, "Three-Dimensionally Confined Modes in Micropost Microcavities: Quality Factors and Purcell Factors," IEEE Q. Electron. (2001).
[109] H. Kim, D. Sridharan, T.C. Shen, G. Solomon, E. Waks, "Magnetic Field Tuning of Two Quantum Dot Spin States to a Photonic Crystal Cavity in the Strong Coupling Regime," Opt. Express 19, 2589–2598 (2011).
[110] J.P. Reithmaier, G. Sęk, A. Löffler, C. Hofmann, S. Kuhn, S. Reitzenstein, L.V. Keldysh, V.D. Kulakovskii, T.L. Reinecke, A. Forchel, "Strong Coupling in a Single Quantum Dot Semiconductor Microcavity System," Nature 432, 197–200 (2004).
[111] K. Srinivasan, O. Painter, "Linear and Nonlinear Optical Spectroscopy of a Strongly Coupled Microdisk Quantum Dot System," Nature 450, 862–866 (2007).
[112] E. Peter, P. Senellart, D. Martrou, A. Lemaître, J. Hours, J.M. Gérard, J. Bloch, "Exciton-Photon Strong-Coupling Regime for a Single Quantum Dot Embedded in a Microcavity," Phys. Rev. Lett. 95, 067401–067404 (2005).
[113] Z.G. Xie, S.G. tzinger, W. Fang, H. Cao, G.S. Solomon, "Influence of a Single Quantum Dot State on the Characteristics of a Microdisk Laser," Phys. Rev. Lett. 98, 117401–117404 (2007).
[114] V. Loo, L. Lanco, A. Lemaître, I. Sagnes, O. Krebs, P. Voisin, P. Senellart, "Quantum Dot-Cavity Strong-Coupling Regime Measured Through Coherent Reflection Spectroscopy in a Very High-Q micropillar," Appl. Phys. Lett. 97, 241110–241112 (2010).
[115] D. Englund, D. Fattal, E. Waks, G. Solomon, B. Zhang, T. Nakaoka, Y. Arakawa, Y. Yamamoto, J.J. Vučković, "Controlling the Spontaneous Emission Rate of Single Quantum Dots in a Two-Dimensional Photonic Crystal," Phys. Rev. Lett. 95, 013904–013907 (2005).
[116] K. Hennessy, A. Badolato, M. Winger, D. Gerace, M. Atatüre, S. Gulde, S. Fält, E.L. Hu, A. Imamoğlu, "Quantum Nature of a Strongly Coupled Single Quantum Dot Cavity System," Nature 445, 896–899 (2007).
[117] S. Kohmoto, H. Nakamura, T. Ishikawa, K. Asakawa, "Site-Controlled Self-Organization of Individual InAs Quantum Dots by Scanning Tunneling Probe-Assisted Nanolithography," Appl. Phys. Lett. 75, 3488–3900 (1999).
[118] D. Chithrani, R.L. Williams, J. Lefebvre, P.J. Poole, G.C. Aers, "Optical Spectroscopy of Single, Site-Selected, InAs-InP Self-Assembled Quantum Dots," Appl. Phys. Lett. 84, 978–980 (2004).
[119] M.H. Baier, S. Watanabe, E. Pelucchi, E. Kapon, "Site-Controlled Self-Organization of Individual InAs Quantum Dots by Scanning Tunneling Probe-Assisted Nanolithography," Appl. Phys. Lett. 84, 1943–1945 (2004).

[120] P. Atkinson, S. Kiravittaya, M. Benyoucef, A. Rastelli, O.G. Schmidt, "Site-Controlled Growth and Luminescence of InAs Quantum Dots Using In Situ Ga-Assisted Deoxidation of Patterned Substrates," Appl. Phys. Lett. 93, 101908–101910 (2008).
[121] Z. Xie, G.S. Solomon, "Spatial Ordering of Quantum Dots in Microdisks," Appl. Phys. Lett. 87, 093106–093108 (2005).
[122] S. Haroche, J.-M. Raimond, "Exploring the Quantum: Atoms, Cavities and Photons," 1st edn., Oxford University Press, New York, NY (2006).
[123] C.H. Bennett, G. Brassard, "Quantum Cryptography: Public Key Distribution and Coin Tossing," Proceedings of the IEEE International Conference on Computers, Systems, and Signal Processing, Bangalore, p. 175 (1984).
[124] R. Loudon, "The Quantum Theory of Light," 3rd edn., Oxford University Press (2000).
[125] C.K. Hong, Z.Y. Ou, L. Mandel, "Measurement of Subpicosecond Time Intervals Between Two Photons by Interference," Phys. Rev. Lett. 59, 2044–2046 (1987).
[126] P. Grangier, "Single Photons Stick Together," Nature 419, 577 (2002).
[127] C. Santori, D. Fattal, J. Vuckovic, G.S. Solomon, Y. Yamamoto, Indistinguishable Photons from a Single-Photon Device," Nature 419, 594–597 (2002).
[128] A. Muller, E.B. Flagg, M. Metcalfe, J. Lawall, G.S. Solomon, Coupling an Epitaxial Quantum Dot to a Fiber-Based External-Mirror Microcavity," Appl. Phys. Lett. 95, 173101 (2009).
[129] S. Seidl, M. Kroner, A. Hogele, K. Karrai, "Effect of Uniaxial Stress on Excitons in a Self-Assembled Quantum Dot," Appl. Phys. Lett. 88, 203113 (2006).
[130] A. Kiraz, M. Atature, A. Imamoglu, "Quantum-Dot Single-Photon Sources: Prospects for Applications in Linear Optics Quantum-Information Processing," Phys. Rev. A 69, 032305 (2004).
[131] J. Bylander, I. Robert-Philip, I. Abram, "Interference and Correlation of Two Independent Photons," Euro. Phys. J. D 22, 295–301 (2003).
[132] A. Zaitsev, "Optical Properties of Diamond: a Data Handbook," Springer (2001).
[133] A. Beveratos, S. Kuhn, R. Brouri, T. Gacoin, J.-P. Poizat, P. Grangier, "Room Temperature Stable Single-Photon Source," Euro. Phys. J. D 18, 191–196 (2002).
[134] A. Gruber, A. Dräbenstedt, C. Tietz, L. Fleury, J. Wratchtrup, C.V. Borczyskowski, "Scanning Confocal Optical Microscopy and Magnetic Resonance on Single Defect Centers," Science 276, 2012–2014 (1997).
[135] F. Jelezko, T. Gaebel, I. Popa, M. Domhan, A. Gruber, J. Wrachtrup, "Observation of Coherent Oscillation of a Single Nuclear Spin and Realization of a Two-Qubit Conditional Quantum Gate," Phys. Rev. Lett. 93, 130501 (2004).
[136] L. Childress, M.V. Gurudev Dutt, J.M. Taylor, A.S. Zibrov, F. Jelezko, J. Wrachtrup, P.R. Hemmer, M.D. Lukin, "Coherent Dynamics of Coupled Electron and Nuclear Spin Qubits in Diamond," Science 314, 281–285 (2006).
[137] M.V. Gurudev Dutt, L. Childress, L. Jiang, E. Togan, J. Maze, F. Jelezko, A.S. Zibrov, P.R. Hemmer, M.D. Lukin, "Quantum Register Based on Individual Electronic and Nuclear Spin Qubits in Diamond," Science 316, 1312–1316 (2007).
[138] R. Hanson, F. Mendoza, R. Epstein, D. Awschalom, "Polarization and Readout of Coupled Single Spins in Diamond," Phys. Rev. Lett. 97, 87601 (2006).
[139] T. Gaebel, M. Domhan, I. Popa, C. Wittmann, P. Neumann, F. Jelezko, J.R. Rabeau, N. Stravrias, A.D. Greentree, S. Prawer, J. Meijer, J. Twamley, P.R. Hemmer, J. Wrachtrup, "Room-Temperature Coherent Coupling of Single Spins in Diamond," Nat. Phys. 2, 408. (2006)
[140] G.D. Fuchs, G. Burkard, P.V. Klimov, D.D. Awschalom, "A Quantum Memory Intrinsic to Single Nitrogen-Vacancy Centres in Diamond," Nat. Phys. 7, 789–793 (2011).
[141] G. Balasubramanian, I.Y. Chan, R. Kolesov, M. Al-Hmoud, J. Tisler, C. Shin, C. Kim, A. Wojcik, P.R. Hemmer, A. Krueger, T. Hanke, A. Leitenstorfer, R. Bratschitsch, F. Jelezko, J. Wrachtrup, "Nanoscale Imaging Magnetometry with Diamond Spins Under Ambient Conditions," Nature (London) 455, 648–651 (2008).
[142] J. R. Maze, P.L. Stanwix, J.S. Hodges, S. Hong, J.M. Taylor, P. Cappellaro, L. Jiang, M.V.G. Dutt, E. Togan, A.S. Zibrov, A. Yacoby, R.L. Walsworth, M.D. Lukin, "Nanoscale Magnetic Sensing with an Individual Electronic Spin in Diamond," Nature (London) 455, 644–647 (2008).

[143] H. Bernien, B. Hensen, W. Pfaff, G. Koolstra, M.S. Blok, L. Robledo, T.H. Taminiau, M. Markham, D.J. Twitchen, L. Childress, R. Hanson, "Heralded Entanglement Between Solid-State Qubits Separated by Three Metres, Nature (London) 497, 86–90 (2013).
[144] G. Davies, M.F. Hamer, "Optical Studies of the 1.945 eV Vibronic Band in Diamond," Proc. R. Soc. London Ser. A 348, 285–298 (1976).
[145] T.P.M. Alegre, C. Santori, G. Medeiros-Ribeiro, R.G. Beausoleil, "Polarization-Selective Excitation of Nitrogen Vacancy Centers in Diamond," Phys. Rev. B 76, 165205 (2007).
[146] A.M. Edmonds, U.F.S. D'Haenens-Johansson, R.J. Cruddace, M.E. Newton, K.-M.C. Fu, C. Santori, R.G. Beausoleil, D.J. Twitchen, M.L. Markham, "Production of Oriented Nitrogen-Vacancy Color Centers in Synthetic Diamond," Phys. Rev. B 86, 035201 (2012).
[147] T. Ishikawa, K.-M.C. Fu, C. Santori, V.M. Acosta, R.G. Beausoleil, H. Watanabe, S. Shikata, K.M. Itoh, "Optical and Spin Coherence Properties of Nitrogen-Vacancy Centers Placed in a 100 nm Thick Isotopically Purified Diamond Layer, Nano Lett. 12, 2083–2087 (2012).
[148] A. Stacey, D.A. Simpson, T.J. Karle, B.C. Gibson, V.M. Acosta, Z. Huang, K.M.C. Fu, C. Santori, R.G. Beausoleil, L.P. McGuinness, *et al.*, "Near-Surface Spectrally Stable Nitrogen Vacancy Centres Engineered in Single Crystal Diamond," Adv. Mater. 24, 3333–3338 (2012).
[149] K. Ohno, F. Joseph Heremans, L.C. Bassett, B.A. Myers, D.M. Toyli, A.C. Bleszynski Jayich, C.J. Palmstrøm, D.D. Awschalom, "Engineering Shallow Spins in Diamond with Nitrogen Delta-Doping," Appl. Phys. Lett. 101, 082413–082413 (2012).
[150] B. Burchard, J. Meijer, I. Popa, T. Gaebel, M. Domhan, C. Wittmann, F. Jelezko, J. Wrachtrup, "Generation of Single Color Centers by Focused Nitrogen Implantation," Appl. Phys. Lett. 87, 261909 (2005).
[151] A. Greentree, P. Olivero, M. Draganski, E. Trajkov, J. Rabeau, P. Reichart, B. Gibson, S. Rubanov, S. Huntington, D. Jamieson, *et al.*, "Critical Components for Diamond-Based Quantum Coherent Devices," J. Phys. Cond. Mat. 18, 825 (2006).
[152] J. Rabeau, P. Reichart, G. Tamanyan, D. Jamieson, S. Prawer, F. Jelezko, T. Gaebel, I. Popa, M. Domhan, J. Wrachtrup, "Implantation of Labelled Single Nitrogen Vacancy Centers in Diamond Using N," Appl. Phys. Lett. 88, 023113 (2006).
[153] B. Naydenov, V. Richter, J. Beck, M. Steiner, P. Neumann, G. Balasubramanian, J. Achard, F. Jelezko, J. Wrachtrup, R. Kalish, "Enhanced Generation of Single Optically Active Spins in Diamond by Ion Implantation," Appl. Phys. Lett. 96, 163108 (2010).
[154] D.M. Toyli, C.D. Weis, G.D. Fuchs, T. Schenkel, D.D. Awschalom, "Chip-Scale Nanofabrication of Single Spins and Spin Arrays in Diamond," Nano Lett. 10, 3168–3172 (2010).
[155] C. Weis, A. Schuh, A. Batra, A. Persaud, I. Rangelow, J. Bokor, C. Lo, S. Cabrini, E. Sideras-Haddad, G. Fuchs, *et al.*, "Single Atom Doping for Quantum Device Development in Diamond and Silicon," J. Vac. Sci. Technol. B: Microelectron. Nanometer Struct. 26, 2596–2600 (2008).
[156] J. Meijer, S. Pezzagna, T. Vogel, B. Burchard, H. Bukow, I. Rangelow, Y. Sarov, H. Wiggers, I. Plümel, F. Jelezko, *et al.*, "Towards the Implanting of Ions and Positioning of Nanoparticles with nm Spatial Resolution," Appl. Phys. A 91, 567–571 (2008).
[157] B. Naydenov, F. Reinhard, A. Lammle, V. Richter, R. Kalish, F. D'Haenens-Johansson, M. Newton, F. Jelezko, J. Wrachtrup, "Increasing the Coherence Time of Single Electron Spins in Diamond by High Temperature Annealing," Appl. Phys. Lett. 97, 242511–242511 (2010).
[158] G. Davies, S.C. Lawson, A.T. Collins, A. Mainwood, S.J. Sharp, "Vacancy-Related Centers in Diamond," Phys. Rev. B 46, 13157–13170 (1992).
[159] V.M. Acosta, E. Bauch, M.P. Ledbetter, C. Santori, K.-M.C. Fu, P.E. Barclay, R.G. Beausoleil, H. Linget, J.F. Roch, F. Treussart, S. Chemerisov, W. Gawlik, D. Budker, "Diamonds with a High Density of Nitrogen-Vacancy Centers for Magnetometry Applications," Phys. Rev. B 80, 115202 (2009).
[160] L. Bassett, F. Heremans, C. Yale, B. Buckley, D. Awschalom, "Electrical Tuning of Single Nitrogen-Vacancy Center Optical Transitions Enhanced by Photoinduced Fields," Phys. Rev. Lett. 107, 266403 (2011).
[161] Y. Mita, Change of Absorption Spectra in Type-Ib Diamond with Heavy Neutron Irradiation," Phys. Rev. B 53, 11360–11364 (1996).
[162] J. Martin, R. Wannemacher, J. Teichert, L. Bischoff, B. Köhler, "Generation and Detection of Fluorescent Color Centers in Diamond with Submicron Resolution," Appl. Phys. Lett. 75, 3096 (1999).

[163] F. Waldermann, P. Olivero, J. Nunn, K. Surmacz, Z. Wang, D. Jaksch, R. Taylor, I. Walmsley, M. Draganski, P. Reichart, A. Greentree, D. Jamieson, S. Prawer, "Creating Diamond Color Centers for Quantum Optical Applications," Diamond Related Mater 16, 1887–1895 (2007).
[164] T. Wee, Y. Tzeng, C. Han, H. Chang, W. Fann, J. Hsu, K. Chen, Y. Yu, "Two-Photon Excited Fluorescence of Nitrogen-Vacancy Centers in Proton-Irradiated Type Ib Diamond," J. Phys. Chem. A 111, 9379–9386 (2007).
[165] T. Schenkel, A. Persaud, S. Park, J. Nilsson, J. Bokor, J. Liddle, R. Keller, D. Schneider, D. Cheng, D. Humphries, "Solid State Quantum Computer Development in Silicon with Single Ion Implantation," J. Appl. Phys. 94, 7017–7024 (2003).
[166] D.N. Jamieson, C. Yang, T. Hopf, S. Hearne, C. Pakes, S. Prawer, M. Mitic, E. Gauja, S. Andresen, F. Hudson, *et al.*, "Controlled Shallow Single-Ion Implantation in Silicon Using an Active Substrate for sub-20-keV ions," Appl. Phys. Lett. 86, 202101–202101 (2005).
[167] J. Loubser, J. Van Wyk, "Electron Spin Resonance in the Study of Diamond," Rep. Prog. Phys. 41, 1201 (1978).
[168] E. Van Oort, N. Manson, M. Glasbeek, "Optically Detected Spin Coherence of the Diamond NV Centre in Its Triplet Ground State," J. Phys. C 21, 4385 (1988).
[169] N.R.S. Reddy, N.B. Manson, E.R. Krausz, "Two-Laser Spectral Hole Burning in a Colour Centre in Diamond," J. Lumin. 38, 46 (1987).
[170] K.-M.C. Fu, C. Santori, P.E. Barclay, L.J. Rogers, N.B. Manson, R.G. Beausoleil, "Observation of the Dynamic Jahn-Teller Effect in the Excited States of Nitrogen-Vacancy Centers in Diamond, Phys. Rev. Lett. 103, 256404 (2009).
[171] A. Batalov, C. Zierl, T. Gaebel, P. Neumann, I. Chan, G. Balasubramanian, P. Hemmer, F. Jelezko, J. Wrachtrup, "Temporal Coherence of Photons Emitted by Single Nitrogen-Vacancy Defect Centers in Diamond Using Optical Rabi-Oscillations," Phys. Rev. Lett. 100, 77401 (2008).
[172] L. Rogers, S. Armstrong, M. Sellars, N. Manson, "Infrared Emission of the NV Centre in Diamond: Zeeman and Uniaxial Stress Studies, New J. Phys. 10, 103024 (2008).
[173] V. Acosta, A. Jarmola, E. Bauch, D. Budker, "Optical Properties of the Nitrogen-Vacancy Singlet Levels in Diamond," Phys. Rev. B 82, 201202 (2010).
[174] L. Robledo, H. Bernien, T. van der Sar, R. Hanson, "Spin Dynamics in the Optical Cycle of Single Nitrogen-Vacancy Centres in Diamond, New J. Phys. 13, 025013 (2011).
[175] F.A. Inam, M.D. Grogan, M. Rollings, T. Gaebel, J.M. Say, C. Bradac, T.A. Birks, W.J. Wadsworth, S. Catelletto, J.R. Rabeau, *et al.*, Emission and Non-radiative Decay of Nanodiamond NV Centers in a Low-Refractive Index Environment, ACS Nano (2013).
[176] K. Beha, A. Batalov, N.B. Manson, R. Bratschitsch, A. Leitenstorfer, "Optimum Photoluminescence Excitation and Recharging Cycle of Single Nitrogen-Vacancy Centers in Ultrapure Diamond," Phys. Rev. Lett. 109, 097404 (2012).
[177] P. Siyushev, H. Pinto, M. Vörös, A. Gali, F. Jelezko, J. Wrachtrup, "Optically Controlled Switching of the Charge State of a Single Nitrogen-Vacancy Center in Diamond at Cryogenic Temperatures," Phys. Rev. Lett. 110, 167402 (2013).
[178] P. Tamarat, T. Gaebel, J. Rabeau, M. Khan, A. Greentree, H. Wilson, L. Hollenberg, S. Prawer, P. Hemmer, F. Jelezko, *et al.*, "Stark Shift Control of Single Optical Centers in Diamond," Phys. Rev. Lett. 97, 83002 (2006).
[179] C. Santori, P. Tamarat, P. Neumann, J. Wrachtrup, D. Fattal, R. Beausoleil, J. Rabeau, P. Olivero, A. Greentree, S. Prawer, *et al.*, "Coherent Population Trapping of Single Spins in Diamond under Optical Excitation," Phys. Rev. Lett. 97, 247401 (2006).
[180] P. Tamarat, N. Manson, J. Harrison, R. McMurtrie, A. Nizovtsev, C. Santori, R. Beausoleil, P. Neumann, T. Gaebel, F. Jelezko, *et al.*, Spin-Flip and Spin-Conserving Optical Transitions of the Nitrogen-Vacancy Centre in Diamond," New J. Phys. 10, 045004 (2008).
[181] A. Batalov, V. Jacques, F. Kaiser, P. Siyushev, P. Neumann, L. Rogers, R. McMurtrie, N. Manson, F. Jelezko, J. Wrachtrup, "Low Temperature Studies of the Excited-State Structure of Negatively Charged Nitrogen-Vacancy Color Centers in Diamond," Phys. Rev. Lett. 102, 195506 (2009).
[182] L. Rogers, R. McMurtrie, M. Sellars, N. Manson, "Time-Averaging Within the Excited State of the Nitrogen-Vacancy Centre in Diamond," New J. Phys. 11, 063007 (2009).
[183] G. Fuchs, V. Dobrovitski, R. Hanson, A. Batra, C. Weis, T. Schenkel, D. Awschalom, "Excited-State Spectroscopy Using Single Spin Manipulation in Diamond," Phys. Rev. Lett. 101, 117601 (2008).

[184] P. Neumann, R. Kolesov, V. Jacques, J. Beck, J. Tisler, A. Batalov, L. Rogers, N. Manson, G. Balasubramanian, F. Jelezko, *et al.*, "Excited-State Spectroscopy of Single NV Defects in Diamond Using Optically Detected Magnetic Resonance, New J. Phys. 11, 013017 (2009).
[185] V.M. Acosta, C. Santori, A. Faraon, Z. Huang, K.-M.C. Fu, A. Stacey, D.A. Simpson, K. Ganesan, S. Tomljenovic-Hanic, A.D. Greentree, S. Prawer, R.G. Beausoleil, "Dynamic Stabilization of the Optical Resonances of Single Nitrogen-Vacancy Centers in Diamond," Phys. Rev. Lett. 108, 206401 (2012).
[186] N. Manson, C. Wei, "Transient Hole Burning in N-V Centre in Diamond," J. Luminescence 58, 158–160 (1994).
[187] C. Santori, D. Fattal, S. Spillane, M. Fiorentino, R. Beausoleil, A. Greentree, P. Olivero, M. Draganski, J. Rabeau, P. Reichart, B. Gibson, S. Rubanov, D. Jamieson, S. Prawer, "Coherent Population Trapping in Diamond NV Centers at Zero Magnetic Field," Optics Express 14, 7986–7993 (2006).
[188] E. Togan, Y. Chu, A.S. Trifonov, L. Jiang, J. Maze, L. Childress, M.V.G. Dutt, A.S. Sorensen, P.R. Hemmer, A.S. Zibrov, M.D. Lukin, "Quantum Entanglement Between an Optical Photon and a Solid-State Spin Qubit," Nature (London) 466, 730–734 (2010).
[189] L. Robledo, L. Childress, H. Bernien, B. Hensen, P.F.A. Alkemade, R. Hanson, "High-Fidelity Projective Read-Out of a Solid-State Spin Quantum Register," Nature (London) 477, 574–578 (2011).
[190] A. Lenef, S. Rand, "Electronic Structure of the NV Center in Diamond: Theory," Phys. Rev. B 53, 13441 (1996).
[191] J. Martin, "Fine Structure of Excited 3E State in Nitrogen-Vacancy Centre of Diamond," J. Luminescence 81, 237–247 (1999).
[192] N. Manson, R. McMurtrie, "Issues Concerning the Nitrogen-Vacancy Center in Diamond," J. Luminescence 127, 98–103 (2007).
[193] J. Maze, A. Gali, E. Togan, Y. Chu, A. Trifonov, E. Kaxiras, M. Lukin, "Properties of Nitrogen-Vacancy Centers in Diamond: The Group Theoretic Approach," New J. Phys. 13, 025025 (2011).
[194] M.W. Doherty, N.B. Manson, P. Delaney, L.C. Hollenberg, "The Negatively Charged Nitrogen-Vacancy Centre in Diamond: The Electronic Solution," New J. Phys. 13, 025019 (2011).
[195] A. Gali, M. Fyta, E. Kaxiras, "Ab Initio Supercell Calculations on Nitrogen-Vacancy Center in Diamond: Electronic structure and hyperfine tensors," Phys. Rev. B 77, 155206 (2008).
[196] F.M. Hossain, M.W. Doherty, H.F. Wilson, L.C. Hollenberg, "Ab Initio Electronic and Optical Properties of the NVˆ{-} Center in Diamond," Phys. Rev. Lett. 101, 226403 (2008).
[297] C.G. Yale, B.B. Buckley, D.J. Christle, G. Burkard, F.J. Heremans, L.C. Bassett, D.D. Awschalom, "All-Optical Control of a Solid-State Spin Using Coherent Dark States" (2013), preprint arXiv:1302.6638.
[298] P.R. Hemmer, A.V. Turukhin, S.M. Shahriar, J.A. Musser, "Raman-Excited Spin Coherences in Nitrogen-Vacancy Color Centers in Diamond," Opt. Lett. 26, 361–363 (2001).
[299] V.M. Acosta, K. Jensen, C. Santori, D. Budker, R.G. Beausoleil, "Electromagnetically-Induced Transparency in a Diamond Spin Ensemble Enables All-Optical Electromagnetic Field Sensing" (2013), preprint arXiv:1303.6996.
[200] K. Hammerer, A.S. Sørensen, E.S. Polzik, "Quantum Interface Between Light and Atomic Ensembles," Rev. Mod. Phys. 82, 1041 (2010).
[201] A. Beveratos, R. Brouri, T. Gacoin, A. Villing, J.-P. Poizat, P. Grangier, "Single Photon Quantum Cryptography," Phys. Rev. Lett. 89, 187901 (2002).
[202] T. Schröder, F. Gädeke, M.J. Banholzer, O. Benson, "Ultrabright and Efficient Single-Photon Generation Based on Nitrogen-Vacancy Centres in Nanodiamonds on a Solid Immersion Lens," New J. Phys. 13, 055017 (2011).
[203] A. Faraon, C. Santori, Z. Huang, V.M. Acosta, R.G. Beausoleil, "Coupling of Nitrogen-Vacancy Centers to Photonic Crystal Cavities in Monocrystalline Diamond," Phys. Rev. Lett. 109, 033604 (2012).
[204] G. Balasubramanian, P. Neumann, D. Twitchen, M. Markham, R. Kolesov, N. Mizuochi, J. Isoya, J. Achard, J. Beck, J. Tissler, V. Jacques, P.R. Hemmer, F. Jelezko, J. Wrachtrup, "Ultralong Spin Coherence Time in Isotopically Engineered Diamond, Nature Mater. 8, 383–387 (2009).

[205] I. Popa, T. Gaebel, M. Domhan, C. Wittmann, F. Jelezko, J. Wrachtrup, "Energy Levels and Decoherence Properties of Single Electron and Nuclear Spins in a Defect Center in Diamond," Phys. Rev. B 70, 201203 (2004).
[206] N. Bar-Gill, L.M. Pham, A. Jarmola, D. Budker, R.L. Walsworth, "Solid-State Electronic Spin Coherence Time Approaching One Second" (2012), preprint arXiv:1211.7094.
[207] P. Neumann, J. Beck, M. Steiner, F. Rempp, H. Fedder, P. R. Hemmer, J. Wrachtrup, F. Jelezko, "Single-Shot Readout of a Single Nuclear Spin," Science 329, 542–544 (2010).
[208] L. Childress, J. Taylor, A. Sørensen, M. Lukin, "Fault-Tolerant Quantum Repeaters with Minimal Physical Resources and Implementations Based on Single-Photon Emitters," Phys. Rev. A 72, 52330 (2005).
[209] S. Benjamin, D. Browne, J. Fitzsimons, J. Morton, "Brokered Graph-State Quantum Computation," New J. Phys 8, 141 (2006).
[210] I. Aharonovich, S. Castelletto, D. Simpson, C. Su, A. Greentree, S. Prawer, "Diamond-Based Single-Photon Emitters," Report Progress Phys. 74, 076501 (2011).
[211] S. Pezzagna, D. Rogalla, D. Wildanger, J. Meijer, A. Zaitsev, "Creation and Nature of Optical Centres in Diamond for Single-Photon Emission Overview and Critical Remarks," New J. Phys. 13, 035024 (2011).
[212] C. Wang, C. Kurtsiefer, H. Weinfurter, B. Burchard, "Single Photon Emission from SiV Centres in Diamond Produced by Ion Implantation," J. Phys. B: At. Mol. Opt. Phys. 39, 37 (2006).
[213] E. Neu, D. Steinmetz, J. Riedrich-Möller, S. Gsell, M. Fischer, M. Schreck, C. Becher, "Single Photon Emission from Silicon-Vacancy Colour Centres in Chemical Vapour Deposition Nano-Diamonds on Iridium," New J. Phys. 13, 025012 (2011).
[214] I. Aharonovich, S. Castelletto, D.A. Simpson, A. Stacey, J. McCallum, A.D. Greentree, S. Prawer, "Two-Level Ultrabright Single Photon Emission from Diamond Nanocrystals," Nano Lett. 9, 3191–3195 (2009).
[215] I. Aharonovich, S. Castelletto, B.C. Johnson, J.C. McCallum, D.A. Simpson, A.D. Greentree, S. Prawer, "Chromium Single-Photon Emitters in Diamond Fabricated by Ion Implantation," Phys. Rev. B 81, 121201 (2010).
[216] T. Gaebel, I. Popa, A. Gruber, M. Domhan, F. Jelezko, J. Wrachtrup, "Stable Single-Photon Source in the Near Infrared," New J. Phys. 6, 98 (2004).
[217] E. Wu, J. Rabeau, G. Roger, F. Treussart, H. Zeng, P. Grangier, S. Prawer, J.-F. Roch, "Room Temperature Triggered Single-Photon Source in the Near Infrared," New J. Phys. 9, 434 (2007).
[218] D. Simpson, E. Ampem-Lassen, B. Gibson, S. Trpkovski, F. Hossain, S. Huntington, A. Greentree, L. Hollenberg, S. Prawer, "A Highly Efficient Two Level Diamond Based Single Photon Source," Appl. Phys. Lett. 94, 203107–203107 (2009).
[219] B. Naydenov, R. Kolesov, A. Batalov, J. Meijer, S. Pezzagna, D. Rogalla, F. Jelezko, J. Wrachtrup, "Engineering Single Photon Emitters by Ion Implantation in Diamond," Appl. Phys. Lett. 95, 181109–181109 (2009).
[220] S. Castelletto, B. Johnson, N. Stavrias, T. Umeda, T. Ohshima, "Efficiently Engineered Room Temperature Single Photons in Silicon Carbide," (2012), preprint arXiv:1210.5047.
[221] A.J. Morfa, B.C. Gibson, M. Karg, T.J. Karle, A.D. Greentree, P. Mulvaney, S. Tomljenovic-Hanic, "Single-Photon Emission and Quantum Characterization of Zinc Oxide Defects," Nano Lett. 12, 949–954 (2012).
[222] R. Kolesov, K. Xia, R. Reuter, R. Stöhr, A. Zappe, J. Meijer, P. Hemmer, J. Wrachtrup, "Optical Detection of a Single Rare-Earth Ion in a Crystal," Nat. Commun. 3, 1029 (2012).
[223] J. Hadden, J. Harrison, A. Stanley-Clarke, L. Marseglia, Y.-L. Ho, B. Patton, J. OBrien, J. Rarity, "Strongly Enhanced Photon Collection from Diamond Defect Centers Under Microfabricated Integrated Solid Immersion Lenses," Appl. Phys. Lett. 97, 241901–241901 (2010).
[224] A. Faraon, C. Santori, Z. Huang, K.-M.C. Fu, V.M. Acosta, D. Fattal, R.G. Beausoleil, "Quantum Photonic Devices in Single-Crystal Diamond," New J. Phys. 15, 025010 (2013).
[225] S. Schietinger, M. Barth, T. Aichele, O. Benson, "Plasmon-Enhanced Single Photon Emission from a Nanoassembled Metal-Diamond Hybrid Structure at Room Temperature," Nano Lett. 9, 1694–1698 (2009).
[226] T.M. Babinec, B.J.M. Hausmann, M. Khan, Y. Zhang, J.R. Maze, P.R. Hemmer, M. Loncar, "A Diamond Nanowire Single-Photon Source, Nat. Nanotech. 5, 195–199 (2010).

[227] L. Marseglia, J. Hadden, A. Stanley-Clarke, J. Harrison, B. Patton, Y.-L. Ho, B. Naydenov, F. Jelezko, J. Meijer, P. Dolan, *et al.*, "Nanofabricated Solid Immersion Lenses Registered to Single Emitters in Diamond," Appl. Phys. Lett. 98, 133107–133107 (2011).
[228] A. Faraon, P.E. Barclay, C. Santori, K.-M.C. Fu, R.G. Beausoleil, "Resonant Enhancement of the Zero-Phonon Emission from a Colour Centre in a Diamond Cavity," Nat. Photon. 5, 301–305 (2011).
[229] B.J. Hausmann, B. Shields, Q. Quan, P. Maletinsky, M. McCutcheon, J.T. Choy, T.M. Babinec, A. Kubanek, A. Yacoby, M.D. Lukin, *et al.*, Integrated Diamond Networks for Quantum Nanophotonics," Nano Lett. 12, 1578–1582 (2012).
[230] M.J. Burek, N.P. de Leon, B.J. Shields, B.J. Hausmann, Y. Chu, Q. Quan, A.S. Zibrov, H. Park, M.D. Lukin, M. Loncar, "Free-Standing Mechanical and Photonic Nanostructures in Single-Crystal Diamond," Nano Lett. 12, 6084–6089 (2012).
[231] J. Riedrich-Möller, L. Kipfstuhl, C. Hepp, E. Neu, C. Pauly, F. Mücklich, A. Baur, M. Wandt, S. Wolff, M. Fischer, *et al.*, "One-and Two-Dimensional Photonic Crystal Microcavities in Single Crystal Diamond," Nat. Nanotechnol. 7, 69–74 (2011).
[232] M. Hiscocks, K. Ganesan, B. Gibson, S. Huntington, F. Ladouceur, S. Prawer, "Diamond Waveguides Fabricated by Reactive Ion Etching," Opt. Express 16, 19512–19519 (2008).
[233] I. Bayn, B. Meyler, A. Lahav, J. Salzman, R. Kalish, B.A. Fairchild, S. Prawer, M. Barth, O. Benson, T. Wolf, P. Siyushev, F. Jelezko, J. Wrachtrup, "Processing of Photonic Crystal Nanocavity for Quantum Information in Diamond," Diamond Related Mater. 20, 937–943 (2011).
[234] S. Castelletto, J. Harrison, L. Marseglia, A. Stanley-Clarke, B. Gibson, B. Fairchild, J. Hadden, Y.D. Ho, M. Hiscocks, K. Ganesan, *et al.*, "Diamond-Based Structures to Collect and Guide Light," New J. Phys. 13, 025020 (2011).
[235] C.F. Wang, Y.-S. Choi, J.C. Lee, E.L. Hu, J. Yang, J.E. Butler, "Observation of Whispering Gallery Modes in Nanocrystalline Diamond Microdisks," Appl. Phys. Lett. 90, 081110 (2007a).
[236] C.F. Wang, R. Hanson, D.D. Awschalom, E.L. Hu, T. Feygelson, J. Yang, J.E. Butler, "Fabrication and Characterization of Two-Dimenstional Photonic Crystal Microcavities in Nanocrystalline Diamond," Appl. Phys. Lett. 91, 201112 (2007b).
[237] K. Fu, C. Santori, P. Barclay, I. Aharonovich, S. Prawer, N. Meyer, A. Holm, R. Beausoleil, "Coupling of Nitrogen-Vacancy Centers in Diamond to a GaP Waveguide," Appl. Phys. Lett. 93, 234107 (2008).
[238] P. Barclay, K. Fu, C. Santori, R. Beausoleil, "Chip-Based Microcavities Coupled to Nitrogen-Vacancy Centers in Single Crystal Diamond," Appl. Phys. Lett. 95, 191115 (2009a).
[239] P.E. Barclay, K.-M. Fu, C. Santori, R.G. Beausoleil, "Hybrid Photonic Crystal Cavity and Waveguide for Coupling to Diamond NV-Centers," Opt. Express 17, 9588–9601 (2009b).
[240] M. Larsson, K.N. Dinyari, H. Wang, "Composite Optical Microcavity of Diamond Nanopillar and Silica Microsphere," Nano Lett. 9, 1447–1450 (2009).
[241] Y.-S. Park, A. Cook, H. Wang, "Cavity QED with Diamond Nanocrystals and Silica Microspheres," Nano Lett. 6, 2075–2079 (2006).
[242] S. Schietinger, T. Schroder, O. Benson, "One-by-One Coupling of Single Defect Centers in Nanodiamonds to High-Q Modes of an Optical Microresonator," Nano Lett. 8, 3911–3915 (2008).
[243] S. Schietinger, O. Benson, "Coupling Single NV-Centres to High-Q Whispering Gallery Modes of a Preselected Frequency-Matched Microresonator," J. Phys. B: At. Mol. Opt. Phys. 42, 114001 (2009).
[244] P. Barclay, C. Santori, K. Fu, R. Beausoleil, O. Painter, "Coherent Interference Effects in a Nano-Assembled Diamond NV Center Cavity-QED System," Opt. Express 17, 8081–8097 (2008).
[245] J. Wolters, A.W. Schell, G. Kewes, N. Nusse, M. Schoengen, H. Doscher, T. Hannappel, B. Lochel, M. Barth, O. Benson, "Enhancement of the Zero Phonon Line Emission from a Single Nitrogen Vacancy Center in a Nanodiamond Via Coupling to a Photonic Crystal Cavity," Appl. Phys. Lett. 97, 141108–141108 (2010).
[246] D. Englund, B. Shields, K. Rivoire, F. Hatami, J. Vuckovic, H. Park, M.D. Lukin, "Deterministic Coupling of a Single Nitrogen Vacancy Center to a Photonic Crystal Cavity," Nano Lett. 10, 3922–3926 (2010).

[247] T. Van der Sar, J. Hagemeier, W. Pfaff, E. Heeres, S. Thon, H. Kim, P. Petroff, T. Oosterkamp, D. Bouwmeester, R. Hanson, "Deterministic Nanoassembly of a Coupled Quantum Emitter–Photonic Crystal Cavity System," Appl. Phys. Lett. 98, 193103 (2011).
[248] H. Bernien, L. Childress, L. Robledo, M. Markham, D. Twitchen, R. Hanson, "Two-Photon Quantum Interference from Separate Nitrogen Vacancy Centers in Diamond," Phys. Rev. Lett. 108, 043604 (2012).
[249] C. Cabrillo, J.I. Cirac, P. García-Fernández, P. Zoller, "Creation of Entangled States of Distant Atoms by Interference," Phys. Rev. A 59, 1025–1033 (1999).
[250] S.D. Barrett, P. Kok, "Efficient High-Fidelity Quantum Computation Using Matter Qubits and Linear Optics," Phys. Rev. A 71, 060310(R) (2005).
[251] H.-J. Briegel, W. Dür, J.I. Cirac, P. Zoller, "Quantum Repeaters: The Role of Imperfect Local Operations in Quantum Communication," Phys. Rev. Lett. 81, 5932–5935 (1998).
[252] B. Sun, M.S. Chapman, L. You, "Atom-Photon Entanglement Generation and Distribution," Phys. Rev. A 69, 042316 (2004).
[253] J. Beugnon, M.P.A. Jones, J. Dingjan, B. Darquié, G. Messin, A. Browaeys, P. Grangier, "Quantum Interference Between Two Single Photons Emitted by Independently Trapped Atoms," Nature 440, 779–782 (2006).
[254] P. Maunz, D.L. Moehring, S. Olmschenk, K.C. Younge, D.N. Matsukevich, C. Monroe, "Quantum Interference of Photon Pairs from Two Remote Trapped Atomic Ions," Nat. Phys. 3, 538–541 (2007).
[255] R. Raussendorf, H.-J. Briegel, "A One-Way Quantum Computer," Phys. Rev. Lett. 86, 5188–5191 (2001).
[256] H.P. Büchler, M. Hermele, S.D. Huber, M.P.A. Fisher, P. Zoller, "Atomic Quantum Simulator for Lattice Gauge Theories and Ring Exchange Models," Phys. Rev. Lett. 95, 040402 (2005).
[257] K.D. Greve, L. Yu, P.L. McMahon, J.S. Pelc, C.M. Natarajan, N.Y. Kim, E. Abe, S. Maier, C. Schneider, M. Kamp, S. Höfling, R.H. Hadfield, A. Forchel, M.M. Fejer, Y. Yamamoto, "Quantum-Dot Spinphoton Entanglement Via Frequency Downconversion to Telecom Wavelength," Nature 491, 421425 (2012).
[258] W.B. Gao, P. Fallahi, E. Togan, J. Miguel-Sanchez, A. Imamoğlu, "Observation of Entanglement Between a Quantum Dot Spin and a Single Photon, Nature 491, 426430 (2012).
[259] J.R. Schaibley, A.P. Burgers, G.A. McCracken, L.-M. Duan, P.R. Berman, D.G. Steel, "Demonstration of Quantum Entanglement Between a Single Electron Spin Confined to an InAs Quantum Dot and a Photon," Phys. Rev. Lett. 110, 167401–167405 (2013).
[260] N. Mizuochi, T. Makino, H. Kato, D. Takeuchi, M. Ogura, H. Okushi, M. Nothaft, P. Neumann, A. Gali, F. Jelezko, J. Wrachtrup, and S. Yamasaki, "Electrically Driven Single-Photon Source at Room Temperature in Diamond," Nat. Photonics 6, 299–303 (2012).